SANDIA REPORT

SAND97-0962 • UC-705
Unlimited Release
Printed April 1997

Structural System Identification: Structural Dynamics Model Validation

RECEIVED
MAY 06 1997
OSTI

J. R. Red-Horse

Prepared by
Sandia National Laboratories
Albuquerque, New Mexico 87185 and Livermore, California 94550

Sandia is a multiprogram laboratory operated by Sandia
Corporation, a Lockheed Martin Company, for the United States
Department of Energy under Contract DE-AC04-94AL85000.

Approved for public release; distribution is unlimited.

Sandia National Laboratories

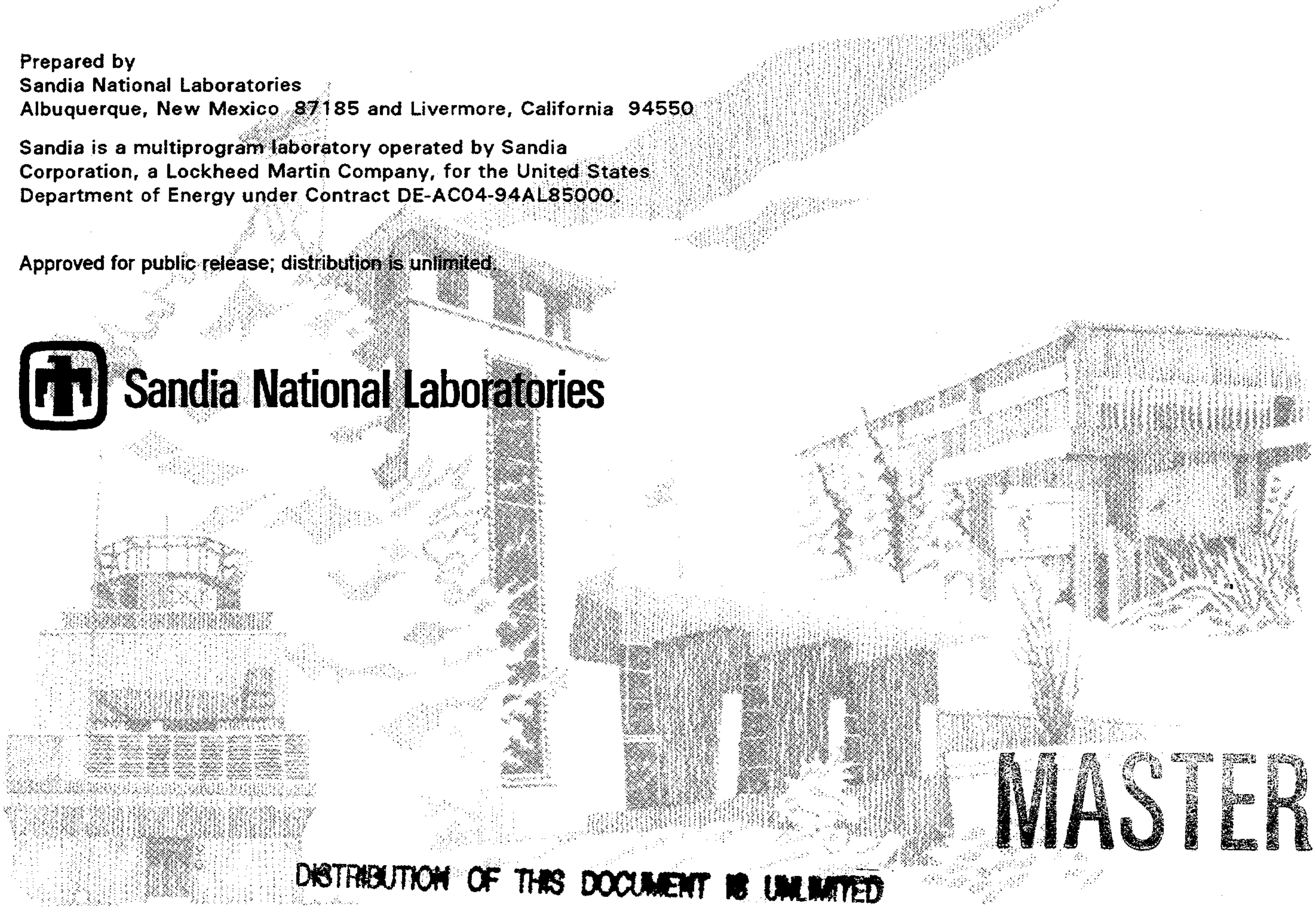

MASTER

DISTRIBUTION OF THIS DOCUMENT IS UNLIMITED

Issued by Sandia National Laboratories, operated for the United States Department of Energy by Sandia Corporation.

NOTICE: This report was prepared as an account of work sponsored by an agency of the United States Government. Neither the United States Government nor any agency thereof, nor any of their employees, nor any of their contractors, subcontractors, or their employees, makes any warranty, express or implied, or assumes any legal liability or responsibility for the accuracy, completeness, or usefulness of any information, apparatus, product, or process disclosed, or represents that its use would not infringe privately owned rights. Reference herein to any specific commercial product, process, or service by trade name, trademark, manufacturer, or otherwise, does not necessarily constitute or imply its endorsement, recommendation, or favoring by the United States Government, any agency thereof, or any of their contractors or subcontractors. The views and opinions expressed herein do not necessarily state or reflect those of the United States Government, any agency thereof, or any of their contractors.

Printed in the United States of America. This report has been reproduced directly from the best available copy.

Available to DOE and DOE contractors from
Office of Scientific and Technical Information
P.O. Box 62
Oak Ridge, TN 37831

Prices available from (615) 576-8401, FTS 626-8401

Available to the public from
National Technical Information Service
U.S. Department of Commerce
5285 Port Royal Rd
Springfield, VA 22161

NTIS price codes
Printed copy: A05
Microfiche copy: A01

DISCLAIMER

This report was prepared as an account of work sponsored by an agency of the United States Government. Neither the United States Government nor any agency thereof, nor any of their employees, make any warranty, express or implied, or assumes any legal liability or responsibility for the accuracy, completeness, or usefulness of any information, apparatus, product, or process disclosed, or represents that its use would not infringe privately owned rights. Reference herein to any specific commercial product, process, or service by trade name, trademark, manufacturer, or otherwise does not necessarily constitute or imply its endorsement, recommendation, or favoring by the United States Government or any agency thereof. The views and opinions of authors expressed herein do not necessarily state or reflect those of the United States Government or any agency thereof.

DISCLAIMER

Portions of this document may be illegible in electronic image products. Images are produced from the best available original document.

SAND97-0962
Unlimited Release
Printed April 1997

Distribution
Category UC-705

Structural System Identification: Structural Dynamics Model Validation

J. R. Red-Horse
Structural Dynamics and Vibration Control Dept.
P.O. Box 5800
Albuquerque, New Mexico 87185-0439

Abstract

Structural system identification is concerned with the development of systematic procedures and tools for developing predictive analytical models based on a physical structure's dynamic response characteristics. It is a multidisciplinary process that involves the ability (1) to define high fidelity physics-based analysis models, (2) to acquire accurate test-derived information for physical specimens using diagnostic experiments, (3) to validate the numerical simulation model by reconciling differences that inevitably exist between the analysis model and the experimental data, and (4) to quantify uncertainties in the final system models and subsequent numerical simulations. The goal of this project was to develop structural system identification techniques and software suitable for both research and production applications in code and model validation.

Contents

1. Introduction

The development of suitable mathematical models for dynamic structural analysis is an integral part of the overall structural design and analysis process. If reliable, predictive models can be developed, they can be used subsequently for a variety of tasks. Examples include the evaluation of competing structural design alternatives, developing structural subcomponent environment specifications and designing control algorithms when elastic structural vibration is an issue. Obviously, the application possibilities are diverse, but the long-term goal of programs such as this is to achieve the ability to perform virtual tests to support weapons qualification in lieu of hardware prototyping.

The ultimate arbiter for establishing how accurately a given model represents a physical structure is the structure itself. However, building and testing hardware specimens for any purpose, including model validation, is a costly and time consuming affair. Thus, a small subset of the possible support and loading configurations of interest are utilized in the validation process. This process, termed structural system identification, is depicted graphically in Figure 1.1. It entails the development of an analytical model of correct model form (i.e., it incorporates the proper physics representing the system) possessing suitable parametric quantities to allow *a posteriori* model adjustment; an appropriately designed diagnostic experiment tasked with extracting necessary physical phenomena for use as validation criteria; and, a reconciliation process in which analysis predictions and experimental data obtained in controlled laboratory tests are compared and any differences are resolved.

The subject effort in structural system identification was concerned with the development of systematic procedures and tools for reconciling and understanding these differences. Further, motivated by the imprecise nature of measuring physical system response, the multidisciplinary system identification approach attempted to investigate and quantify uncertainty in test data and to use these measurement uncertainties in assessing the confidence in the physical parameters in the final, reconciled analysis models.

In the remainder of this document a discussion of these closely related, though technically diverse, tasks is presented. Overviews of each are provided in Chapters 2–4. More in-depth details are presented in the text of published articles contained in Appendix A. Appropriate reference citations can be found in this documentation as well.

This Sandia research effort received significant interest and inquires for technical support and collaboration from government agencies, such as NASA and DoD agencies, as well as from several commercial agencies in the automotive, aerospace and offshore oil production industries.

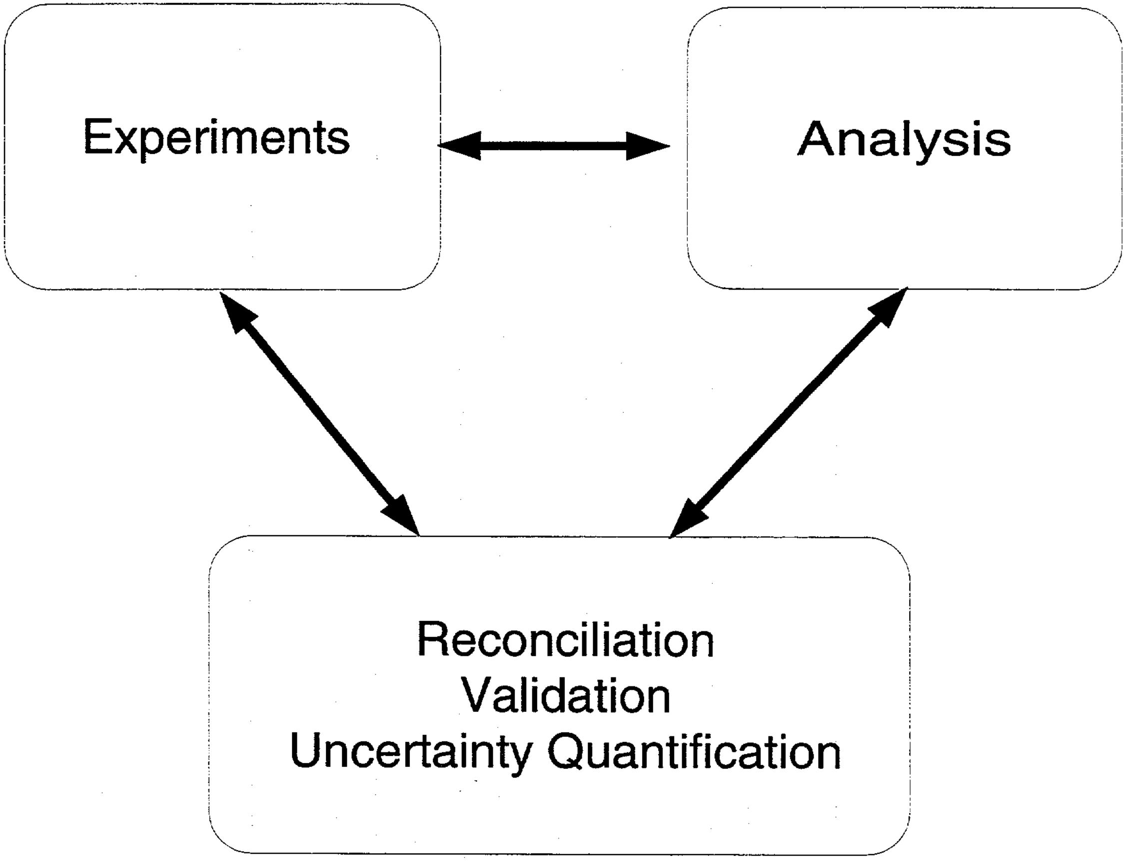

Figure 1.1. Outline of System Identification Process

2. Diverse Technical Breadth

The structural system identification process is broad in scope: analysis models must be developed, experimental data must be gathered and reduced, and differences between the two must reconciled. In this chapter, a brief discussion of each of these is presented.

2.1 Experimental

The task of obtaining high quality experimental data and reducing this data appropriately requires great care. For structural dynamics model development, these steps often result in experimentally derived modal models. A number of issues are relevant:

- It is nontrivial to ensure that the structure, in its test configuration, is the same structure that is being modeled. For example, it is physically impossible to test a structure under idealized free-free boundary conditions. Steps must be taken to mitigate the effects of these BC uncertainties along with any other deviations from the ideal.
- Typically, measurement degrees of freedom (DOF) in a test setup are far fewer in number than are present in a finite element analysis model. Excitation and measurement locations must be selected so that information about the modal model is maximized. At the core of this is the ability to excite and to measure all of the modal frequencies and mode shapes in the frequency range of interest; and to be able to establish correspondence between companion modes in the analysis model in the reduced set of DOF.
- At present, the current state-of-the-art process for deriving a modal model from test data can be thought of as a two-level fitting process. First, frequency response functions (FRF) are obtained through spectral analysis methods using acquired time history data. FRF's relate the response at the measurement DOF to the input and the excitation DOF in the frequency domain. Modal parameters are then determined from these FRF data via any of a number of nonlinear estimation algorithms. Each of these steps can be sensitive to decisions made by the data analyst as well as to numerical and algorithmic uncertainties.

Each of the above issues has been addressed during the course of the structural system identification project. One significant software tool that originated from these concerns is Optimal Test Design (OTD), a Matlab-based package specifically designed to address the selection of optimal response and excitation DOF for modal testing.

2.2 Modeling/Analysis Software

Even though no technological restriction on model type exists, Sandia analysis models generally take the form of finite element models (FEMs). For such models, there are a number of methodologies capable of reconciling any differences that exist between test and analysis in a manner that accounts for the uncertainty in both the experimental data and the model parameters. A primary focus of this research was one estimation methodology that is ideally suited to determining physical parametric quantities that are present in the FEMs. A software package, NASDSA, was developed to extract the necessary information from MSC/NASTRAN models using its pre-existing design sensitivity analysis (DSA) mechanisms. Two other codes were also developed: NASSID—a translator for communicating output from NASDSA to the parameter estimation code, SSID (a Sandia software tool using Bayesian estimation that will be described in Section 2.3); and SD2NAS—a package which facilitates the return to MSC/NASTRAN from SSID with an updated parameter set.

2.3 Test/Model Reconciliation Codes

The approach taken was to update user-specified parameter sets using modal data (modal frequencies and elements of mode shape vectors) as criteria, or *measurements*. FEM-based physical parameters are the *state* variables upon which the measurement predictions rely. The update method chosen is the probabilistic nonlinear parameter estimation scheme known as iterative Bayesian Estimation. Similar to other iterative approaches, this technique requires that a linearized relationship between the measurements and state for each iteration cycle be supplied. In the linearized formulation, the state parameters enter into the physics through first order sensitivity matrices which are calculated local to the current estimates of the FEM parameter values. Each estimation cycle results in new paramaters updates and, using these new values, a first-order Taylor series approximation to the updated system mass and stiffness is then performed. Finally, an new eigensolution is calculated for use both in comparing current analysis eigendata to that of the pre-selected test eigendata and in the generation of the sensitivity data for the ensuing estimation cycle.

SSID, an acronym for Structural System IDentification, is a Sandia software package which performs the tasks outlined in the previous paragraph based on specifications input by an analyst. SSID has gone through several significant revisions and code rewrites during the course of the system identification program. This code now represents a state-of-the-art parameter estimation capability. Recent applications entail models on the order of 50–75,000 DOF and include government as well as commercial applications. Current capabilities include:

- Sparse matrix storage and linear algebra incorporating software from Prof. Yousef Saad at the University of Minnesota;

- A Lanczos-based eigensolver, ARPACK, developed at Rice University by Prof. Dan Sorensen, et. al.;

- A sparse, direct solver based on a new Cholesky decomposition technique. This solver is a derivative of SPARSPAK and is the contribution of Dr. Esmond Ng at ORNL;

- A sophisticated mode tracking algorithm developed by Mike Eldred of Sandia, Structural Dynamics and Vibration Control Dept. Modal criteria require that mode correspondence between test and analysis models be established.

3. Selected Publications

In Appendix A, several publications are presented that serve as examples of the types of applications that were addressed during the period of performance of the LDRD. References are provided in the individual articles as well as more in-depth technical detail on the topics of interest. A significant number of these publications have led to widespread interest in this research external to Sandia, and have helped to establish Sandia as a recognized leader in this area in the technical community. Furthermore, this work is now an essential element of the broader research topic of uncertainty quantification at Sandia.

4. Concluding Remarks

Structural system identification for structural dynamics applications has been a topic of interest for many years. For example, The Aerospace Corporation and The Jet Propulsion Laboratory were investigating techniques for use in qualifying payload models as early as the late '60s. Offshore oil companies explored use of the technology for application in monitoring the structural health of offshore oil rigs in the early '70s. Sandia's initial foray followed closely behind these efforts. However, practical application and more in-depth technology development were hindered by the lack of cohesive and general software tools necessary for laying the foundation for the development of a more extensive and uniform experience base. As a direct result of work under the current program, this is now possible at Sandia through the use of software and methodologies developed through this research. These resources have resulted in work partnerships and Memoranda of Understanding with other government agencies and National laboratories, as well as Cooperative Research and Development Agreements with commercial concerns.

Appendix A
Selected Publications

IMAC XI

A MODAL TEST OF A SPACE-TRUSS FOR STRUCTURAL PARAMETER IDENTIFICATION*

Thomas G. Carne and
Randall L. Mayes
Sandia National Laboratories
P. O. Box 5800
Albuquerque, NM 87185

Marie B. Levine-West
Jet Propulsion Laboratory
California Institute of Technology
Pasadena, CA 91109

ABSTRACT

The Jet Propulsion Laboratory is developing a large space-truss to support a micro-precision interferometer. A finite element model will be used to design and place passive and active elements in the truss to suppress vibration. To improve the model's predictive capability, it is desirable to identify uncertain structural parameters in the model by utilizing experimental modal data.

Testing of both the components and the system was performed to obtain the data necessary to identify the structural parameters. Extracting a modal model, absent of bias errors, from measured data requires great care in test design and implementation. Testing procedures that are discussed include: verification of non-constraining shaker attachment, quantification of the non-linear structural response, and the design and effects of suspension systems used to simulate a free structure. In addition to these procedures, the accuracy of the measured frequency response functions are evaluated by comparing functions measured with random excitation, using various frequency resolutions, and with step sine excitation.

INTRODUCTION

The Jet Propulsion Laboratory (JPL) has been developing the technology for a mission known as the Focus Mission Interferometer, which is a large, partial aperture telescope [1]. The truss structure which supports the optical instrumentation spans thirty meters. Proper optical performance requires controlling relative positions to the nanometer level. Figure 1 shows an artist's depiction of the Focus Mission Interferometer. The Micro-Precision Interferometer (MPI) is a half-scale, ground-based testbed for the development and test of the technologies necessary for the Focus Mission Interferometer. The MPI testbed has only a single-sided optics boom rather than double-sided as shown in Figure 1. The MPI also contains the scaled metrology boom and the tower, thus creating a truss-structure with three nearly orthogonal elements. (7m x 6.3m x 5.5m) The metrology boom is perpendicular to the optics boom but has a slightly acute angle with the tower. Figure 2 shows the MPI in the test laboratory.

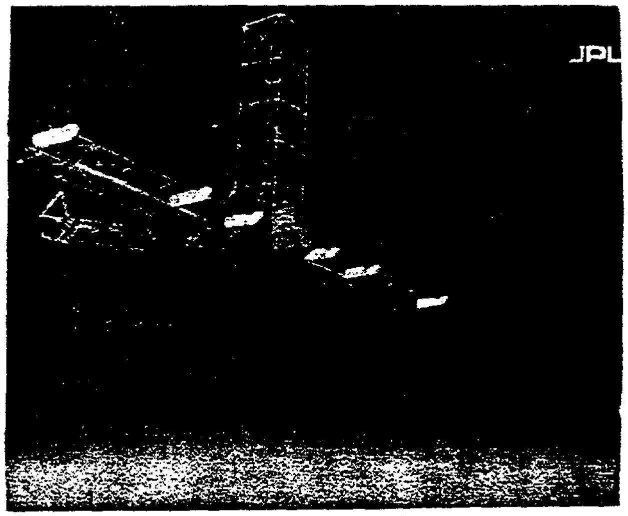

Figure 1: Focus Mission Interferometer

The partial aperture telescope simulates a full aperture system with performance increasing with the distance between the apertures. However, in order to maintain the performance, the translations and articulations of the optical equipment must be controlled to the nanometer level in spite of a vibratory environment due to onboard equipment. Vibration suppression will be achieved through a layered approach, consisting of vibration isolation, structural control, and optical control [2].

The finite element model will be used extensively to design the vibration suppression system, and consequently it is critical that it be accurate and predictive. The model will have a variety of

---

* a portion of this work was performed at Sandia National Laboratories under the support of the U.S. Department of Energy contract number DE-AC04-76DP00789.

uses including: helping to determine the attachment locations for the various spacecraft components, simulating the various control designs, evaluating configuration changes, and identifying the optimal placement of active and passive elements.

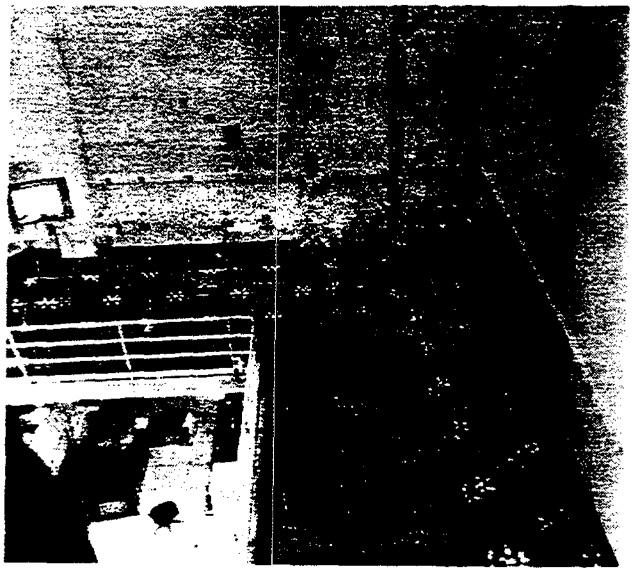

Figure 2: Micro-Precision Interferometer Testbed

To develop a finite element model with the desired fidelity, a system identification process will be used to identify uncertain structural parameters in the model [3, 8]. The emphasis will be on the structural parameters rather than the mass and stiffness matrices, because we want to develop a predictive structural model which is applicable even when physical changes are made to the system including adding large masses, adding structure, moving optical instruments, or the insertion of damping elements. Measured modal data will be a key element in the system identification process, and consequently precautions must be taken to ensure that the data are appropriate. These procedures and some of the results from the testing are described in this paper. First, some component testing is described which was performed to gain information on the local behavior of the strut elements, in particular, the end-joint flexibility. Then the system testing will be described with the various procedures to ensure relevant experimental data. Lastly, some of the results from the identified finite element model will be included and compared to the test data, although the model/test reconciliation is covered extensively in [3, 9].

COMPONENT TESTING

The MPI is a truss constructed by assembling a large number of similar strut elements, replicated throughout the structure. These struts are interconnected at aluminum node balls with a threaded connection that is locked using a B-nut. Figure 3 displays an expanded view of the connection hardware which creates the joints between the struts and the node balls. Although the individual struts could be easily modeled, the stiffness of the joint which interconnects all of these elements would be most difficult to analytically predict. The interconnecting joint stiffness may not be important for the first few modes of vibration (a pinned joint assumption would probably be sufficient); however, these joint stiffnesses will certainly become important for the higher modes. This concern motivated the formulation of a separate component test plan.

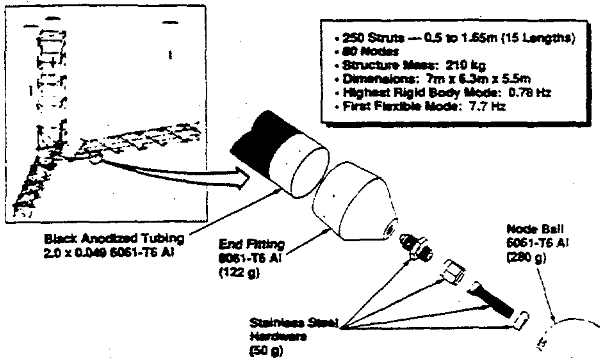

Figure 3: Detail of Interconnecting Joint

The component test plan had two objectives. The first objective was to provide modal data that could be used to identify the nominal stiffness parameters associated with bending and axial deformations of the struts, strut end-caps, and particularly the B-nut connection joint. The second objective was to provide modal data that could lead to deterministic quantifications of phenomena that would cause variations from the nominal parameters. The phenomena included: amplitude of vibration, static strut loading, B-nut installation torque, and B-nut length. Reference [3] contains more details of these test procedures and results than can be included here.

Figure 4 shows seven different configurations of the balls, struts, and B-nuts that were tested to provide modal data for the identification of the component structural parameters. By using multiple configurations, this provides redundant data for a better identification of the parameters. Each configuration was suspended by soft bungee cords and string so that the rigid body modes would be sufficiently separated in frequency from the first elastic modes. A photo of one of the configurations is displayed in Figure 5. For each configuration the first axial and first bending modes were measured using transient excitation in both the axial and lateral directions. Modal data was extracted from frequency response functions (FRF's), and Table 1 lists the results of these tests. The modal frequencies along with the mode shapes were used in conjunction with finite element models of these configurations to identify the structural parameters, in particular the joint flexibilities [3].

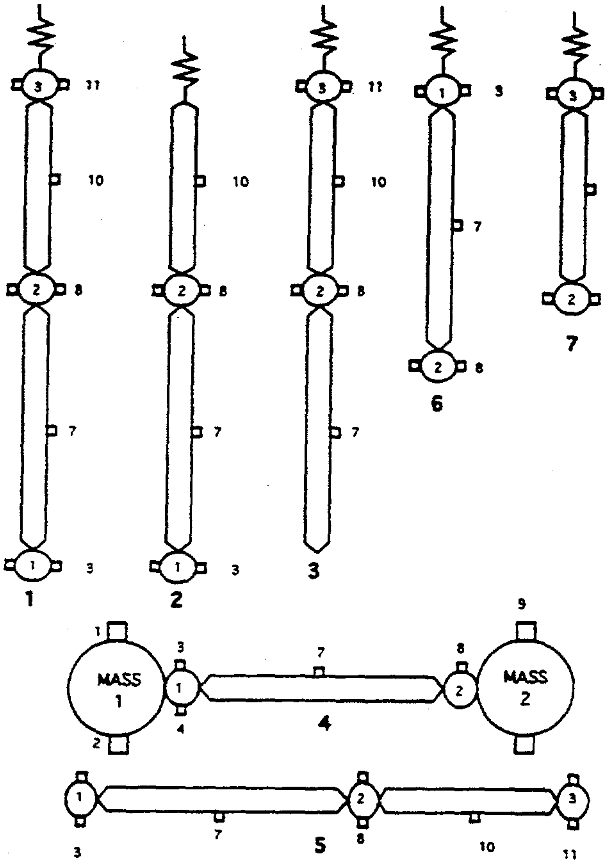

Figure 4: Seven Configurations for Component Testing

Table 1: Modal Parameters from the Component Tests

	Bending Properties		Axial Properties	
Configuration	Freq (Hz)	Damping (&)	Freq (Hz)	Damping (&)
1	12.26	1.0	826.3	0.1
2	15.91	0.5	942.2	0.1
3	13.95	0.4	1013.2	0.1
5	12.09	0.5	825.5	0.2
6	133.56	0.6	1202.3	0.3
7	165.5	0.4	1518.5	0.1

MODAL TEST OF THE ENTIRE STRUCTURE

In contrast to the component testing, which was designed to exercise localized behavior in simple structural elements, the system test exercises the entire MPI structure with all the structural elements interacting. The primary objective of the system test was to provide laboratory measurements of the structural dynamics and to provide data for the reconciliation of the analytical model and the test. This objective may sound trivial, however for a system identification test, one must concentrate on providing data that can be used for reconciliation, not just test data. One must be sure that the model describes properly and completely that which is being tested and that the structure being tested is in the model. As usual, a modal test was used for the system test (in contrast to, for example, static testing or frequency response testing) since the modes can define the structural dynamics, are fairly easy to compute with the model, and tend to globally exercise the structure. Figure 6 show the MPI in the laboratory at JPL; one can easily see the interconnecting struts and node balls in this photo.

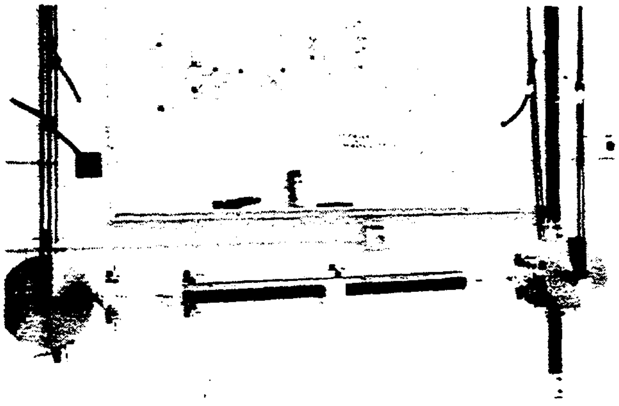

Figure 5: Configuration 4 Suspended in Lab

The structure was supported in the laboratory to simulate free boundary conditions which would best mimic the operational environment of the MPI. Initial plans were to measure all elastic modes below one hundred Hz, but the upper limit was reduced to sixty Hz due to the high modal density occurring in the range above sixty Hz. Another feature of this system identification test was the use of multiple configurations of the structure, both to test the validity of the identified model and to provide additional experimental data in which the structure was being exercised in a different manner. The various configurations included both the addition of significant mass items and the inclusion of extra struts in the structure. In this report we will show results from just the primary configuration.

Supporting the structure, so that free boundary conditions were well approximated, was a very important aspect of the pre-test planning. If the support does not have minimal effects on the elastic modes, then the support structure must be included and modeled with sufficient detail to account for the effects on the elastic modes. If the support approximates well the free boundary conditions, then only a simplistic model of the support needs to be included to account for the small changes to the modes. For this test the MPI was supported from three points with soft coil springs to produce rigid body modes of less than one Hz. The coil spring suspension will be discussed further in this section; this suspension did introduce additional structural dynamics to the total structure (MPI plus support) that were not originally included in the model.

After examining the mode shapes, frequency response functions, and mode indicator functions as predicted by the model, two shaker locations were chosen at the ends of the optics and metrology booms. The directions of the input forces were in the planes of the end-faces of the booms and oriented to produce twist of the booms. Figure 7 show one of the shakers attached to the MPI, using a long flexible rod to limit side loads and moments on the force transducer. Portable fifty-pound shakers were used for excitation. The modal test of the primary configuration was actually performed by two separate test groups (Sandia and JPL) using different instrumentation, excitation, and data acquisition hardware separated by months of time. The primary objective of the Sandia test was to accurately evaluate the mode shapes for system identification, whereas that of the JPL test was to determine the variations in the modal parameters resulting from different testing techniques. Later in this sections the results from the two tests are compared.

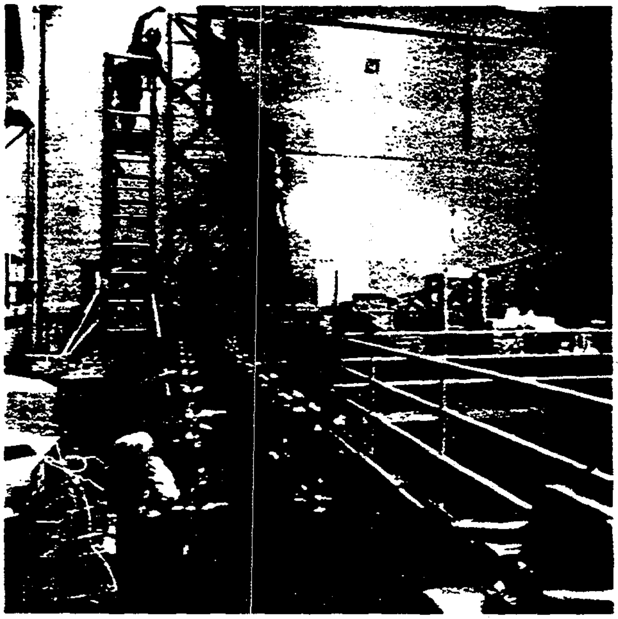

Figure 6: MPI In Test Lab

Instrumentation Plan

For the Sandia test, every one of the eighty node balls of the truss structure was instrumented with a tri-axial accelerometer; while for the JPL test only 127 accelerometers were available. More detailed mode shape information was collected for the Sandia test due to the uncertainties in the data requirements for the model reconciliation task. In addition to the eighty balls of the truss another twenty-four accelerometers were included at various locations including the midpoint of some of the longer struts and at suspension points.

For the JPL test, the placement of the accelerometers was selected to optimally measure the desired mode shapes. A modal analysis was first performed using the finite element model with the full set of degrees of freedom (dof), and the resulting mass-normalized mode shapes were stored. The rotational dof's and those dof's which would not be instrumented were then removed through Guyan reduction. Then a second modal analysis on the reduced model was performed, and the cross-orthogonality of the reduced modes with the original modes is verified by computing:

$$\Phi_f^T M_r \Phi_r$$

Figure 7: Shaker Attachment to MPI

where M_r and Φ_r are the Guyan reduced mass and eigenvector matrix, and Φ_f is the matrix of eigenvectors of the full order system in which the components corresponding to the uninstrumented dof's have been omitted.

Ideally, the resulting cross-orthogonality matrix should be the identity matrix for the modes of interest. In practice, if the diagonal values are greater than 0.9 and the cross terms are small, it can be assumed the the omitted dof's can be reduced without inducing modal coupling or affecting the reliability of the measured mode. This iterative process is continued until the best dof's for instrumentation have been identified. For the MPI, 116 accelerometers were distributed over sixty-nine of the eighty nodes. The optimally placed sensors produced a cross-orthogonality of 0.93 or better for twenty-two global modes below 130 Hz. Ten additional accelerometers were placed at the mid-spans of the six longest struts to measure their local behavior.

Reciprocity and Linearity

After the MPI was completely instrumented with accelerometers and cabling, reciprocity was measured between the two shaker attachment locations. An acceleration-to-force FRF was measured from the driving-point accelerometer at Shaker 2 to the force transducer at Shaker 1 with Shaker 2 disconnected from the structure. Then the reciprocal FRF was measured with Shaker 1 disconnected. Reciprocity requires a linear elastic structure, but by disconnecting the non-exciting shaker it can also detect shaker attachment effects. Figure 8 displays an overlay of the two reciprocity functions. One function is plotted with a solid line, and the second function is plotted with a line plus circles. Examining the figure, one can see that the reciprocity functions are indeed very repeatable evidence that the structure is linear at the excitation levels of interest and that the shakers had been attached without changing the structure.

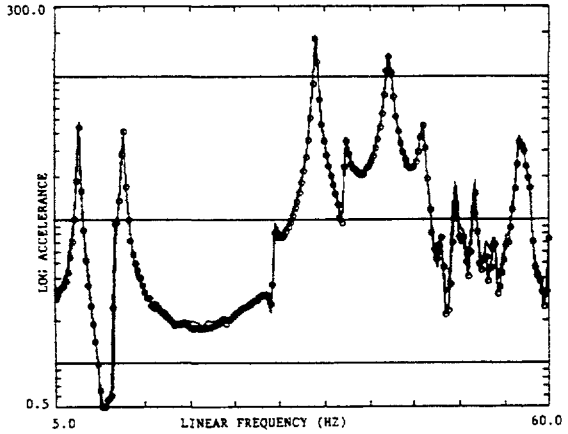

Figure 8: Overlay of Two Reciprocity Functions

To verify the linearity of the structure over a broader amplitude range, the structure was excited with a transient input and then allowed to free-decay for twelve seconds. An accelerometer signal was measured, sampling at 512 Hz, while the response decayed from approximately 0.2 to 0.02 g's. By exciting the structure in different locations in specific directions, one could primarily excite particular modes. A time history from one of these tests is shown in Figure 9. The time histories were then digitally filtered so that one of the lowest modes would dominate the response. This data was then analyzed in overlapping segments using ERA [4] to calculate the dominant modal frequency as a function of time and consequently as a function of vibration amplitude. The calculated modal frequency for each segment is plotted for the two modes in Figures 10 and 11. The vertical axis on the plot has been tremendously expanded so that the variation in the calculations can be observed. The solid line on the plot is the best fit straight line through the data points and clearly reveals that these two modal frequencies are independent of the amplitude of vibration for the levels tested.

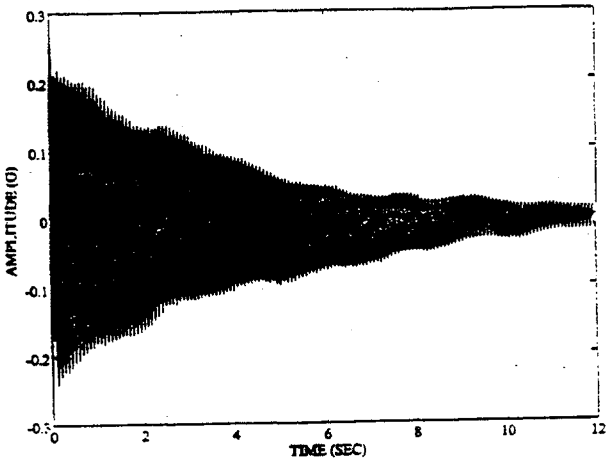

Figure 9: Decaying Response Time-History

Data Acquisition and Results

After the reciprocity and linearity evaluations were performed, the actual modal test proceeded with measurement of the FRF's. Although groups of accelerometers were sequentially switched into the data acquisition system, the instrumentation remained unchanged throughout the entire modal test to ensure the structure remained unchanged during the test. Burst random inputs were used as the excitation. Figure 8 shows the reciprocity FRF's, but these are not atypical of the measured FRF's. From the total set of FRF's the modal parameters were estimated, using Polyreference [5] for the JPL test and a combination of Polyreference and a frequency domain mode-shape algorithm [6] for the Sandia test.

The modal frequencies from the two tests are compared in Table 2 with notations describing the characteristics of each mode; only the elastic modes are included in the table. For the first eleven modes, the measured frequencies are remarkably consistent, considering that different people, hardware, and data acquisition were used on these two tests. The average difference between these eleven modal frequencies is only 0.4 percent.

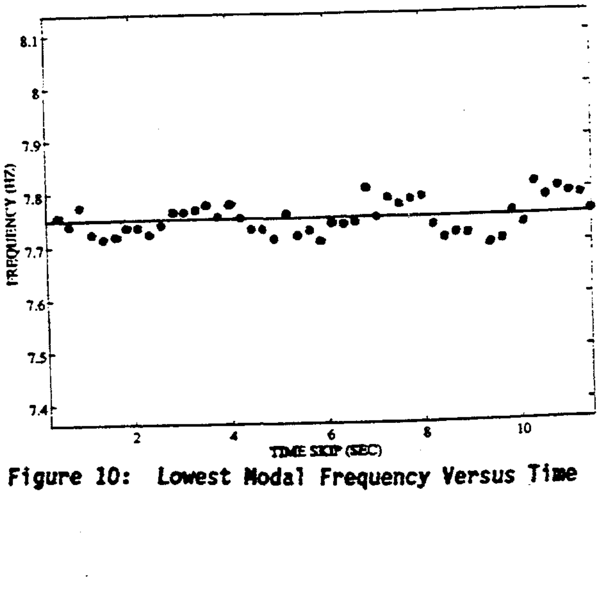

Figure 10: Lowest Modal Frequency Versus Time

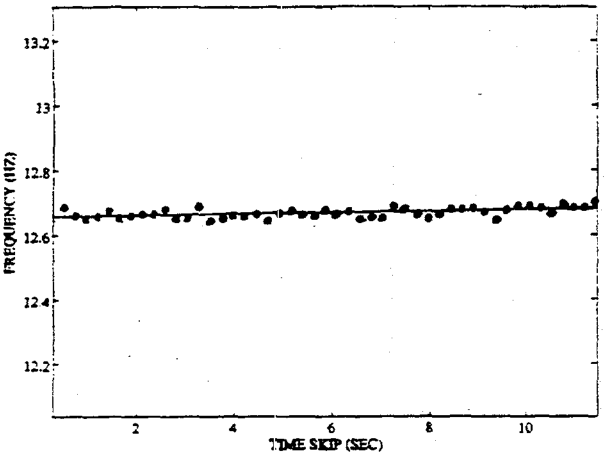

Figure 11: Third Modal Frequency Versus Time

TABLE 2 - MEASURED MODAL FREQUENCIES FROM THE SANDIA AND JPL TESTS

	MODAL FREQUENCIES (Hz)		
MODE NO.	SANDIA TEST	JPL TEST	NOTATION
1	7.75	7.77	System Mode
2	11.65	11.64	"
3	12.67	12.71	"
4	29.36	29.55	"
5	34.06	34.22	"
6	37.34	37.50	"
7	42.25	42.56	"
8	46.04	46.12	"
9	48.09	48.01	Spring surge
10	49.50	49.69	System mode
11	50.63	50.97	"
12	51.69	52.15	Strut local bending
13	51.97	52.52	Probably orthogonal local bending
14	53.00	53.21	System mode
15	53.95	53.92	System or spring
16	56.82	56.93	Spring surge
17	57.26	-	Very low amplitude
18	58.02	58.08	System mode
19	60.04	60.00	System mode

Note that mode 9 is described as a spring surge mode; this mode was due to structural dynamics within the coil spring. This is behavior in the structural support that is definitely undesirable, as it greatly complicates the identification of modes of the structure using experimental data only. This structural dynamic property of the springs had not been included in the finite element model of the suspension (the suspension was modeled as massless, linear-spring elements). In fact, these modes were particularly troublesome because they appeared to be system modes, but with relatively low amplitudes. However, in the reconciliation process there were no analytical mode which corresponded to these modes. Experimentally, the spring surge modes were identified by repeating the modal test with foam rubber wrapped around the spring coils, thus increasing the damping internal to the spring. With the damping material inserted, two of the modes literally disappeared from the frequency response functions, and these are indicated as spring surge in the table as modes 9 and 16.

Mode 12 in the table is unique in that it is the local strut mode for the longest strut in the truss (lowest frequency). The Sandia test found that mode approximately 0.5 Hz lower in frequency than the JPL test. The Sandia test used instrumentation at the center of the strut that was approximately eight grams heavier than the JPL test, and with the aluminum tube weighing approximately 900 grams, the mass loading effect should reduce the frequency by approximately 0.9%. This explains the difference between the two measured values. Mode 13, which has been identified as the orthogonal strut bending mode, also reveals a difference of about 0.55 Hz. Examining the remainder of the table shows some additional system modes, a mode that Sandia identified, but JPL did not (probably another spring surge mode), and mode 16 which was clearly identified as a spring surge mode. Overall, the fine correlation between the two tests is extremely reassuring regarding the validity of the modal data.

The mode-shapes for the modes listed in Table 2 were identified using the FRF's, and Figure 12 displays the first six modes. The deformed shape has been plotted over the undeformed mesh indicated with a dashed line. The first three modes have various scissoring motions involving different booms and the tower, while subsequent mode-shapes become more complex in their descriptions.

As the last step in the analysis of the modal data, FRF's are synthesized using the experimental modal parameters as the basis. These are compared to the original measured data to evaluate how closely the modal model synthesis fits the measured data. Figure 13 and 14 show two of these comparisons. In both figures, there are two functions plotted. The solid line is the measured data, and the line plus circles is the synthesis. Figure 13 is for the cross-driving-point FRF, and Figure 14 is for a response in the tower due to input at the end of the metrology boom. One can see that the both syntheses reproduce the measured data quite well which gives great confidence to the data analysis portion of the modal test.

Frequency Response Functions

In an effort to qualify the experimental technique which used the burst random excitation, the FRF's were also measured using step sine excitation. In Figure 15 two driving point FRF's have been overlaid, one using burst random with twenty-five averages and other using step sine. Both have a frequency resolution of 0.93 Hz, and the magnitudes are plotted from six to sixty Hz. They virtually overlay each other, although if one could look very closely, the peaks and valleys are a little sharper with the step sine. Of course, this particular structure is somewhat ideal in that it is very linear and lightly damped. The data acquisition time for the step sine was approximately twelve times longer than the burst random using twenty-five averages. Consequently, for this structure at least, one could conclude that FRF's measured with burst random are perfectly adequate and are much faster to acquire.

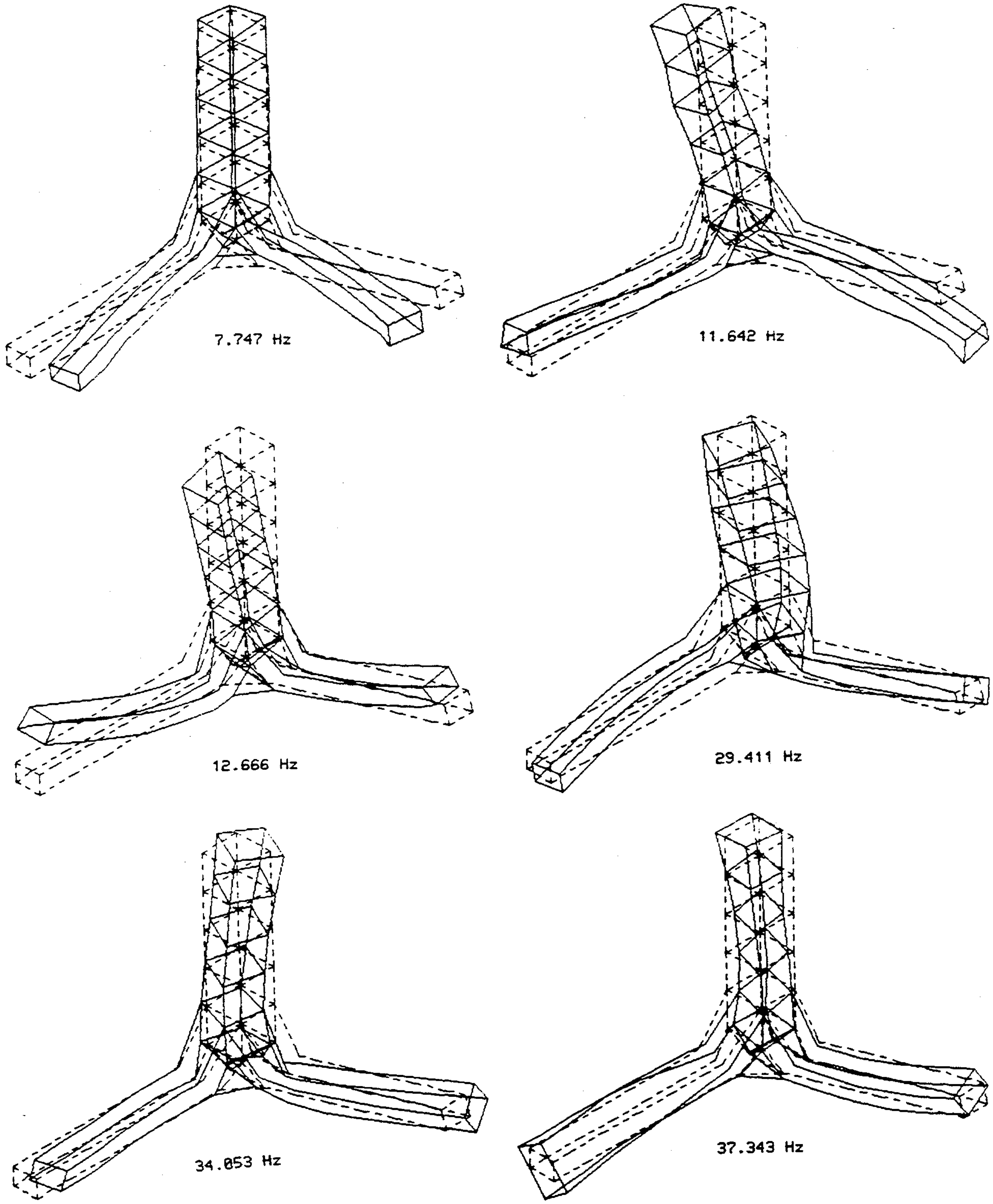

Figure 12: Mode Shapes of the MPI

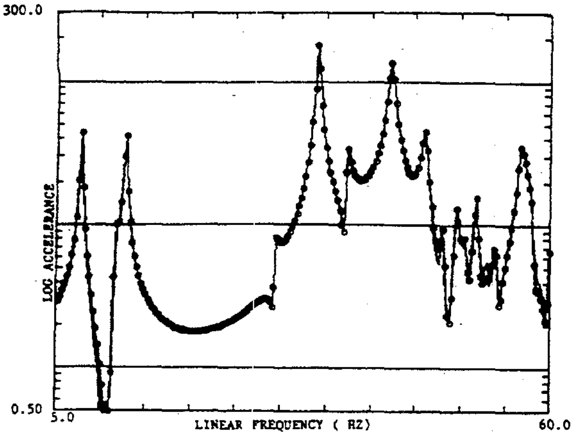

Figure 13: Synthesis of Cross-Driving Point FRF Overlaid on Measured FRF

To further evaluate the FRF measurement procedures, a driving point FRF was again measured with burst random excitation; but in this case the frequency resolution was varied. Figure 16 show three FRF's overlaid, plotted from five to fifteen Hz, that have been measured with three different frequency resolutions, 0.093, 0.041, and 0.014 Hz. Upon close examination one can see that the peaks and valleys have been missed somewhat by the FRF's with the coarser frequency resolution, although recall that this structure is very lightly damped. Using these FRF's, the modal frequencies and dampings were identified (Table 3). There appear to be no trends in the data, just variations due to the estimation process. In fact, the identified frequencies are incredibly consistent, with the damping values varying more, but not in any consistent manner. Of course, the consistency of the identified parameters is to be expected if one examines Figure 16 closely. Even though the peaks have been missed with the coarser resolution, the remainder of the FRF function overlays almost perfectly, which shows that there has not been significant leakage for the coarser resolution.

Table 3: Effect of Frequency Resolution on Identified Modal Parameters

$\Delta F = 0.094$ Hz		$\Delta F = 0.041$ Hz		$\Delta F = 0.014$ Hz	
Freq (Hz)	Damp (%)	Freq (Hz)	Damp (%)	Freq (Hz)	Damp (%)
7.768	0.17	7.766	0.16	7.765	0.19
11.641	0.13	11.640	0.16	11.640	0.14
12.706	0.10	12.707	0.13	12.703	0.13

COMPARISON OF MODEL AND TEST

The identification of the finite element model is the primary thrust of [9], consequently only a few details of the results will be included here. The objective of the identification process is to validate a model that is accurate up to sixty Hz, and that process is currently ongoing. In Table 4, initial modal frequencies and MAC values for the first eight elastic modes are included. Here, the non-squared version of the MAC [7] is used as defined by

$$\mathrm{MAC} \equiv \mathrm{MAC}_{ns} \equiv \frac{\phi_a^T \phi_e}{|\phi_a|\,|\phi_e|}$$

TABLE 4: COMPARISON OF TEST AND ANALYSIS MODAL DATA

MODE No.	Test Frequency	Analysis Frequency	Frequency Error (&)	MAC
1	7.75	7.86	1.4	0.998
2	11.65	11.68	0.3	0.997
3	12.67	12.77	0.8	0.997
4	29.36	29.29	-0.2	0.998
5	34.06	34.18	0.4	0.999
6	37.34	37.37	0.1	0.995
7	42.25	42.43	0.4	0.996
8	46.04	46.08	0.1	0.996

The agreement between the test and analysis, shown in Table 4, appears to be quite good. There are very small differences in the frequencies, although the biggest difference is for the first mode. The MAC values are very close to unity, an indication of good correspondence of the mode-shapes. However, it is important to understand that a MAC comparison of two mode-shapes is very forgiving of random errors.

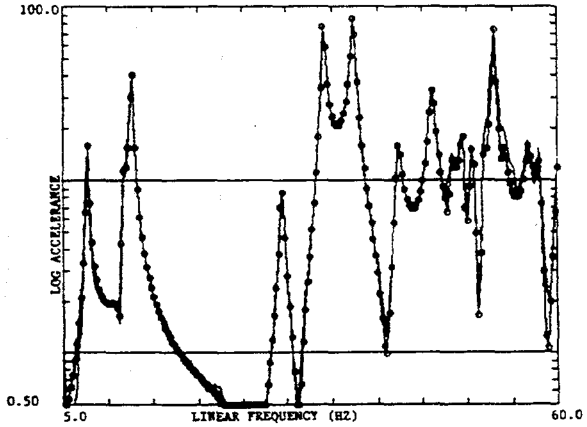

Figure 14: Synthesis of a Tower FRF Overlaid on Measured FRF

CONCLUDING REMARKS

The JPL MPI structure is a very linear, repeatable, and lightly damped structure and thus, it is an excellent testbed for evaluating system identification concepts. The system identification process requires testing, analysis, and test/analysis reconciliation. Testing for the MPI was divided into component-level and system-level experiments. The primary objective of the component testing was identification of the joint stiffness which would be virtually impossible to model a priori. The system level test exercises the entire structure and is the final "test" of the reconciled model. However, both the test and the model should be equal partners in the reconciliation process. The system test of the MPI was performed by two separate teams using different equipment and separated in time by weeks. The agreement in the modal frequencies for the first nineteen elastic modes up to sixty Hz was very reassuring. Synthesized FRF's, using the identified modal parameter, agreed very well with the measured FRF's lending more confidence to the identified modes. There were problems with the suspension system, in that the springs had very lightly damped modes within the frequency band of interest, making clear descriptions of some system modes difficult.

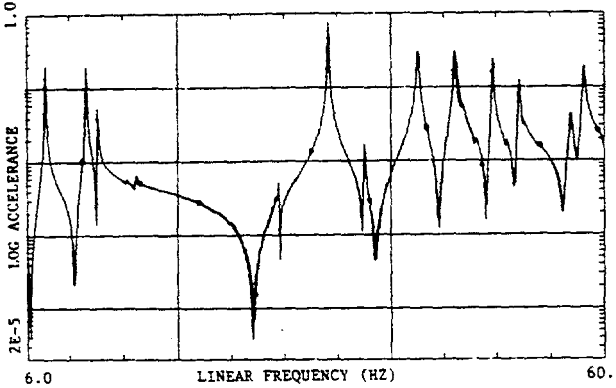

Figure 15: Step Sine FRF Overlaid on Burst Random FRF

For a successful system identification process, there are a few key points that need to be stressed. Communications between the analyst and the experimentalist is essential, for each must know the compromises and assumptions the other has made. The experimentalist must plan and measure the data with the reconciliation process in mind, not just produced data. One needs to be sure that the model describes that which has been tested, and that the test article is that which has been modeled. Finally, in planning instrumentation, one should instrument all support connections to the structure all the way to solid ground.

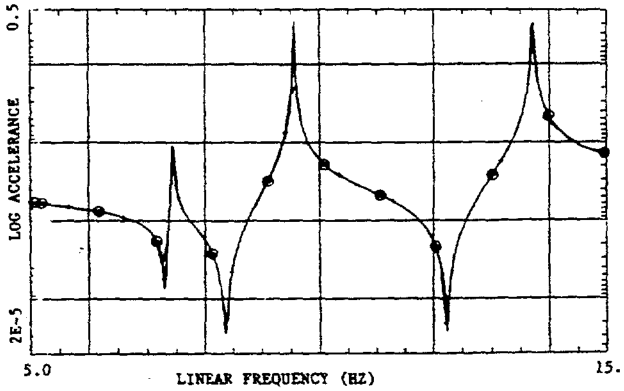

Figure 16: Three Burst Random FRF's Overlaid with Δf = 0.093, 0.041, 0.014 Hz

ACKNOWLEDGEMENTS

Support from the entire JPL CSI team is greatly appreciated, particularly Greg Neat and Lee Sword.

REFERENCES

[1] R. A. Laskin and M. S. Martin, "Control/ Structure System Design of a Spaceborne Optical Interferometer," Proceedings of the AAS/AIAA Astrodynamics Specialist Conference, 1989.

[2] J. T. Spanos, et. al., "Control Structure Interaction in Long Baseline Space Interferometers," In Proceedings of 12th IFAC Symposium on Automatic Control in Aerospace, Ottobrunn, Germany, 1992.

[3] J. R. Red-Horse, et. al., "System Identification of the JPL Micro Precision Interferometer Truss: An Overview," Proceedings of the Third International Conference on Adaptive Structures, November 9-11, 1992, San Diego, CA.

[4] Juang, J. N. and Pappa, R. S., "An Eigensystem Realization Algorithm for Modal Parameter Identification and Model Reduction," Journal of Guidance, Control and Dynamics, Volume 8, No. 5, September - October 1985, pages 620-627.

[5] H. Vold and G. F. Rocklin, "The Numerical Implementation of a Multi-Input Modal Estimation Method for Minicomputers," In Proceedings of the 1st IMAC, pages 542-548, 1982.

[[6] R. L. Mayes, "A Multi Degree of Freedom Mode Shape Estimation Using Quadrature Response," In Proceedings of the 11th IMAC (to appear), 1993.

[7] D. J. Ewins, "Modal Testing: Theory and Practice," John Wiley and Sons, 1984.

[8] M. B. Levine-West, "High Fidelity Predictive Models of Structures on Orbit," Report D-10113, Jet. Propulsion Laboratory, California Institute of Technology, Pasadena, CA, September 1992.

[9] J. R. Redhorse, E. L. Marek, and M. Levine-West, "System Identification of the JPL Micro Precision Interferometer Truss: Test-Analysis Model Reconciliation," Proc. 34th SDM, La Jolla, CA, 1993.

Submitted to the 1st International Symposium on
Microdynamics and Accurate Control
Nice, France.
November 30 - December 3, 1992.

A SYSTEMS APPROACH TO HIGH FIDELITY MODELLING

Dr. M. Levine-West, Dr. J. Red-Horse, E. Marek

Jet Propulsion Laboratory, Pasadena, California, U.S.A.
Sandia National Laboratory, Albuquerque New Mexico, U.S.A.

1. Introduction

Structural controls and dynamics research will have to face great challenges in the coming years to meet increasingly high precision requirements on the stability, pointing and measurement accuracy of future space missions [1]. In particular, attention will be given to methods which will be able to reliably estimate models of large flexible structures in space, and accurately predict nanometer-level response due to micro-g disturbances in a low gravity environment over a very wide frequency and thermal band. Such concern arise in problems involving structural optimization, and optimal placement of dampers and active members for vibration suppression [2]. These predictive models will have to be constructed from knowledge gained from both ground and on-orbit tests.

Recent advancements in the fields of experimental methods, modal identification and model updating are progressively improving the ability of analytical models to predict dynamic response and performance [3,6]. However, each of these areas of research are conducted separately. Typically, the model identification technique is validated from a single set of "measured modes", response time histories or frequency response functions. Little attention is usually given as to how these modes were excited and identified or what kind of input excitation was used to produce the structural response. Also, considerations such as the reliability of these "measured data", or how well the data represents the parameters within the analytical model are rarely addressed. Accuracy to the level required for high precision space missions can only be achieved if the experimental testing, data reduction and analytical model updating are integrated together into a single process.

A study was undertaken at the Jet Propulsion Laboratory (JPL) to identify candidate approaches to the reliable development of high fidelity predictive models of flight systems, such as the Focus Mission Interferometer (FMI), for which it is necessary to develop the capability to predict on-orbit motions to within an order of a nanometer [7]. The investigation studied the feasibility of integrating test and analyses methods for tuning of predictive flight models from both ground and on-orbit data. One of the objectives of the study was to select the class of models, the set of parameters, and the integrated procedure which could best predict the *on-orbit* response at any degree-of-freedom (dof) and over a wide frequency range. The structural test/analysis recursive system identification procedure, STARS-ID, described herein, proposes to obtain accurate flight prediction from a reliable ground model which is then altered for on-orbit environmental conditions [7]. Precision in the ground model is achieved from multiple iterations of the test/updating procedure, in which each iteration focuses on the identification of a selected set of parameters. The need for statistical information regarding the reliability of the performance prediction is also addressed. The paper describes the STARS-ID process, and its current implementation on tests initiated at JPL.

2. The Micro-Precision Interferometer (MPI)

JPL's Control Structure Interaction (CSI) team is developing the capability to create Micro-Precision Controlled Structures for flight systems such as optical interferometers [8]. These systems will be single payload structures with fixed truss geometry and are expected to fly in low earth orbit. The structures will be assembled with identical bays and components through multi-directional ball-joints, and secondary structures will be attached for the electronics and optical metrology equipment. Some members in the structure will be replaced by passive dampers or active members for vibration suppression and control purposes.

High fidelity predictive modelling for such structures must then consider identification techniques for modular designs of appendages and applicability of sub-component analysis. Many closely-spaced modes, resulting from manufacturing and assembly imprecision of the identical bays and struts, are expected to corrupt the higher frequency range, and complicate the identification process. Uncertainties and possible nonlinearities from the joints in μg gravity under μg internal disturbances must also be considered. On-orbit testing techniques could be implemented through controlled internal dynamic disturbances from the active members, and optical path length distortions could possibly be used as a performance index for predictability not directly related to modes or structural properties. Furthermore, moving sub-components, such as optical trolleys, could be used for on-orbit multiple-configuration testing.

Several testbeds exist at JPL to validate CSI vibration suppression, optical control, and structural optimization technology required for the FMI. All have the structural characteristics listed above, and could thus also provide a useful tool for STARS-ID technology validation. The MPI testbed is representative of a space-based interferometer comprised of two booms and a vertical tower, 7*m*x6.3*m*x5.5*m*, weighing 210*kg* (Figure 1). The testbed to date is a bare-truss structure, suspended by three linear extensional springs simulating the free-free on-orbit environment. The MPI will evolve in distinct phases over a number of years. A major structural configuration change marks each phase, each of which will be followed by a dynamic characterization of the modified structure and appropriate analytical model updates. The plan for repeating this test sequence a number of times provides an ideal opportunity to perfect STARS-ID modelling and identification approaches.

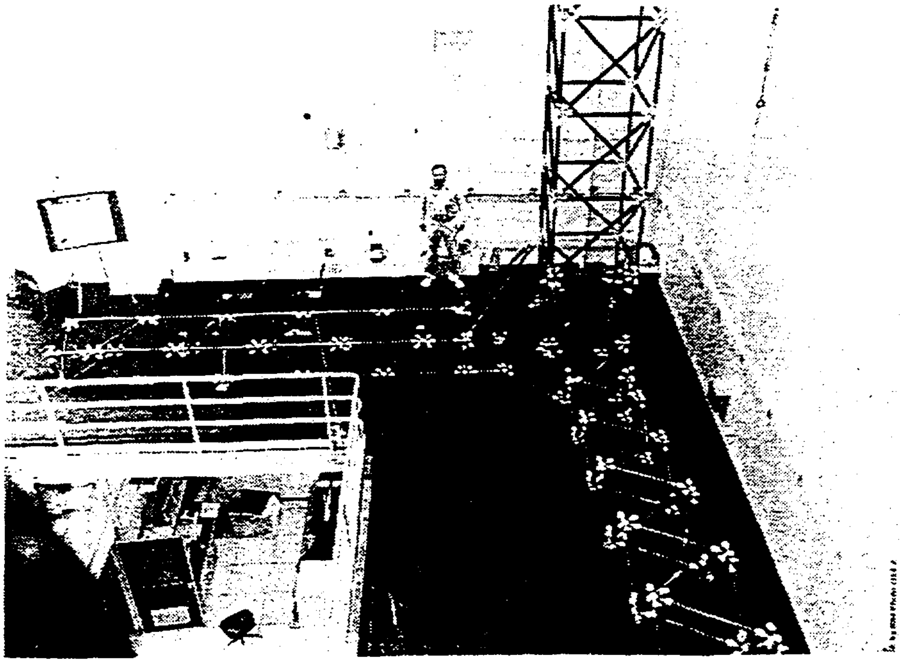

Figure 1. The Micro-Precision Interferometer Testbed at JPL.

3. Structural Test/Analysis Recursive System Identification: STARS-ID

The STARS-ID process to obtain high fidelity predictive models on-orbit is summarized in Fig. 2. Each step, numbered from *1* to *12*, represents existing areas of research in experimental and analytical structural dynamics, and are discussed in detail in [7]. Choices within each field are made on the premise of integrability to STARS-ID and applicability to accurate performance prediction for FMI-type structures. Based on the class of models selected to characterize the predictive structural performance measure *(Steps 1-2)*, the on-orbit model will be obtained by first identifying the parameters from ground experiments *(Steps 2-7)*, and then will be revised to accommodate on-orbit conditions (*Step 8)*. Model parameters can either identified directly from measured data (*Steps 3 & 5*), or can be identified through the intermediary of modal parameters identified from the measured data *(Steps 3-4-5)*. Because of uncertainties and lack of experience regarding the behavior of large flexible bodies in space, it will be necessary to perform a set of flight experiments to improve the model *(Steps 9-11)*. Behaviors or parameters which cannot be accurately predicted from ground-based experimental tests include nonlinearities in micro-*g* environment and response variations from thermal effects. Statistical methods are incorporated to assess the reliability of model parameter estimates resulting from random and systematic errors and model uncertainties and to quantify their effect on the predicted structural performance. Ultimately, these models must be flight verified to confirm their predictive accuracy and reliability *(Step 12)*.

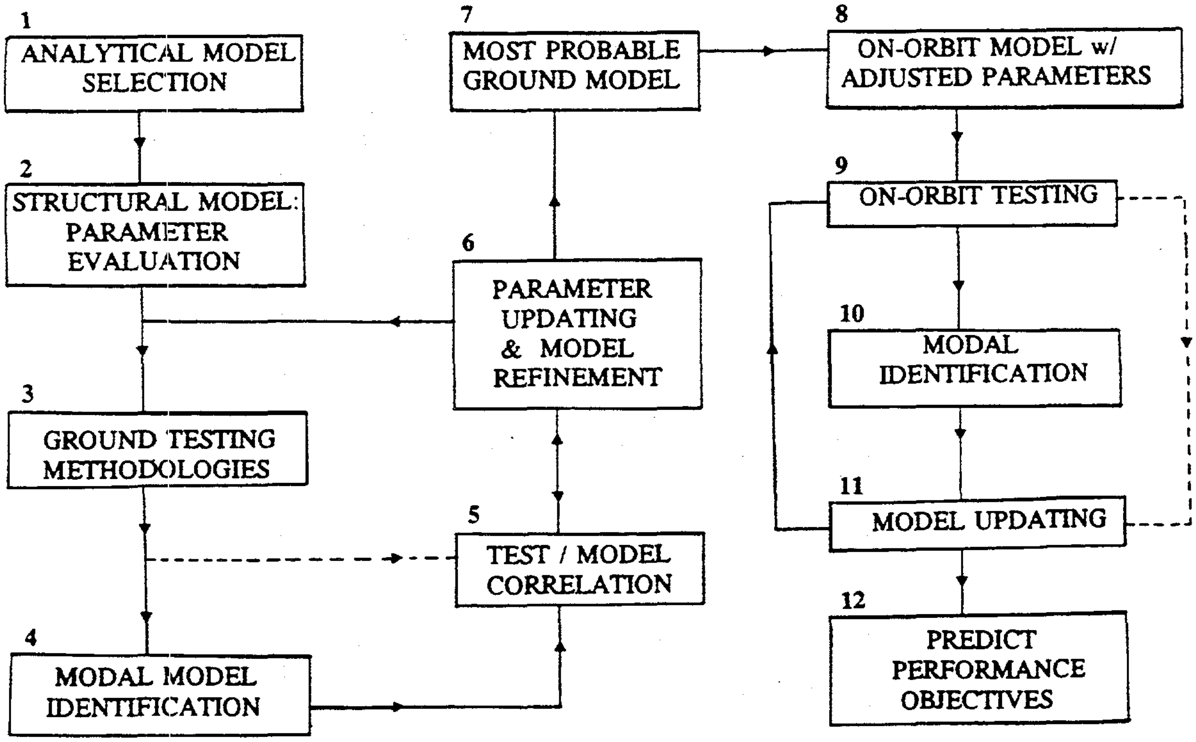

Figure 2. Flow-diagram for STARS-ID.

Existing techniques and methodologies pertinent to each of these field have been extensively reported and studied in [7]. Only certain critical issues and those methods that have been implemented to date on the MPI testbed will be reported hereafter.

3.1. Analytical Models for STARS-ID

Choices within each of the topics in Figure 2 are made on the premise of improvement in the prediction accuracy to on-orbit conditions. The first issue that must be resolved is the selection of the class of analytical model appropriate for on-orbit prediction. Classes of structural models based on identifying input-output transfer functions or impulse response functions can accurately evaluate the structural response at measured sensor and actuator locations from a particular set of tests, and is widely used in control systems design. However, they cannot be used to predict the response at other unmeasured input-output combinations or for different environmental conditions such as changes in gravity and temperature.

Among the most commonly used models for dynamic input-output representation, the ones suitable for prediction should be described by parameters which have a physical interpretation and are independent of the testing conditions and environment. In theory, structural models defined through the finite element method (FEM) could be used in conjunction with experimental information to update the physical parameters such as modulus of elasticity E, mass density ρ, and geometric properties $A, L, \ldots$ The dynamic loading, gravitational and environmental conditions could then be altered in the analytical model to predict on-orbit response. Furthermore, FEM techniques can be used to derive a full model of a large flexible structure from ground tests on its individual sub-components which are then assembled into the numerical model for on-orbit prediction of the complete structure [7].

The general equations of motions used to describe structural response with the FEM is:

$$[M]\,\{\ddot{q}\} + [C]\,\{\dot{q}\} + [K]\,\{q\} = \{F\} \tag{1}$$

where, *[M]* is the mass matrix, *[C]* is the damping matrix, *[K]* is the stiffness matrix, *{q}* is the displacement time history response of the structure, and *{F}* are the time histories of the applied forces. Within the FEM formulation, the physical parameters enter the equations of motions at the element level. Some of these parameters, such as lengths and cross-sectional areas, can be directly measured off the test structure, thus reducing the identification process to the more ambiguous global parameters such as those related to material properties, boundary conditions and joint mechanisms. Damping is typically assumed to be either proportional to *[M]* and *[K]* for real normal modes of the structure, or is assumed to be lumped for coupled modes. In either case, the models used to describe damping are approximate and do not represent the exact damping mechanisms occurring in most space-like structures. Obtaining analytical models for damping mechanisms, and means to identify damping in actual structures are difficult problems which are currently being investigated by a number of researchers [7].

Modelling the dynamic behavior of the joints is also a difficult and uncertain process. Separating joint nonlinearities from the otherwise linear behavior of the structure may be a viable way to represent the linear behavior of the joints from ground tests, and then add the nonlinear contributions for on-orbit response prediction.

Another critical issue is the definition of the minimum number of dof's required in the final model for accurate on-orbit prediction *(Step 2)*. Within STARS-ID the model complexity and accuracy is progressively built-up through multiple testing and parameter updating sequences. Constructing the initial FEM model is a crucial first step to designing an accurate predictive model. The initial model must represent as closely as possible the structure that will be updated after each test. If the errors between the initial numerical model and the experimental response are too large, then the parameter updating might diverge and be unsuccessful.

However, it must also be understood that the accuracy of the prediction can be greatly improved if from the very beginning the actual structure is designed with parts that can be easily modelled, and is built to behave in a linear and consistent manner. This includes the suspension mechanisms which should not couple or interfere with the dynamics of the tested structure.

3.2. Testing Methodologies with Application to the MPI Modal Tests

The purpose of a dynamic test *(Step 3)* is to observe the dynamic behavior of structures through measured time histories or frequency response functions (FRF's), with the aim of identifying modes (*Step 4)* or directly updating model parameters (*Step 5*). The reliability and accuracy of the identified parameters are strongly dependent on the procedures used to conduct the dynamic tests. Many techniques now exist for modal testing and data reduction, and most of these methods work well on simple structures. The current procedures used to perform a good modal test are fairly standard, as described in detail in [7]. Some of these methodologies have been implemented for the MPI modal tests.

Following the STARS-ID approach, an initial model of the MPI was designed using 80 nodes (1 per node ball) and 250 rod elements (1 per strut). The struts were assumed to be interconnected at the node balls through a pinned connection. Although the initial model is crude, and could not properly represent the bending of the struts and the joint stiffness, it later proved to be adequate in predicting the lower modes of the system (Table 1). Improvement in the higher mode predictability was obtained by performing separate component tests on several strut-joint assemblies [12]. Using parameter identification methods, these sub-component modal tests provided the nominal stiffness parameters associated with bending and axial deformations of the struts and joint flexibilities.

Based on the predicted analytical mode shapes, FRF's and mode indicator functions, two shaker locations were chosen at the ends of the booms. The directions of the input forces were diagonal to the end-faces of the booms and oriented to produce the best response, including torsion, in the predicted modes up to 100 Hz. Two portable fifty-pound shakers were used for excitation at levels of approximately *1lbf.*

Two independent modal tests were performed on the MPI [14]. In the first series of test, the MPI was fully instrumented at the full 240 dof's by installing tri-axial accelerometers at each of the 80 node balls of the structure, and 40 other accelerometers were situated at a variety of strategic locations, such as mid-strut locations for longer members and suspension system attachment points. The main purpose of these tests was to achieve the detailed mode shape information required for the test/analysis reconciliation task. These tests measured the dynamic behavior of the MPI up to 100 Hz, using random input excitation at a resolution of 0.25 *Hz.*

In a second series of test, the MPI was instrumented at only 117 dof's, the location of which was optimally determined by approximating each node as a single degree of freedom oscillator, and by considering the ratio of the diagonal terms M_{ii} / K_{ii} as the equivalent eigenfrequencies. The dof's associated with the highest frequencies are removed from the analytical model using Guyan reduction. If the cross-orthogonality error between the reduced mass matrix and the full eigenvectors at the reduced dofs is less than 10%, then it is assumed that the sensors can adequately measure the target modes. This method has proved to be satisfactory for structures such as trusses which have sparse matrix representation. Eleven additional accelerometers were placed at the mid-spans of the six longest struts to measure the local behavior of these elements. The emphasis of this second series of experiments was to determine the effect of the excitation methodology on the accuracy of the identified modes. Step-sine and random excitation tests were performed at frequency resolutions of 0.093 Hz, 0.041 Hz, and 0.014 Hz, and sine-dwell tests were performed around target modes.

Mode	EXPERIMENTAL MEASUREMENTS			ANALYTICAL PREDICTION and UPDATING		
	Test Set #1	Test Set #2	Mode Type	Pre-Test Model	Updated Model	MAC Test #1
1	7.75	7.77	system	7.67	7.86	0.998
2	11.65	11.64	system	11.43	11.68	0.997
3	12.67	12.71	system	12.57	12.77	0.997
4	29.4	29.6	system	27.4	29.3	0.998
5	34.1	34.2	system	32.9	34.2	0.999
6	37.3	37.5	system	34.5	37.4	0.995
7	42.3	42.6	system	38.7	42.4	0.996
8	46.0	46.1	system	44.7	46.1	0.996
9	48.1	48.0	suspension	-	-	-
10	49.5	49.7	system	47.1	49.4	0.989
11	50.6	51.0	syst / local	49.9	51.1	0.963
12	51.7	52.1	syst / local			0.770
13	53.0	52.5/53.2	system	53.3	53.8	0.968
14	54.0	53.9	syst / susp			0.912
15	56.8	56.9	suspension	-	-	-
16	58.1	58.1	system	58..6	56.9	0.963
17	60.0	60.0	syst /susp	62.0	60.3	0.984

Table 1. Modal frequencies (*Hz*) identified from two independent tests, with comparison to the pre-test and updated analytical model predictions.

Tests were also performed for 13 different structural configurations to validate the identified model and to provide additional experimental data for the STARS-ID methodology. Multiple structural configuration are recommended to verify the predictability of the analytical model, and will be used to improve its accuracy. For the MPI modal tests, the various configurations consisted of the addition of masses equal to one-third of the boom weights at the boom tips, the inclusion of one or two extra diagonal struts within the flexible tower, and combinations of both added mass and struts at several locations on the MPI. To determine the coupling effect of the local modes, a 240*gm* mass was added in the middle of the longest strut weighing approximately 900*gm*. The test results for the primary configuration are explained in detail in [14], and are briefly summarized hereafter.

Structures can only be accurately represented by modal models if they behave as linear systems. Linearity of the MPI was confirmed in both series of tests by matching the reciprocity FRF measurements between the two shaker locations. Excellent agreement between the overlaid reciprocity FRF's also proved that the dynamic coupling of the attached shakers did not affect the modal response of the MPI. As a further evaluation of the linearity of the structure, the MPI was excited with a transient input, and then allowed to free-decay from a level of $0.2g$ to $0.02g$. Modal frequencies were evaluated for overlapping segments of the time histories, and were shown to be independent of the amplitude of vibration for the levels tested.

The actual MPI modal tests were then performed. Uncorrelated burst random inputs at the two shaker locations were used as inputs. In a first test, FRF's were averaged from 12 short bursts of approximately 0.7*sec* with 3.3*sec* decay at a resolution of 0.25*Hz*. In a second test, the FRF's were averaged from 25 longer bursts of 6*sec* with 8*sec* decay at a resolution of 0.093*Hz*. Comparison of the FRF's demonstrated that the leakage and noise level was significantly reduced in the second test because of the longer burst and decay times and greater number of averages.

The modal parameters were then extracted from the measured FRF's using a combination of Polyreference and a frequency-based mode shape algorithm [13]. In this phase of the study, only modes below 60*Hz* were considered because of high modal density beyond that value. The modal frequencies from the two sets test are compared in Table 1, with notations describing the particulars of the modes. Damping will be discussed later. For the first twelve modes up to 52*Hz*, the measured frequencies are remarkably consistent, considering that different people, hardware, and data acquisition systems and parameters were used on these two tests. The average difference is only 0.4 percent. Beyond 52*Hz*, differences in the identified frequencies could be the result of heavier hardware and cruder frequency resolution used for the first test set. The mode shapes

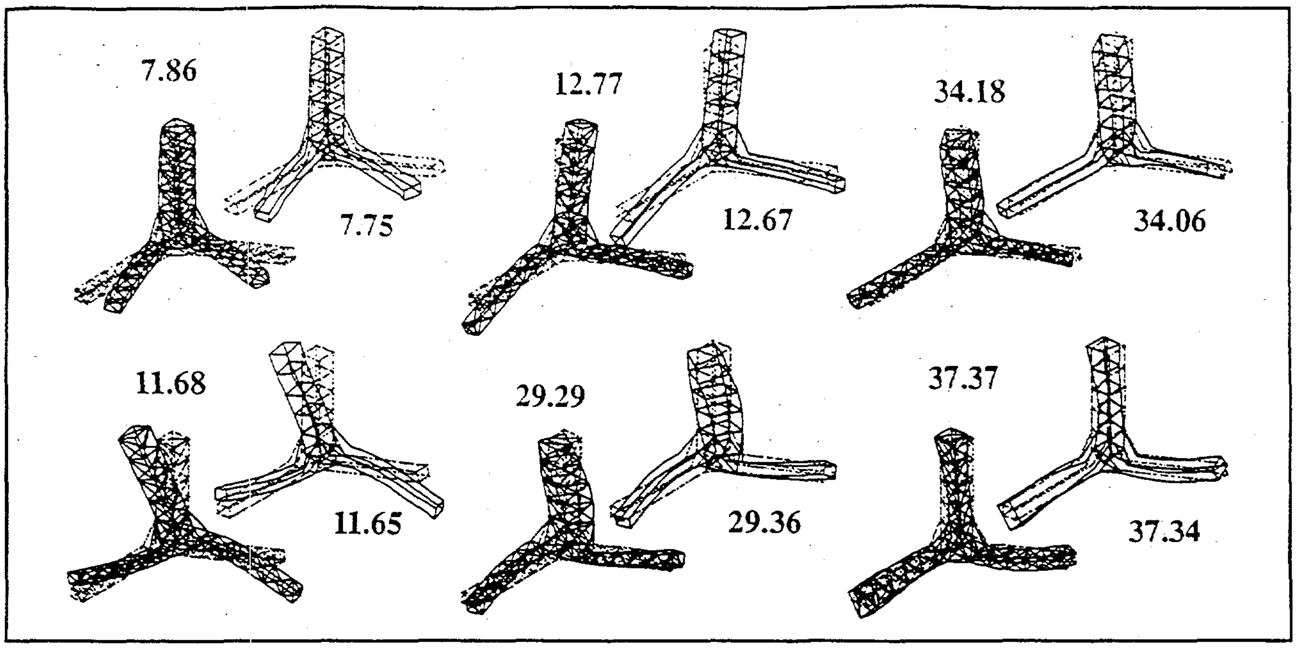

Figure 3. Experimental (top) and Analytical (bottom) Mode Shapes for the First 6 Modes.

obtained from the first test with measurements at 280 dof's are shown in Figure 3 for the first 6 modes. The first 3 modes have various scissoring motions involving different booms and the tower, while subsequent mode-shapes become more complex in their descriptions.

The identified modal parameters are then used to synthesize analytical FRF's H_{ij} (ω) between input dof i and output dof j at frequency ω :

$$H_{ij}(\omega) = \sum_{r=1}^{N} \frac{\phi_{ir}\ \phi_{jr}}{\omega_r^2\ [1 - (\omega/\omega_r)^2 + 2j\zeta_r(\omega/\omega_r)]} \tag{2}$$

where ω_r is the identified undamped natural frequency of mode r, ξ_r is the damping ratio, and ϕ_r is the eigenvector. These are compared to the original measured data. Figure 4 shows this comparison for the FRF measured at one of the driving points, in which all the modes of the structure between $5 Hz$ and $65 Hz$ are represented. The match between the measured and synthesized FRF is quite good, which lends great confidence to the data analysis portion of the modal test.

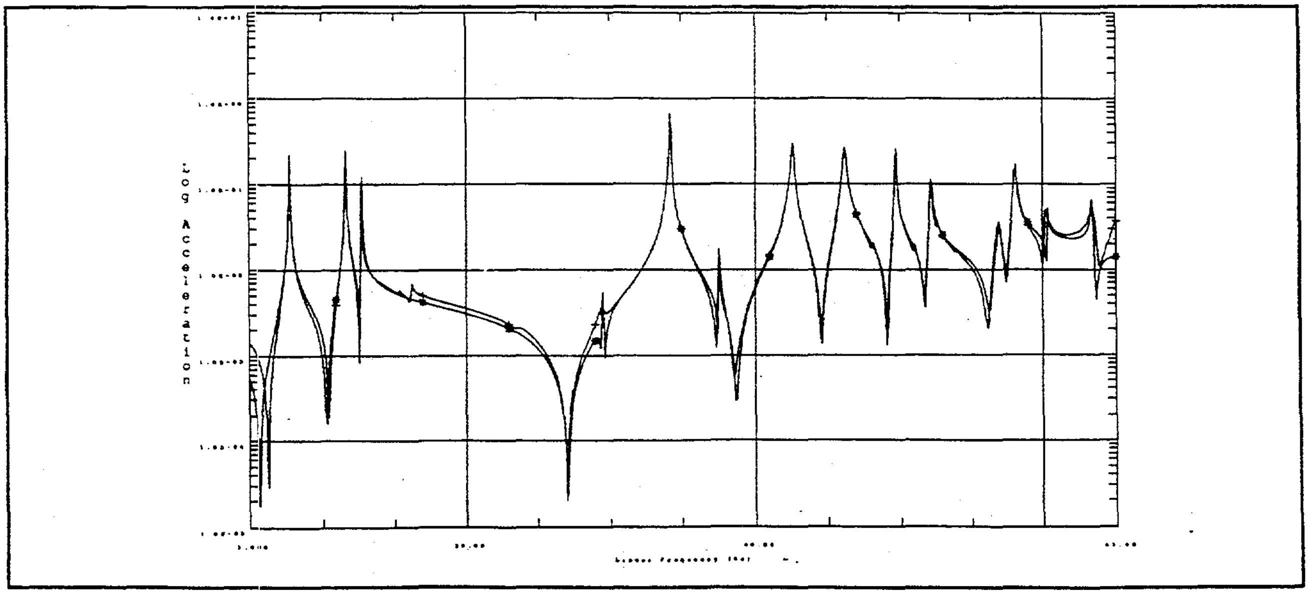

Figure 4. Comparison between the measured and analytical driving point FRF [5-65 *Hz*].

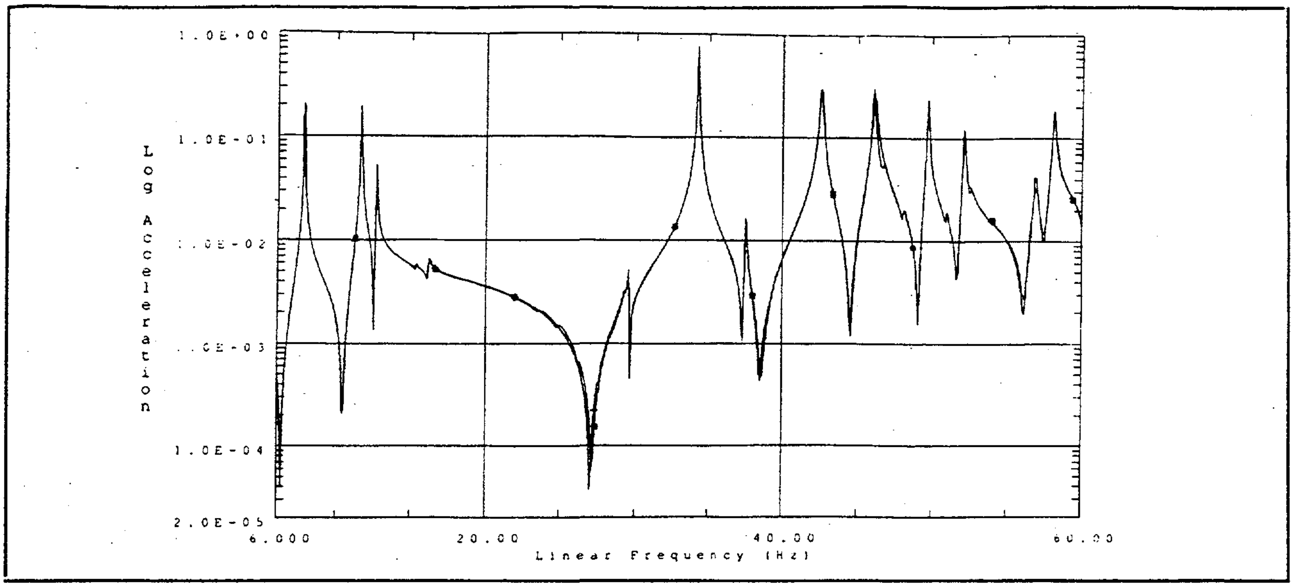

Figure 5. Comparison between the measured driving point FRF obtained with step-sine and burst random excitations for [6-60*Hz*] at ΔF=0.093*Hz*.

In an effort to qualify the experimental technique which used the burst random excitation, the FRF's were also measured using step-sine excitation. In Figure 5, the driving point FRF's have been overlaid between 6 and 60*Hz*. Both tests were performed with a resolution of 0.093*Hz*, and the burst random test used 25 averages with 6*sec* bursts and 8*sec* decays. They virtually overlay each other, although the peaks and the valleys are a little sharper with the step-sine. The data acquisition time for the step-sine was approximately 12 times longer than the burst random. Consequently, for this type of structure, accuracy comparable to the step-sine technique can be achieved much faster with burst random methods if long enough burst and decay times and sufficient number averages are performed.

To further evaluate the FRF measurement procedure, a driving point FRF was again measured with burst random excitation, but in this case the frequency resolution was varied. Figure 6 shows overlaid FRF's plotted for 0.093*Hz*, 0.041*Hz*, and 0.014*Hz*. Upon close examination one can see that the peaks and the valleys have been missed with the coarser

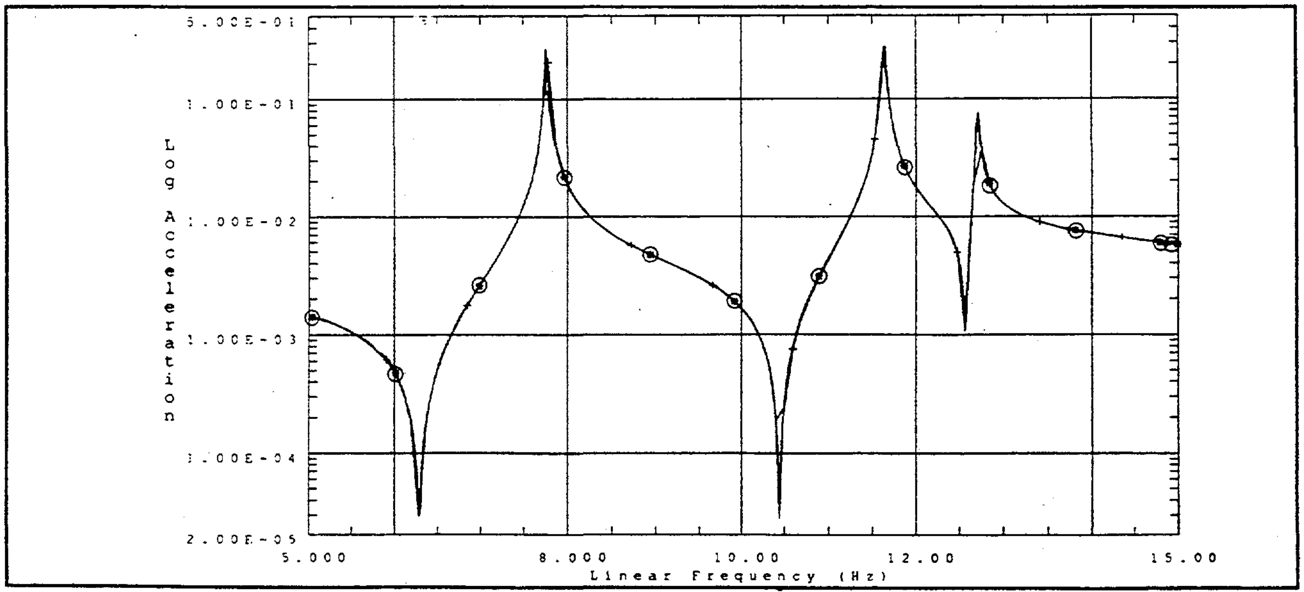

Figure 6. Comparison of the measured driving point FRF's for burst random excitation as a function of frequency resolution (ΔF=0.093, 0.041, 0.014 *Hz*).

MODE #	ΔF = 0.093 Hz		ΔF = 0.041 Hz		ΔF = 0.014 Hz	
	Freq (Hz)	Damp (%)	Freq (Hz)	Damp (%)	Freq (Hz)	Damp (%)
1	7.768	0.17	7.766	0.16	7.765	0.19
2	11.641	0.13	11.640	0.16	11.640	0.14
3	12.706	0.10	12.707	0.13	12.703	0.13

Table 2. **Effect of experimental frequency resolution on the identification of the modal parameters**

resolution test. However, identification of the modal parameters with the three sets of FRF's does not show any trends in the frequencies and damping as a function of measurement resolution (Table 2). In fact, the identified frequencies are incredibly consistent, with the damping varying just slightly more. This indicates that leakage does not affect the identification from the coarser data in this particular case. Further investigation will be carried out to analyze the differences in the mode shapes as a function of frequency resolution.

A separate series of tests also investigated the effect of the suspension system on the overall dynamics of the system. To simulate free-free boundary conditions, the MPI was suspended from three points with assemblies consisting of steel coil springs and light weight steel cables. The suspension was designed to induce "rigid body" modes of 0.7*Hz* or less to avoid coupling with the lowest MPI elastic mode expected at 7.8*Hz*. In the original configuration, the springs were lightly damped by friction induced by a steel safety wire. Later, the safety wires were removed and the two-shaker burst random tests were reiterated on the MPI with the undamped suspension system. Finally, the spring coils were fully wrapped with lightweight foam padding thus significantly increasing the friction, and the tests were reiterated on the MPI with the damped suspension system. Figure 7 overlays a driving point FRF for identical burst random tests performed with and without suspension damping. The 2 measurements are quite different, and the undamped tests are characterized by extra sharp peaks induced by spring surge. A pre-test analysis predicted surge modes at 7.86*Hz*, and 9.66*Hz*, with higher harmonics at multiples of these frequencies. Sine dwell tests performed around some of the predicted surge frequencies confirmed through visual inspection of the springs that the observed extra peaks in the undamped tests resulted from surge. In particular, the surge mode at 7.86*Hz* is strongly coupled to the first elastic mode of the MPI measured at 7.77*Hz*. Furthermore, the modes identified in the original configuration at 48.0*Hz* and 56.9*Hz* (Table 1) completely disappeared once the suspension was heavily damped.

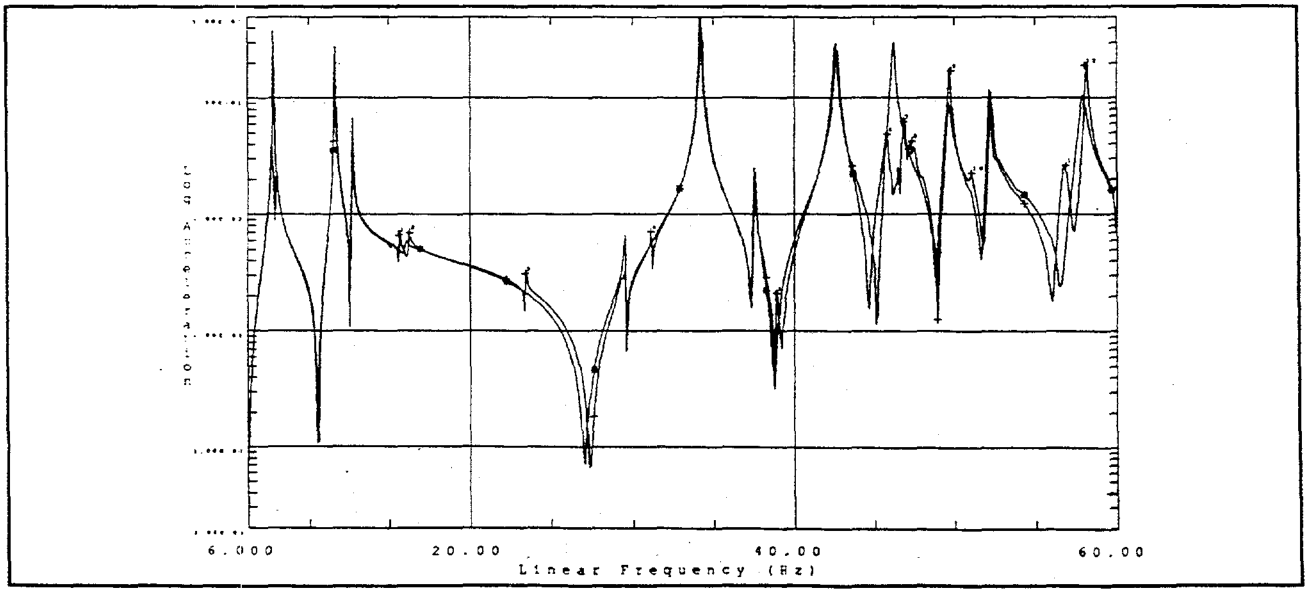

Figure 7. **Comparison of the measured driving point FRF with and without suspension damping.**

MODE #	Original Suspension		Damped Suspension		Undamped Suspension	
	Freq (Hz)	ξ (%)	Freq (Hz)	ξ (%)	Freq (Hz)	ξ (%)
1	7.77	0.17	7.78	0.14	7.75	0.49
2	11.64	0.13	11.66	0.30	11.64	0.12
3	12.71	0.11	12.75	0.14	12.71	0.10
4	29.55	0.15	29.53	0.10	29.56	0.17
5	34.22	0.09	34.26	0.11	34.21	0.08
6	37.51	0.12	37.55	0.13	37.49	0.10
7	42.56	0.21	42.62	0.23	42.53	0.20
8	46.12	0.24	46.20	0.19	46.68	0.24
9	49.69	0.09	49.57	0.30	49.68	0.13
10	50.97	0.12	51.00	0.23	51.00	0.17
11	52.15	0.13	52.23	0.12	52.13	0.12
12	52.52	0.30	52.62	0.37	52.49	0.30
13	53.21	0.17	53.17	0.30	53.14	0.16
14	53.92	0.24	53.83	0.50	53.81	0.38
16	58.08	0.15	57.85	0.32	58.11	0.66

Table 3. **Identified modal frequencies and damping as a function of suspension damping**

To understand how the suspension mode couple with the structure, the modal properties of the MPI were identified for all three damping configurations. The results are listed in Table 3 for all the structural modes up to 58*Hz*. It can be seen that the identified modal frequencies are consistent regardless of the suspension configuration. However, in the undamped case, those system modes that are coupled to the surge, such as the modes at 7.75*Hz* and 46.14*Hz*, also have high damping values of the order of 0.3% to 0.5%. In all other cases, the damping identified for the structure is of the order of 0.1% to 0.2%.

In conjunction with the STARS-ID process, future work will investigate the kind of input functions which would be most appropriate for accurate modal extraction and/or structural parameter identification. This leads to the notion of an optimal excitation pattern design, for which the optimization criteria may be the identifiability of specific modes (weighted or not for their importance) or of specific structural parameters (which can also be weighted for there importance). The "optimal input design" also entails an "optimal actuator location and direction". Work in this area is reported in more detail in [7].

Just as the actuator location and excitation pattern are related to the controllability of the parameters, optimal sensor location are related to observability. In many respects, the problem of sensor location is also closely related to that of dof reduction methods for FEM models. Like the actuator location problem, location of the sensors must be selected on the basis of an optimality criterion which matches the purpose of the test. Other methods than the ones used for the MPI modal tests have been reported in [7].

3.3. Test/Model Correlation

The next step in the STARS-ID process is to compare the test results to the analytical prediction (*Step 5*). The accuracy of the predictive model is strongly dependent on the procedures used for model verification and error localization, on the parameter identification/updating process, and on the ability to extract the model parameters from the experimental data. The selection of appropriate prediction measures, as well as model/test correlation indicators are discussed in [7]. The first task is to determine which modes should be paired for comparison and correlation. The second task is to assess the "closeness" of the identified mode pairs by quantifying the discrepancies. The traditional metric for mode agreement is the modal assurance criterion (MAC). It is a convenient metric since it does not require mass normalization of the modes and it reduces the mode pair agreement to a single scalar value. The MAC is a measure of the linear dependence between the analytical and experimental eigenvectors, Φ_a and Φ_e, respectively:

$$MAC \equiv \frac{\Phi_a^T \Phi_e}{|\Phi_a| \, |\Phi_e|} \qquad (3)$$

where T denotes the transpose, and $| \, . \, |$ is the Euclidean norm. Other advanced metrics and model correlation techniques which provide additional insight into mode correspondence and characterize mode shape pairs are reported in [7] and [15].

3.4. Parameter Updating and Model Refinement

The parameters must then be updated to match the experimental results. In STARS-ID the predictive accuracy is achieved by updating the model from independent sets of data and for various structural configurations. Among the many existing parameter updating schemes, special attention is given to those most suited for multiple test configurations and statistical reliability estimation [7].

Following the classification of Roy *et al.* [16], FEM updating techniques from measured modal information fall into 2 categories: *global and local.* Global methods directly modify the coefficients of the mass and/or stiffness matrix of the FEM model. Local methods perform corrections of the physical parameters, such as element geometric properties, E and ν. The proposed analytical model must correctly represent the dynamic behavior of the structure, and only the value of the parameters is altered to fit the experimental results. Among the types of local methods, those based on sensitivities are the most appropriate for implementation in STARS-ID.

Sensitivity methods linearize the relations between the modal parameters and the physical parameters to be modified, followed by a least squares minimization. Research in this area has been performed by J. Collins and T. Hasselman, G. Lallement, J. Piranda, R. Fillod, R. Glaser, E. Dascotte, B. Caesar, M.L. Wei, T. Janter, and N. Creamer [7]. Adjustments to the physical parameters are performed by minimizing the error between the analytical and the measured modal response of the structure through the sensitivity derivatives. The update is accomplished iteratively or optimally, depending on the number of physical parameters and on the number of measurements available.

Collins *et al* [10], and later Hasselman [11] developed a Bayesian parameter estimation technique which is formulated in an iterative process and uses the measured natural frequencies and mode shapes to modify the physical stiffness and mass properties of the analytical model. The merits of this method are that all operations are performed with the *full* FEM model. However, this results in computational requirements which may be very high and updating should not require more than a limited number of iterations. Thus, it is important that the initial estimates of the analytical model be very close to the actual properties, and that the analytical model itself allow a true representation of the dynamic behavior of the structure. This method preserves the connectivity of the original analytical model during the iteration. It is implemented in the computer code SSID which updates the model parameters from eigenproperties using an efficient Lanczos eigensolver. It is conveniently set up for recursive algorithms and statistical evaluation of the results, and it makes provisions for future parameter updating capabilities from measured FRF or input/output time histories for STARS-ID.

The current application uses modal information only. It assumes that the differences between the experimental and analytical frequencies and mode shapes are small, and result from both model errors and experimental errors, ϵ. The errors between the eigenproperties of the measured data $u_t = < \lambda_t , \phi_t >^T$ and the model eigenproperties $u_m = < \lambda_m , \phi_m >^T$ can be approximated by a first order Taylor expansion about the current analytical values r_i of the design parameters r $(\rho, E, I, \ldots)$ obtained after the i^{th} iteration:

$$\begin{Bmatrix}\lambda_t\\ \Phi_t\end{Bmatrix} = \begin{Bmatrix}\lambda_m\\ \Phi_m\end{Bmatrix}_{r = r_i} + T\left\{r - r_i\right\} + \epsilon \tag{4}$$

where T is the sensitivity matrix at the current parameter values $r=r_i$:

$$T = \left[\frac{\partial}{\partial r}\begin{Bmatrix}\lambda_m\\ \Phi_m\end{Bmatrix}\right]_{r = r_i} = \begin{bmatrix}\dfrac{\partial \lambda_m}{\partial K} & \dfrac{\partial \lambda_m}{\partial M}\\ \dfrac{\partial \Phi_m}{\partial K} & \dfrac{\partial \Phi_m}{\partial M}\end{bmatrix}_{r = r_i} \cdot \begin{bmatrix}\dfrac{\partial K}{\partial r}\\ \dfrac{\partial M}{\partial r}\end{bmatrix}_{r = r_i} \tag{5}$$

The weighted errors in the measurement and and in the physical parameter are minimized using the Bayesian estimator :

$$J = (u_t - u_m)^T S_{\epsilon\epsilon} (u_t - u_m) + (r_0 - r)^T S_{rr} (r_0 - r) \tag{6}$$

where the weighting coefficients S_{rr} and S_{ee} are the cross-correlation matrix of the physical parameters and the eigenproperties, respectively. In the general case where there is more data than parameters, it can be shown that the set of physical parameters r can be estimated recursively from:

$$r_{i+1} = r_i + \left[S_{rr}^{-1} + T^T S_{\epsilon\epsilon}^{-1} T\right]^{-1} \left[S_{rr}^{-1}(r_0 - r_i) + T^T S_{\epsilon\epsilon}^{-1}(u_t - u_i)\right] \tag{7}$$

Convergence is reached when r_{i+1} equals r_i to within a pre-specified accuracy. The posterior covariance matrix describing the statistical reliability of the most probable parameter estimates r^* is then obtained from Equation 5:

$$S_{rr}^{*} = \left[S_{rr}^{-1} + T^T S_{\epsilon\epsilon}^{-1} T\right]^{-1} \tag{8}$$

Because the covariance matrix of both the *prior and posterior* estimates are computed, SSID could be efficiently modified to perform model updating from multiple tests in which the posterior covariance matrix from *Test i* is used as a more accurate weighting function for *Test i+1*. Furthermore, the posterior covariance matrices could also be used to determine the accuracy of the updated parameters and reliability of the assumed FEM model to fit the measured data. This new approach is currently under implementation within STARS-ID.

The above model updating technique applied to the sub-component tests defined the joint-strut assemblies in terms of 5 elements, the parameters of which were incorporated into the full system model. For the MPI testbed, the pre-test rod model with 240 dof's was refined to a beam model with approximately 10,000 dof's. The model updating technique was then applied to the full model to match the measured modal properties and mode shape of the test set #1. Table 1 shows that the measured modal frequencies are very close to those of the updated analytical model, with differences of the order of 1%. The rows corresponding to the spring surge were left blank, since the analytical model did not represent the suspension mechanism. The analytical mode shapes also closely match the experimental measurement as illustated in Figure 3, and as demonstated by the

MODE	24 kgs @ Met. Boom		16 kgs @ Opt. Boom		Added Strut in Tower	
	Test	Model	Test	Model	Test	Model
1	6.45	6.45	7.03	6.87	8.16	8.04
2	9.7	9.5	10.8	10.5	11.6	11.5
3	12.6	12.3	11.8	11.6	12.7	12.5

Table 4 Comparison of the analytical prediction to the measured experimental modes for various structural configurations.

MAC values listed in Table 1. The model updating results for the MPI are described in more detail in [12,15]. Discrepancies that still remain require further refinement of the analytical model. This will be resolved by performing full system parameter estimation on the physical elements that were not identified in the component level tests and by including the suspension in the full system model.

Table 1 aslo demontrates that the pre-test rod model with only 240 dof's predicted the actual modes of the MPI fairly well, and contributed to the success of the updated model. The robustness of the pre-test model was further verified by comparing its prediction for known perturbations in the MPI. Modes identified from actual test performed with added mass at the tips of the booms and extra diagonal struts in the towers are compared to the analytical predictions of the first three modes in Table 4. It is shown that the predictive accuracy of the model is excellent. Using the recursive form of the proposed Bayesian estimation technique to match the modal information from the multiple configuration tests will further improve the reliability of the model.

4. Conclusion

A systems approach, STARS-ID, was presented in which accurate FEM models of flight systems obtained from ground-based tests could be used for on-orbit performance prediction. STARS-ID methodologies were successfully tested on the MPI truss structure at JPL.The physical parameters are updated from multiple ground-based experiments involving deterministic changes in the structural configuration. For this purpose, model correlation methods based on local sensitivity techniques are recommended for sequential or simultaneous implementation of the multiple configuration tests. Within this classification, methods based on Bayesian estimation techniques are recommended for statistical inference. For future flight missions, statistical methods within STARS-ID will become necessary to determine the most probable set of physical parameters based on the experimental data, and will be required to assess whether the reliability bounds of the predicted performance fall within the requirements.

The accuracy and reliability of the structural parameter estimates are strongly related to the experimental procedures and the modal identification techniques. STARS-ID advocates experimental techniques which are capable of isolating structural modes from suspension effects, identifying local modes and separating closely-spaced modes. It was demonstrated how methods such as stepped-sine testing about particular modes, and sub-component or element testing could contribute significantly to the increase in accuracy of the updated structural model. In the future, considerations such as optimal sensor/actuator location, and excitation force design targeted at specific modes or parameters must also be investigated to enhance the reliability of the analytical models.

Acknowledgements

The work and support of Tom Carne and Randy Mayes at Sandia, and of Lee Sword and Greg Neat at JPL are greatly appreciated.

References

1. Hanks, B.R., "Dynamic Challenges for the 21st-Century Spacecraft", Proc. 61st Shock and Vibration Symposium, Vol. 4, pp. 3-18. Pasadena Ca., Oct. 16-18 1990.
2. Milman, M., C. Chu, and M. Salama, "Integrated Control-Structure Design of the JPL Phase-B Testbed", 5th NASA/DOD CSI Technology Conference, Lake Tahoe, Nevada, March 5, 1992.
3. Denman, E.E., T.K. Hasselman, *et al.*, "Identification of Large Space Structures on Orbit - a Survey",USAF/ NASA Workshop on Model Determination for Large Space Structures. JPL/Caltech, Pasadena Ca., March 22-24, 1988. pp.36-53.
4. Juang, J.N., and R.S. Pappa, "A Comparative Overview of Modal Testing and System Identification for Control of Structures", 1990.
5. Huang, H.H., and R. R. Craig, Jr., "A Review of Error Localization and Model Updating for Structural Components", Report No. CAR-91-1, Center for Aeronautical Research, Univ. of Texas at Austin, May 1991.
6. Lallement, G., and J. Piranda, "Methodes de Recalage de Modeles en Elastodynamique Lineaire", Course notes for COMETT, Durbuy, Belgium, Oct. 7-11, 1991.
7. Levine-West, M.B., "High Fidelity Predictive Models of Structures on Orbit", Report No. JPL D-10113, Jet Propulsion Laboratory, California Institute of Technology, Pasadena, California, Sept. 1992.
8. Laskin, R.A., and M.S. Martin, "Control/Structure System Design of a Spaceborne Optical Interferometer", Proceedings of the AAS/AIAA Astrodynamics Specialist Conf., 1989.
9. Isenberg, J., "Progressing from Least Squares to Bayesian Estimation", Proc. ASME Dynamic Systems & Control Division, Paper No. 79-WA/DSC-16, New York, N.Y., Dec. 2-7 1979.
10. Collins, J.D., G.C., Hart, T.K. Hasselman, and B. Kennedy, "Statistical Identification of Structures", AIAA Journ., Feb. 1974, pp.185-190
11. Hasselman, T.K., J.D. Chrostowski, and T.J. Ross, "SSID/PDAC Theoretical Manual (Version 1.0)", Technical Report No. TR-91-1152-1, prepared for the National Aeronautics and Space Administration by Engineering Mechanics Associates, December 1991.
12. J.R. Red-Horse *et al.*, "System Identification of the JPL Micro-Precision Interferometer Truss: an Overview", Proc. of the 3rd Int'l Conf. on Adaptive Structures, San Diego California, Nov. 1992.
13. R.L. Mayes. "A Multi Degree of Freedom Mode Shape Estimation Using Quadrature Response", Proc. of the 11th Intern'l Modal Analysis Conf., Kissimmee Fl., Feb. 1993.
14. T.G. Carne, R.L. Mayes and M.B. Levine-West, "A Modal Test of a Space-Truss for Structural Parameter Identification", Proc. of the 11th Intern'l Modal Analysis Conf., Kissimmee, Fl., Feb. 1993.
15. J.R. Red-Horse, E.L. Marek, and M.B. Levine, "System Identification of the JPL Micro-Precision Interferometer Truss: Test-Analysis Model Reconciliation", Proc. of the 34th AIAA SDM Conference, La Jolla, Ca., March 1993.
16. Roy, N. A., A. Girard, L. P. Bugeat, and J. N. Bricout, "A Survey of Finite Element Updating Methods", Proc. of the International Symposium on Environmental Testing for Space Programs - Test Facilities and Methods, ESTEC, Noordwwijk, The Netherlands, June 26-29, 1990.

Submitted to the 3rd International Conference on
Adaptive Structures
San Diego, CA, November 9–11, 1992

System Identification of the JPL Micro-Precision Interferometer Truss: An Overview

J. R. Red-Horse[1], T. G. Carne, E. L. Marek, R. L. Mayes
Sandia National Laboratories, Albuquerque, NM

G. W. Neat and L. F. Sword
Jet Propulsion Laboratory, Pasadena, CA

Abstract

The JPL Micro-Precision Interferometer (MPI) is a testbed for studying the use of control-structure interaction technology in the design of space-based interferometers. A layered control architecture will be employed to regulate the interferometer optical system to tolerances in the nanometer range. An important aspect of designing and implementing the control schemes for such a system is the need for high fidelity, test-verified analytical structural models. This paper summarizes coordinated test and analysis efforts aimed at producing such a model for the MPI structure. Pretest analysis, modal testing and test-analysis reconciliation results are summarized for a series of tests at both the component and full system levels.

Overview

The Jet Propulsion Laboratory (JPL) Control Structure Interaction (CSI) Program is responsible for the investigation of control challenges faced by future large precision optical systems in space. A search to select a specific mission on which to apply the CSI technology adopted an advanced concept known as the Focus Mission Interferometer (FMI). The FMI is a large, spacecraft-based, partial aperture telescope capable of both imaging and astrometry (resolving and measuring the angle between two objects, respectively). This advanced concept was the object of a preliminary analytical study tasked with determining the CSI technologies that would be required to meet the mission's science requirements [1]. In this analytical study, a truss structure spanning 30 meters supported both spacecraft and instrument hardware. Proper instrument operation required controlling and measuring the positions of optical components distributed throughout the structure to the nanometer level. To achieve these requirements, a control architecture evolved which collectively provided the necessary vibration attenuation capabilities. Subsequent efforts have been directed at verifying this control scheme in hardware.

The Micro-Precision Interferometer (MPI) Testbed is a ground-based, half-scale hardware version of the FMI (see Fig 1) comprised of two booms and a vertical tower with dimensions of 7m x 6.3m x 5.5m. The primary objective of the testbed is to confirm the viability of a space-based interferometer concept by incorporating CSI technology.

---

[1] John Red-Horse, Dept 1434, Sandia National Laboratories, P.O. Box 5800, Albuquerque, NM 87185

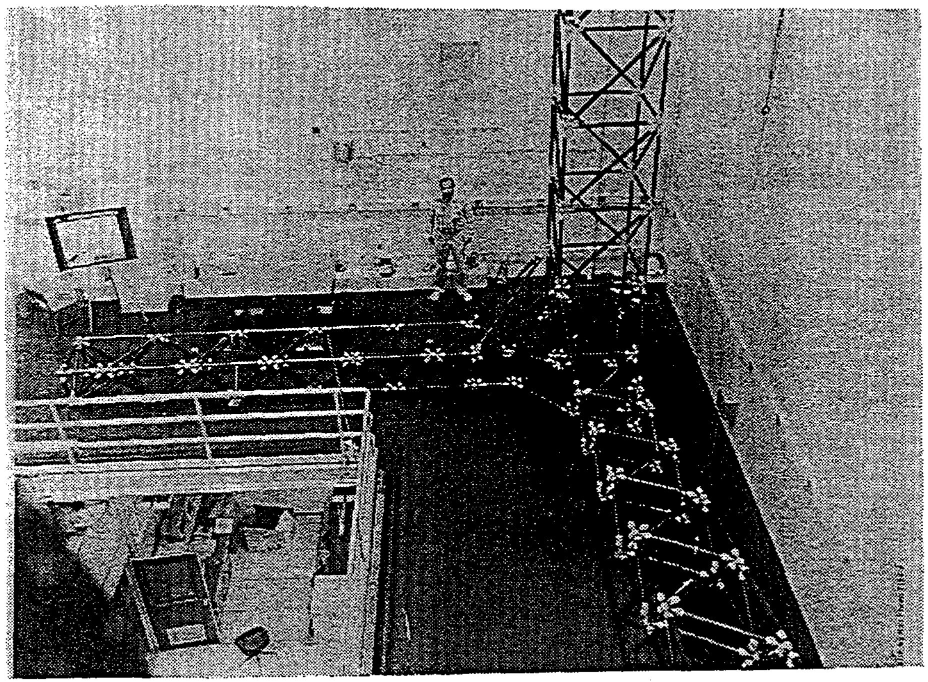

Figure 1: Photograph of MPI Structure

The testbed will evolve in distinct phases over a number of years. A major structural configuration change marks each phase. Each of these changes involves a sequence of events, which includes design, fabrication, assembly, and integration of new components followed by characterization of the resulting structure and appropriate analytical model updates. The plan for repeating this sequence a number of times provides an ideal opportunity to perfect testbed design, characterization, and modeling approaches. The testbed to date is a bare truss structure, suspended by three linear extensional springs. Late in 1992, the first set of optical components will be mounted to the structure marking the beginning of a two year intensive control experimentation effort. In 1996, a second round of optical components will be designed and mounted to the structure. This latter component set will provide the testbed with all the elements necessary to demonstrate complete instrument functionality.

In its simplest form, the space-based interferometer articulates or translates optical elements so that a partial aperture telescope emulates a traditional full aperture system. Instrument performance improves with increase in diameter of the full aperture, or analogously, distance between the partial apertures. The advantage of the partial aperture system is that it achieves comparable performance to the full aperture system though at a significant reduction in the required structural mass. However, to satisfy the instrument's performance requirements, the optical component translations and articulations must be precisely regulated in the presence of an induced vibratory environment.

The MPI Testbed provides a means of experimentally verifying system level effects between different vibration attenuation methods. These methods together form the layered control architecture involving vibration isolation, structural control and optical control techniques [2]. A six axis isolation system will attenuate typical spacecraft disturbances such as tape recorders, reaction wheels, and articulating solar panels. The interface between the testbed disturbance sources and the structure allows for the incorporation of different isolator designs including hard and soft mount approaches and active and/or passive isolator designs [3]. The structural control methods provide a means of vibration attenuation in targeted frequency ranges that will enhance the performance of the optical control systems. This is done by replacing various truss elements with active or passive damping elements. The testbed's optical system is a Michelson Interferometer, the components of which will be distributed across 7 meters of structure. The optical design will evolve from a ground-based operational interferometer (Mark III) which is bolted to bed rock at the summit of Mt. Wilson [4]. The wave front tilt and stellar path length control subsystems are the primary optical control loops. Successful interferometer operation requires that these control systems have high disturbance rejection across a broad range of frequencies in spite of the structure's dynamics. In addition, the optical system contains a complex metrology system to sense the position of critical components.

Accurate characterization of the testbed in conjunction with successful model updating procedures should facilitate the generation of high fidelity finite element testbed models. The need for such models is particularly important when addressing control objectives in the micro-dynamic regime. The resulting models will need to provide: (1) a tool to aid in the design of future testbed configurations, and (2) a high confidence simulation environment for the design and evaluation of system and subsystem level control approaches. For example, the current mechanical design challenge is to develop mounting hardware for optical and spacecraft components and to determine the locations at which to attach this hardware to the structure. The resulting global and local dynamic behavior must not complicate the alignment of optical elements and must not limit the bandwidth of subsystem control loops. Accurate modeling is essential for successful implementation of specific control methodologies as well. Examples include the placement of active and passive elements, as well as the design of Multiple-Input/Multiple-Output structural control schemes for which the measurement of plant transfer functions is impractical.

Generating a high fidelity analytical model is implicitly dependent on the characteristics of the physical structure. The CSI Program at JPL has extensive experience in the design, fabrication and assembly of linear, lightly damped precision truss structures [5, 6]. These objectives are achieved by properly selecting structural materials, proper joint design and adopting precision assembly procedures. Drawn aluminum tubing was the material selected for the MPI Testbed struts based on its homogeneous construction and strict manufacturing tolerances which allow for accurate characterization. Even the best tubing available is not perfectly straight, therefore a bonding jig was designed to hold the end fittings collinear during the adhesive injection and curing process. Figure 2 shows how these struts are joined with the node balls using the adjustable B-Nut hardware. Precision measuring devices were developed, capable of determining node to node distances to within a tolerance of .1mm. These linear measuring devices, used in conjunction with an optics table which provided a planar reference, resulted in an assembled structure with tolerances in the submillimeter range.

The field of Structural System Identification is concerned with producing accurate analytical models. Examples of work in this area can be found in [7, 8]. In general, such models should be capable of representing the physical structure through numerous configuration changes; in this case, those encountered during the design phase in the

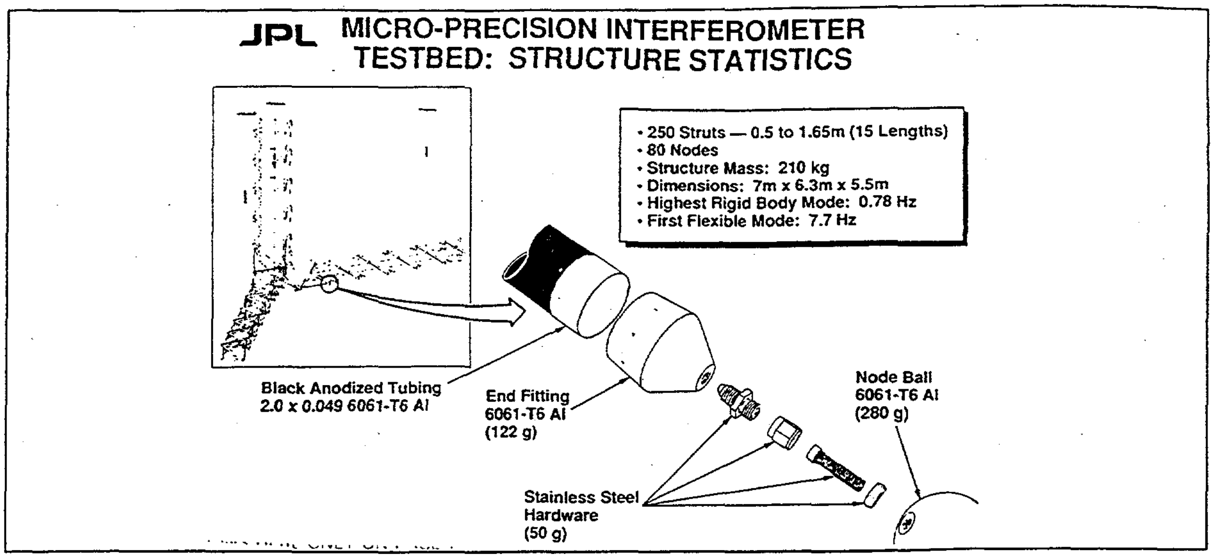

- 250 Struts — 0.5 to 1.65m (15 Lengths)
- 80 Nodes
- Structure Mass: 210 kg
- Dimensions: 7m x 6.3m x 5.5m
- Highest Rigid Body Mode: 0.78 Hz
- First Flexible Mode: 7.7 Hz

Figure 2: Detail of MPI Components

testbed and those expected in the actual operation of the telescope. This paper discusses the testing, modeling, and model updating procedures applied to the initial configuration of the MPI testbed structure for which it is a bare, suspended space frame.

The approach taken was to identify the structure by determining a suitably rich physical parameter set through a coordinated, three-pronged effort involving pre-test analysis, test, and reconciliation phases. For a variety of reasons, the identification was performed in two stages: first, a component level identification procedure was performed, then the results from this initial phase were incorporated into the identification of the full system.

Component Level Identification

Modal Tests

The bare MPI structure is constructed of a few basic components that are replicated throughout the structure. Therefore, it seemed plausible that accurate finite element models (FEM) of these components would lead to an accurate model of the assembled structure.

The component level test plan had two objectives. The first was to provide data to determine the nominal physical parameter values associated with the bending and axial stiffnesses of the struts, strut end caps, and B-Nut connectors which attached each strut to the node balls. The second was to provide data for deterministically quantifying phenomena that might cause variations in the parameter values. The phenomena that were chosen to address were: (1) Dynamic amplitude of vibration, (2) Static strut loading (e.g. from gravitational or nonuniform thermal loads), (3) B-Nut installation torque, and (4) B-Nut installation length. In this section, we concentrate on results relating to the first objective—determining the nominal stiffness parameters.

Nominal Component Parameter Characterization

Figure 3 shows the seven configurations of the node balls, struts and B-Nut assemblies that were tested. All except Configuration 4 were used to provide data to meet the first objective described above. Each configuration was suspended by soft shock cords and string so that the rigid body modes would be well separated in frequency from the first elastic mode. In each configuration a small impact hammer with a force transducer was used to impact one of the end balls longitudinally to excite the first axial mode. Each configuration was impacted laterally at the middle ball (or the middle of the strut if there was no middle ball) to excite the first bending mode. Frequencies and damping were extracted for the first elastic mode in each impact direction from frequency response functions (FRF's) of the accelerometers to the input hammer force. Five averages were taken to form each FRF estimate. Table 1 lists the results of these tests.

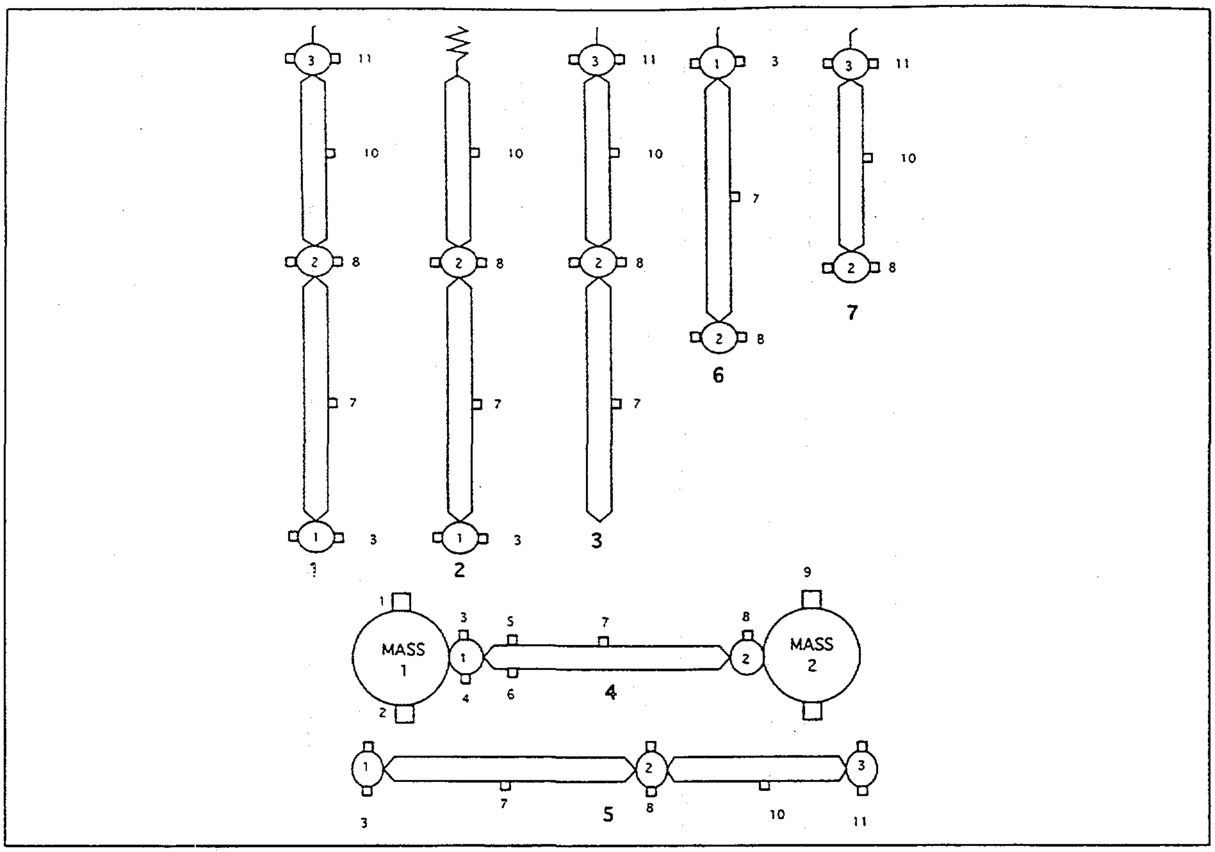

Figure 3: Seven Tested Subsystem Configurations

Linearity Checks

For six of the configurations, a linearity check was performed. The variation in frequency was mapped as the amplitude decayed freely from an impact with the hammer. Eight seconds of data were taken for the axial impacts and 16 seconds were taken for the lateral impacts. The roots were extracted from the first 25% of data, then the next 25% and so on. The structural elements appear to be linear for all practical purposes. The variations

Configuration	Bending Properties		Axial Properties	
	Freq (Hz)	Damping (%)	Freq (Hz)	Damping (%)
1	12.26	1.0	826.3	0.1
2	15.91	0.5	942.2	0.1
3	13.95	0.4	1013.2	0.1
5	12.09	0.5	825.5	0.2
6	133.56	0.6	1202.3	0.3
7	165.5	0.4	1518.5	0.1

Table 1: Nominal Modal Results for the Component Tests

in frequency for these configurations were all less than 0.2% for axial modes and 0.4% for bending modes.

Summary of Remaining Results

Configuration 4, where a short strut was placed between two large masses, was used to determine how variations in the selected phenomena affected the response natural frequencies. The results of initial tests in this configuration, directed at investigating the effects of changing B-Nut length and torque level showed that the joint between the ball and the large masses experienced an apparent change in stiffness. Significant tightening of this joint led to results that agreed well with analytical predictions. Varying the angle of the support cables in Configuration 4 provided a means to test axial static load effects. Results were plausible for the bending behavior, but proved inconclusive for the axial modes. This ball mass torque level problem, which explains the omission of Configuration 4 from Table 1, is thought to explain these inconclusive static load data.

Analytical Parameter Identification

Here the task was to identify the structural elements at the subsystem level from the results of the modal test series. This identification results in both an appropriate model form as well as estimates for the accompanying nominal parameter values.

Parameter estimation was accomplished for all subsystem configurations and parameters (i.e., those affecting both axial and bending response) using a design sensitivity based approach (DSA) as implemented in the SDRC software package, CORDS [9]. As a validation step, a subset of these parameters was also estimated using a Bayesian estimation algorithm as implemented in the program SSID [10].

Model form was addressed by estimating across multiple subsystem configurations, simultaneously in the case of CORDS, and consistently across individual configurations for SSID. The premise of this approach is that parameterizations can not support accuracy across a variety of configurations if the model form of the structural subsystem does not capture the correct qualitative structural behavior. The final model form was comprised of point masses for the node balls with rigid elements from these points to their geometrical radii and three beams: one each for the B-Nut assembly, end cap, and strut. Each beam element accounted for mass via nonstructural mass specifications which decoupled it from the physical parameters for each beam: cross sectional areas and moments of inertia.

The reconciliation procedure was separated into two phases with the axial and bending characteristics considered independently. Due to the cited problems with torque level between the large masses and node balls, the original Configuration 4 test results were not considered in the subsequently described reconciliation analyses. However, as a post study verification of model form, Configuration 4 with a long B-Nut assembly (for which the torque problem had been addressed) was considered.

Axial Characteristics

For this parameter set correlation was performed using the DSA approach with data from each of Configurations 1 through 7 (with the exception of Configuration 4) stacked in a single response vector. The results are summarized in Table 2. A consistent update was achieved with good test-analysis model agreement across the configuration set.

Config/	Axial Results			Bending Results		
Item	Initial	Final	Test Freq (Hz)	Initial	Final	Test Freq (Hz)
1	815.2	825.7	826.3	13.20	12.25	12.26
2	928.7	941.7	942.2	17.04	15.83	15.91
3	1003	1015	1013	14.99	13.92	13.95
6	1162	1181	1202	148.9	133.4	133.5
7	1470	1490	1519	198.6	167.2	165.5
A_{strut}	0.3003	0.3123	—	—	—	—
A_{bnut}	0.0700	0.0672	—	—	—	—
I_{bnut}	—	—	—	$4.0(10^{-4})$	$4.01(10^{-4})$	—
I_{endcap}	—	—	—	0.0477	0.00856	—
$I_{longbnut}$	—	—	—	$4.0(10^{-4})$	$3.77(10^{-4})$	—

Table 2: Component-Level Reconciliation Results

Bending Characteristics

The DSA approach was also taken for estimating the bending parameters. In addition, the Bayesian approach described above was implemented for which formal consideration was given to both modal frequency and shape data. A particularly striking result was that both methods produced effectively identical parameter estimates. These results are also shown in Table 2, where one can observe the good correlation for each member of the configuration set.

Configuration 4 Revisited

Configuration 4 from the original test series was not considered in the reconciliation process due to the effects of the connections between the large masses and the node balls. However, this test was repeated with longer versions of the B-Nut assembly for the purpose of gaining insight into the effects of B-Nut length on the response characteristics. An attempt was made to reconcile the test and analysis models for one particular B-Nut length (3.1in). Both methods yielded good agreement for the axial properties, but the bending characteristics proved problematic. Estimation was performed using the first three bending modes without achieving consistent results. A close examination of the third bending mode shape showed that a qualitative response property, namely rotational motion between the large end mass and the node ball, was not being captured by the initial model form. Resolving this issue and re-estimating yielded consistent results which are shown in Table 3.

Freq No/ Item	Initial FEM	Final FEM	Test (Hz)
1	6.07	6.23	6.21
2	8.76	9.02	9.04
3	112.1	114.9	115.2
$I_{longbnut}$	$4.0(10^{-4})$	$3.77(10^{-4})$	—

Table 3: Config 4 (long B-Nut) Reconciliation Results

System Level Identification

Modal Testing

In contrast to the component testing, which was designed to exercise localized behavior in simple structural elements, the system level modal test was intended to exercise the entire MPI structure with all structural elements interacting. The primary objectives of the system level test were to obtain laboratory measurements of the dynamic properties of the structure and to provide the data necessary for building an accurate analytical model.

The structure was supported by soft springs in the laboratory to simulate a free-free environment which would best mimic the operational environment of the MPI. Initial plans were to measure and identify all elastic modes below 100Hz, but the upper limit was reduced to 60Hz due to the high modal density occurring in the range above 60Hz.

Supporting the structure so that free boundary conditions were well approximated was a very important aspect of the pre-test planning. For this test the MPI was suspended from three points with assemblies consisting of steel coil springs and light weight steel cables which produced rigid body modes in a range below 1Hz.

After examining the pre-test mode shapes, FRF's, and mode indicator functions provided by the analysis model, two shaker locations were chosen at the ends of the two booms. The directions of the input forces was diagonal to the end-faces of the booms and oriented to produce torsional response. Two portable fifty-pound shakers were used for excitation. Every one of the eighty node balls of the truss structure was instrumented with a tri-axial accelerometer. Additional accelerometers were also placed at a variety of strategic locations, such as mid-strut locations for longer members and suspension system attachment points, to achieve the detailed mode shape information necessitated by the uncertain data requirements of the test/analysis model reconciliation task.

After the MPI was completely instrumented with approximately 280 accelerometers, reciprocity was measured between the two shaker attachment locations. An acceleration-to-force FRF was measured from Shaker 1 to the driving-point accelerometer at Shaker 2 with Shaker 2 disconnected from the structure, and conversely. Reciprocity requires a linear elastic structure, but by disconnecting the nonexciting shaker it can also detect shaker attachment effects. Figure 4 displays an overlay of the two reciprocity measurements.

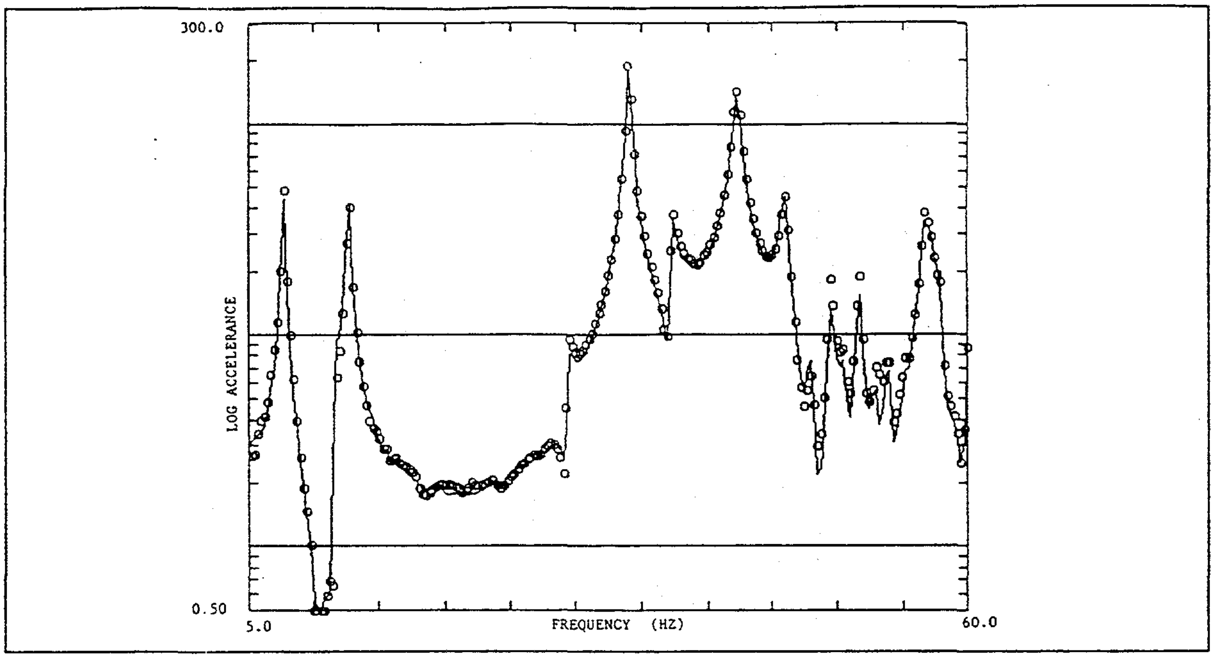

Figure 4: Shaker Reciprocity Checks

Examining the figure, one can see that the reciprocity FRF's agree quite well—evidence that the structure is linear at the excitation levels of interest and that the shakers had been attached without changing the structure.

After the linearity evaluations were performed, the actual modal test proceeded with measurement of the FRF's. Although groups of accelerometers where sequentially switched into the data acquisition system, the instrumentation remained unchanged throughout the entire modal test to ensure the structure was unchanged during the test. Burst random inputs were used as the excitation. From the total set of FRF's, an initial test-derived modal model was extracted, using a combination of Polyreference [11] and a frequency domain-based mode shape algorithm [12]. After an initial reconciliation attempt with the analytical model was made, a second data reduction was performed. The data for these models are discussed in conjunction with that of the analysis model in the next section.

Note that subsequent tests underway at JPL have indicated that many of the unresolved modes that are present in the test models are due to the elastic behavior of the suspension system. In particular, test mode 9 was found to be a spring surge mode—

elastic motion associated with axial compressive waves in the spring. This type of behavior is definitely undesirable, further complicating the task of identifying the structure itself using experimental data only. These suspension system modes were particularly troublesome because they were clearly present in the measurement data and were hard to discern from the system modes of the structure even though they occurred with relatively low amplitudes.

As the last step in the analysis of the modal test data, a number of FRF's were generated using the experimental modal parameters. These resynthesized FRF's were compared to the original measured data to evaluate how closely the modal model synthesis fit the measured data. Figure 5 shows one of these comparisons for the cross-driving-point FRF, which was typical of most of the resynthesized FRF's. Visual inspection indicates that this resynthesis reproduces the measured data quite well, lending great confidence in the data reduction portion of the modal test.

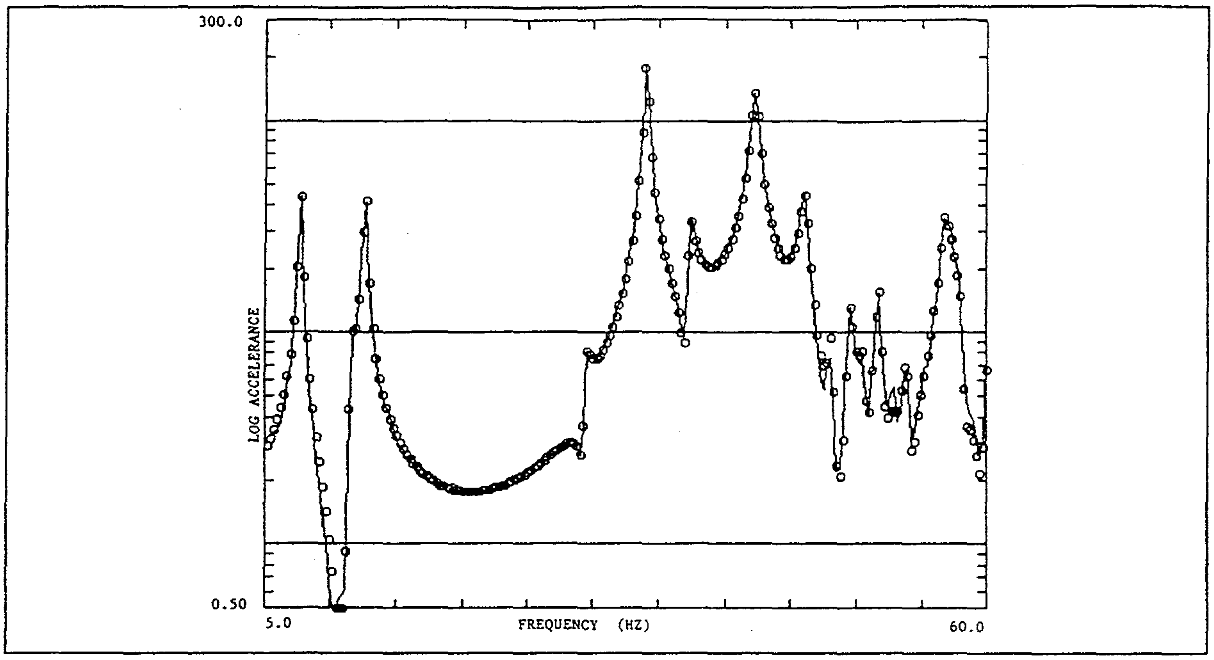

Figure 5: Cross Driving Point FRF's—Measured and Resynthesized

Analysis

As a result of the system identification at the component level, the full system analytical model agreed well with the initial test-derived model—especially for the first eight system modes. Thus, initial focus was on resolving various discrepancies that existed at higher frequencies through re-examination of the test-derived model. Future studies will concentrate on a final, refined estimate of parameters in the full system. This study underscores the need to consider both models, test and analysis, as equals in the reconciliation process. An important fact is that any change in the test model inferred from the reconciliation process does not necessarily imply that a full retest will be needed. For example, it may indicate a need to perform a revised data reduction on the existing test data, for which there is some subjectivity on the part of the experimentalist.

For the structure under consideration, an initial test model was extracted from the test data and compared with the analytical model, which had been assembled from the identified subsystem elements. This initial reconciliation process motivated refinements in the test model. Discrepancies that still remain require further refinement of the analytical model. This will be resolved by performing full system parameter estimation on physical elements that were not included in the component level test series and by including a model of the suspension system in the full system model.

Test/Analysis Mode Comparison

There are two aspects to comparing a set of test and analysis mode shapes, correspondence and accuracy. The first task is to determine which modes should be paired for comparison and correlation. The second task is to assess the "closeness" of the identified mode pairs by quantifying the discrepancies. Moreover, when acceptable correspondence cannot be established, their relation to the surrounding modes must be established. The traditional metric for mode agreement is the modal assurance criterion (MAC) also referred to as the mode shape correlation coefficient [13]. This metric is convenient since it does not depend on normalization of the modes and it reduces the mode pair agreement to a single scalar value. Although there is some ambiguity in its definition, this paper uses a non-squared version of the MAC defined as

$$\mathrm{MAC} \equiv \mathrm{MAC}_{ns} \equiv \frac{\phi_a^T \phi_e}{|\phi_a|\ |\phi_e|} \tag{1}$$

where ϕ_a and ϕ_e are single analytical and experimental mode shape vectors, respectively, T denotes the transposition operator and $|\cdot|$ is the Euclidean norm. The MAC does have its deficiencies however. For instance, no one has been able to establish a clear numerical range over which MAC's guarantee correspondence. Other advanced metrics are being developed which provide additional insight into mode correspondence, quantify similarity to surrounding modes and characterize errors in mode shape pairs. Studies employing these metrics will be reported in [14].

Results

With the tools cited above the process of finding Test Set 1 modes which corresponded to analysis modes was undertaken. The first eight modes, six of which are shown in Figure 6, were system modes with a high degree of correlation. Table 4 quantifies many of the results. The first and second columns sequentially list the FEM and test modes by increasing frequency and are aligned with their best counterparts—accepted mode pairs are indicated with a (*) in the far right-hand column. A dashed line with an embedded mode number in either of these columns indicates that two comparison modes had their highest MAC values for that mode number with the higher of the two taking precedence. The dashes in the remaining columns are also an indication that this has occurred. Examination of the table shows that three analysis modes, 16, 19, and 20 had no apparent counterparts in the test-derived modal model; nor did test modes 9, 11, and 13. Plots of displacement shapes for FEM modes 19 and 20 indicated that they were the orthogonal pair corresponding to test mode 11, a local mode. MAC calculations had

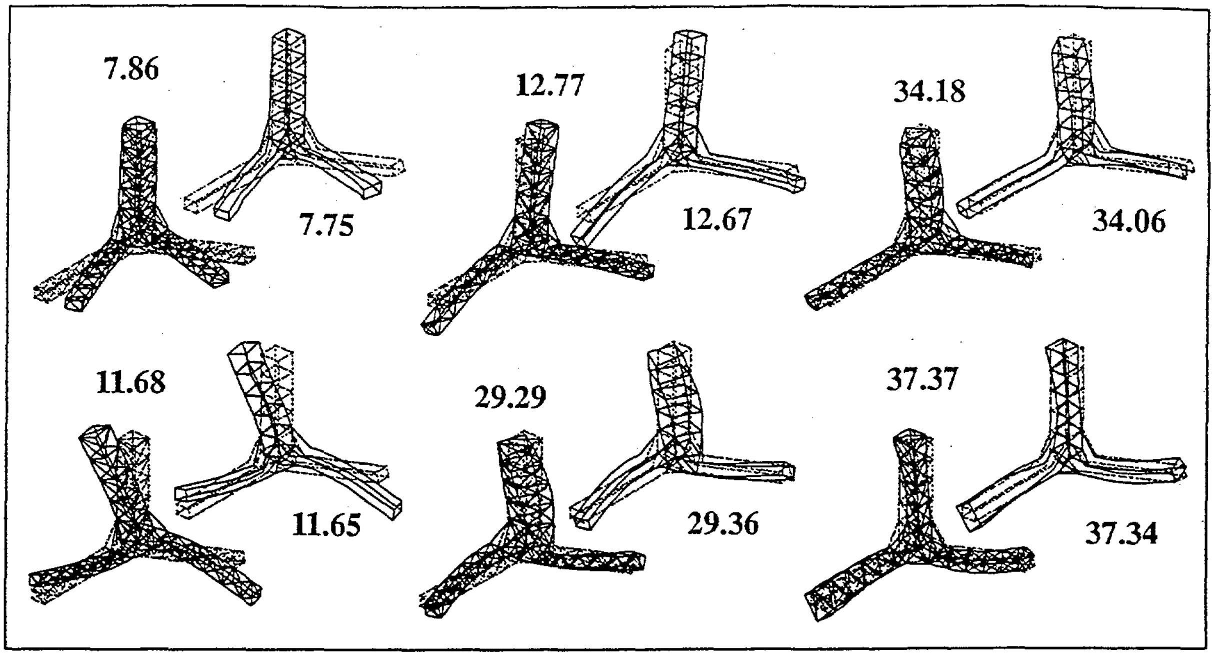

Figure 6: First Six Pairs of Test and Analysis Modes

failed to give this result due to the omission of mid strut nodes in the test displacement set. In fact, the MAC value of 0.9441 for FEM mode 20 and test mode 14 is explicit evidence of the need for extreme caution when establishing modal correspondence based on this criterion alone. Our overriding goal became to find the test mode corresponding to FEM mode 16.

Test Set 2 was then extracted from the measurement data. The results associated with this set are shown in Table 5 where the first eight mode pairs have been omitted for brevity (they are identical to those of Table 4). In the test mode column, three new modes are shown in bold. In this new set, FEM mode 16 now has a counterpart in test mode 11.

While this resolved the issue of correlating analysis modes to those present in the test model, there are still a number of modes that are present in the test mode set that have yet to be resolved. These modes have been the object of some concern and additional test procedures have been performed that seem to indicate that they are associated with the suspension system. This subject remains under investigation.

Concluding Remarks

The JPL MPI Testbed is an example of a repeatable, linear, high precision structure. As such, it affords an opportunity to refine analytical modeling and structural system identification procedures.

To facilitate an accurate structural characterization the testing and the test-analysis reconciliation processes were separated into two stages, one each for the component and system levels. The first stage involved a component level test-analysis series which focused on two primary objectives: (1) the identification of an appropriate model form for the

FEM Frequency/#	Test Set 1 Frequency/#	Maximum FEM MAC	Maximum Test MAC	Frequency Error(%)
7.86/7	7.75/1	0.9984	0.9984	1.42(*)
11.68/8	11.65/2	0.9966	0.9966	0.26(*)
12.77/9	12.67/3	0.9971	0.9971	0.79(*)
29.29/10	29.36/4	0.9978	0.9978	-0.24(*)
34.18/11	34.06/5	0.9985	0.9985	0.35(*)
37.37/12	37.34/6	0.9950	0.9950	0.08(*)
42.43/13	42.25/7	0.9960	0.9960	0.43(*)
46.08/14	46.04/8	0.9955	0.9955	0.09(*)
-15-	48.06/9	—	0.7474	—
49.37/15	49.50/10	0.9890	0.9890	-0.26(*)
51.11/16	51.69/11	0.7696	0.7696	-1.12
53.80/17	53.00/12	0.9677	0.9677	1.51(*)
-17-	56.87/13	—	0.7714	—
56.72/18	58.01/14	0.9628	0.9628	-2.22(*)
58.58/19	-15-	0.6824	—	—
59.14/20	-14-	0.9441	—	—
60.26/21	60.04/15	0.9836	0.9836	0.37(*)

Table 4: MPI FEM/Test Set 1 Comparison

Node Ball/B-Nut/End Cap/Strut subsystem and (2) the estimation of a suitable set of "nominal" physical parameter values for this model. Modal test results were presented for the various configurations that were considered.

The test-analysis model reconciliation approach was based on estimating physical parameters in finite element models of each configuration. Such an approach provides an advantage over other methods by allowing results to be extrapolated to different configurations. For the current task, parameter estimation was performed via two techniques: a design sensitivity based approach using modal frequency information and a Bayesian approach which also incorporated mode shape data. A multiple configuration reconciliation approach resulted in an update of the model form and initial nominal physical parameter values for the structural subsystems which were to be incorporated into the system model.

The second stage concerned the identification of the full system model. Results of the system level modal test were presented. Structural system identification techniques were instrumental in refining the initial experimental modal model development. These developments underscore not only the essential need for communication between the analyst and the experimentalist, but also the equal footing on which both test and analysis rest in the system identification process. The full system model was produced by replicating the model form and parameter estimation results from the component level results. The initial system showed good agreement with modal test results for the system modes in the frequency range of interest.

FEM Frequency/#	Test Set 2 Frequency/#	Maximum FEM MAC	Maximum Test MAC	Frequency Error(%)
-15-	48.06/9	—	0.7605	—
49.37/15	49.50/10	0.9890	0.9890	-0.26(*)
51.11/16	**50.63/11**	0.9364	0.9364	0.95(*)
-16-	51.69/12	—	0.7696	—
53.80/17	53.00/13	0.9677	0.9677	1.51(*)
-17-	**53.96/14**	—	0.9116	—
-17-	56.82/15	—	0.7658	—
-18-	**57.26/16**	—	0.7150	—
56.72/18	58.01/17	0.9628	0.9628	-2.22(*)
58.58/19	-18-	0.6824	—	—
59.14/20	-17-	0.9441	—	—
60.26/21	60.04/18	0.9836	0.9836	0.37(*)

Table 5: MPI FEM/Test Set 2 Comparison

Finally, it is imperative that the analysis model capture the qualitative properties exhibited by the test article and that instrumentation planning be done accordingly to ensure these phenomena are measured in the test. For this case, testing was done with the structure suspended via "soft" springs—an approximation to an analytical free-free condition. However, initial indications were that the structural dynamics of the suspension suspension system greatly affected the acquired test data. Future work at the system level will examine such issues in greater detail.

Further plans also include: (1) addressing the issue of when the system identification procedure should be considered complete. For example, our focus has been on reconciling modal models, but other characterizations of the response such as those described by FRF's and state-space models might be more suitable, (2) consideration of physical uncertainty in the prediction of system response, (3) local mode characterization and mitigation, (4) structural modification verification, and (5) establishing metrics for selecting optimal excitation, measurement and suspension system locations.

Acknowledgements

Thanks is extended to the remaining members of the JPL CSI team, Marie Levine and Rob Calvet, whose work contributed this article. Also, a portion of this work was performed at Sandia National Laboratories under the support of the U.S. Department of Energy contract number DE-AC04-76DP00789. This support was greatly appreciated.

References

[1] R. A. Laskin and M. S. Martin. Control/Structure System Design of a Spaceborne Optical Interferometer. In *Proceedings of the AAS/AIAA Astrodynamics Specialist Conference*, 1989.

[2] J. T. Spanos et al. Control Structure Interaction in Long Baseline Space Interferometers. In *Proceedings of 12th IFAC Symposium on Automatic Control in Aerospace*, Ottobrunn, Germany, 1992.

[3] J. A. Garba, B. K. Wada, and J. L. Fanson. Adaptive Structures for Precision Controlled Large Space Systems. *J. of Intell. Mater. Syst. and Struct.* **3**, 348–366 (1992).

[4] M. Shao et al. Mark III Stellar Interferometer. *Astron. Astrophys.* **193**, 357–371 (1988).

[5] J. L. Fanson and J. A. Garba. Experimental studies of active members in control of large space structures. In *Proceedings of the 29th AIAA SDM Conference*, pages 9–17, Williamsburg, VA, 1988.

[6] J. T. Spanos and A. Kissil. Modeling and Identification of the JPL Phase B Testbed. In *Proceedings of AIAA/ASME/SPIE Conference on Active Materials and Adaptive Structures*, Alexandria, VA, 1991.

[7] E. L. Marek, R. L. Mayes, and T. G. Carne. Modal Survey and Test-Analysis Correlation of a Multiply Configured Three Stage Booster. In *Proc. of Conference on Active Materials and Adaptive Structures*, pages 837–852, 1991.

[8] D. R. Martinez, J. R. Red-Horse, and J. J. Allen. System Identification Methods for Dynamic Structural Models of Electronic Packages. In *Proceedings of the 1991 Structures, Structural Dynamics and Materials Conference*, 1991.

[9] C. Flanagan. Users Guide for CORDS2. Technical report, Structural Dynamics Research Corporation, San Diego, California, 1988.

[10] T. K. Hasselman and J. D. Chrostowski. SSID—A Computer Code For Structural System Identification. Technical Report TR-91-1134-1, Engineering Mechanics Associates, Inc., 3820 Del Amo Blvd, Suite 318, Torrance, CA, 1991.

[11] H. Vold and G. F. Rocklin. The Numerical Implementation of a Multi-Input Modal Estimation Method for Minicomputers. In *Proceedings of the 1st IMAC*, pages 542–548, 1982.

[12] R. L. Mayes. A Multi Degree of Freedom Mode Shape Estimatin Using Quadrature Response. In *Proceedings of the 11th IMAC (to appear)*, 1993.

[13] D. J. Ewins. *Modal Testing: Theory and Practice*. John Wiley and Sons, 1984.

[14] J. R. Red-Horse, E. L. Marek, and M. Levine. System Identification of the JPL Micro-Precision Interferometer Truss: Test-Analysis Model Reconciliation. In *Proceedings of the 34th SDM (to appear)*, 1993.

SYSTEM IDENTIFICATION OF THE JPL MICRO-PRECISION INTERFEROMETER TRUSS: TEST-ANALYSIS RECONCILIATION

J. R. Red-Horse[1], E. L. Marek
Sandia National Laboratories
Albuquerque, NM

M. Levine-West
Jet Propulsion Laboratory
Pasadena, CA

Abstract

The JPL Micro-Precision Interferometer (MPI) is a testbed for studying the use of control-structure interaction technology in the design of space-based interferometers. A layered control architecture will be employed to regulate the interferometer optical system to tolerances in the nanometer range. An important aspect of designing and implementing the control schemes for such a system is the need for high fidelity, test-verified analytical structural models. This paper focuses on one aspect of the effort to produce such a model for the MPI structure, test-analysis model reconciliation. Pretest analysis, modal testing, and model refinement results are summarized for a series of tests at both the component and full system levels.

Introduction

Background

New generation structural design applications, ranging from concurrent design engineering to large space structures integrated with structural control schemes, has placed increasing reliance on accurate computational modeling capabilities. This has motivated renewed emphasis on the ability to model analytically structural dynamics phenomena. The processes associated with the development of high precision analytical models, referred to collectively as *structural system identification*, are complex indeed. They encompass the diverse tasks of testing, analysis and model reconciliation. Testing aspects include building a suitable physical specimen, making accurate measurements, and deriving a test model from the measured data; while analysis generally entails developing a finite element model (FEM) of the hardware in the tested configuration. Both of these areas have separately enjoyed periods of immense growth. Until very recently, however, the reconciliation of differences that inevitably exist between the test and analysis results have been handled by heuristically based, ad-hoc procedures. Such approaches are rapidly being replaced by more quantitative methods.

One path to model reconciliation, often referred to as parameter identification [1], is concerned with the development of systematic tools for use in estimating parameters in an analysis model which appropriately update it to achieve better agreement with test data. Two general methodologies exist in parameter identification of dynamic structural models. The first of these techniques falls into the class of non-iterative, or one-step methods [2, 3]. These methods estimate individual entries of the associated system mass and stiffness matrices; and as such, do not require any model design sensitivity information. They are based on a closed-form minimization problem and require only measured modal information and the mass and stiffness matrices from the finite element model. The updated mass and stiffness matrices exactly reproduce the experimental modal frequencies and mode shapes at predetermined points on the structure. To date, no one-step method accounts for the existence of uncertainty in the data. The second of these classes, which involves the estimation of physical parameters, contains procedures that are based on iterative estimation methods [4, 5]. These methods include generalized nonlinear least squares schemes, which assume deterministic data, and algorithms based on Bayes estimation, which approach the problem from a probabilistic point of view. Estimation schemes based on the latter approach account for uncertainty in both the experimental data and the model parameters.

The subject of this paper is the test-analysis model reconciliation of the Jet Propulsion Laboratory's (JPL) Micro-Precision Interferometer (MPI) testbed.

Micro-Precision Interferometer

As a major component of NASA's Focus Mission spacecraft development project [6], the JPL Control Structure Interaction (CSI) team is developing capabilities specific to the design of Micro-Precision Controlled Structures for flight systems such as optical interferometers [7]. These systems, including the target system known as the Focus Mission Interferometer (FMI), will be single payload structures with fixed truss geometry and are expected to fly in low earth orbit. The structures will be composed of identical bays and components connected through multi-directional ball

---

[1] John Red-Horse, Dept 1434, Sandia National Laboratories, P.O. Box 5800, Albuquerque, NM 87185

Copyright ©1993 by the American Institute of Aeronautics and Astronautics, Inc. All Rights Reserved.

joints. Structural subsystems will support the necessary electronics and optical metrology equipment. Some members in each structure will be replaced by passive dampers or active members for vibration suppression and control purposes.

Several testbeds exist at JPL to validate the various CSI technology goals required for the FMI [8]. All of these testbeds possess the structural characteristics listed above, thus providing a useful application for system identification technology validation. The MPI truss is a partial, scale model of the FMI comprised of two booms and a vertical tower, 7mx6.3mx5.5m, weighing 210kg. A more definitive discussion of the MPI, and its role in the JPL CSI mission can be found in [9].

Of particular interest are the controlled manner under which this structure was manufactured and assembled, and on the configuration change management scheme that JPL intends to employ. Stringent relative path length requirements imposed by the use of interferometry necessitate the implementation of both active and passive structural vibration control schemes. To reliably investigate a number of these schemes, the analytical models should be capable of representing the physical structure through numerous configuration changes—both those encountered during the design phase in the testbed and those expected in the actual operation of the telescope.

System Identification Approach

The philosophical approach in developing the models was to seek to identify the structure by determining both an appropriate model form and a corresponding physical parameter set through a coordinated three-pronged approach linking the test, analysis and reconciliation phases described above. It is an approach that must be totally integrated in the development of large space structural applications [10]. While it is not the subject of this article, the procedure implicitly requires the evaluation of uncertainty intervals associated with the estimated parameters [11, 12].

For a variety of reasons, the identification was performed in two stages: First, a component level identification procedure was performed. Second, results from this initial phase were incorporated into the identification of the full system.

Specific tasks include pre-test analyses, joint characterization modeling and testing, suspension system design, modal testing and parameter estimation, finite element modeling, test-analysis reconciliation and quantification of thermal and gravitational effects.

The current study concentrates on the issues relating to the reconciliation effort. The first stage considered model reconciliation for a series of modal tests at the subsystem level while the second stage was concerned with the full system model. For the subsystem level reconciliation, two iterative identification procedures were exercised: Bayes estimation [13], implemented in the software package `SSID` [14], and Design Sensitivity Analysis (DSA) as it is implemented in the SDRC software package `CORDS` [15].

Each of the above procedures utilizes output from the general purpose finite element program `MSC/NASTRAN`. `CORDS` requires only DSA information, while `SSID` requires a great deal more. Specifically, one must obtain the system mass and stiffness matrices along with the mass and stiffness matrix sensitivities for each design parameter. Acquiring this sensitivity information from `NASTRAN` requires a customized `DMAP` solution sequence and a translator capable of communicating it (`NASSID` [16]). `SSID` then uses the information for performing eigenanalyses and in the computation of eigenvalue and eigenvector sensitivities internally using a modal summation approximation. Note that both estimation programs also perform approximate model updates internally, although `SSID` does this at the system matrix level using a truncated Taylor series approximation. This system level approach has the additional advantage of requiring far fewer loops back into the finite element code than is necessary for `CORDS`. In fact, for cases where the system mass and stiffness matrices are linear in the parameters, there is no need to return to `NASTRAN` since the Taylor series update will be exact.

Full system level model reconciliation considered only the Bayesian estimation scheme. A primary concern for such systems is the correct formulation of the problem statement. For modal models this requires one to establish the correspondence between modes in the test and analysis models. For complicated structures this is a nontrivial step.

Component Level Identification

Modal Tests

The MPI testbed is constructed of a few basic components that are replicated many times throughout the structure. Therefore, it seemed plausible that accurate finite element models of these components would lead to an accurate model of the assembled structure. These components are located and identified in Figure 1.

The component level test plan had two objectives. The first was to provide data to determine the nominal physical parameter values associated with the bending and axial stiffnesses of the struts, strut end caps, and B-Nut connectors which attached each strut to the node balls. The second was to provide data for deterministically quantifying phenomena that might cause variations in the parameter values. The phenomena that were chosen to be addressed were: (1) Dynamic amplitude of vibration, (2) Static strut loading (e.g. from gravitational or nonuniform thermal loads), (3) B-Nut installation torque, and (4) B-Nut installation length. In this section, we concentrate on results relating to

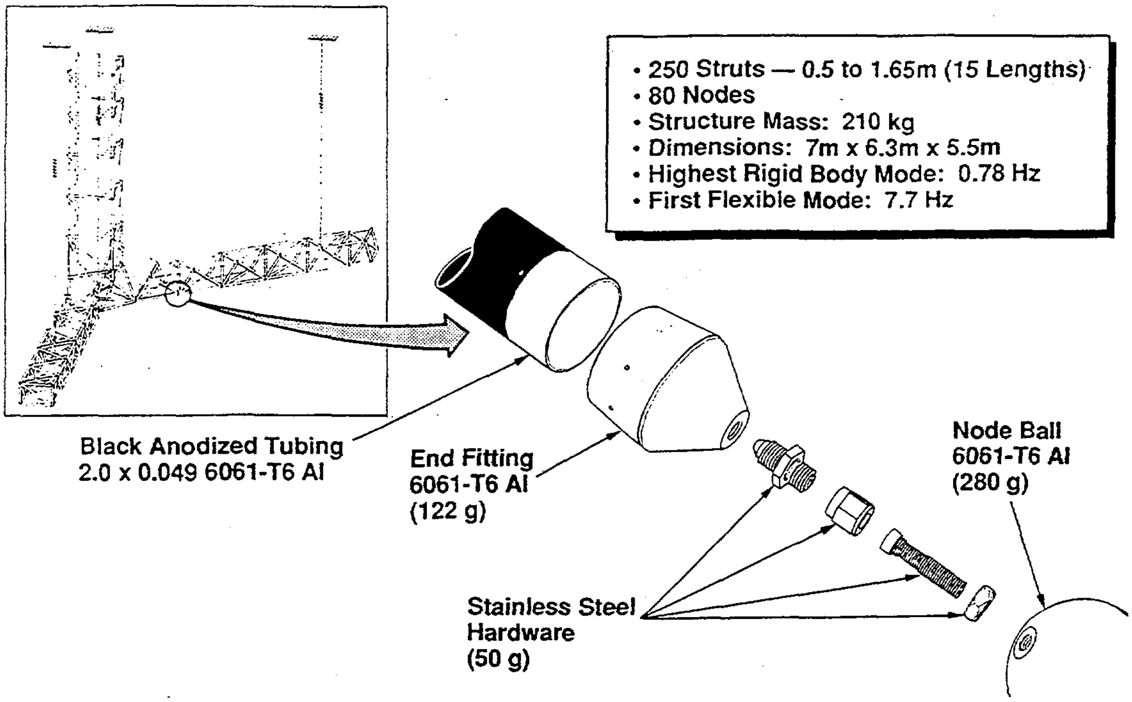

- 250 Struts — 0.5 to 1.65m (15 Lengths)
- 80 Nodes
- Structure Mass: 210 kg
- Dimensions: 7m x 6.3m x 5.5m
- Highest Rigid Body Mode: 0.78 Hz
- First Flexible Mode: 7.7 Hz

Figure 1: MPI and Exploded Subsystem Components

the first objective—determining the nominal stiffness parameters.

Nominal Component Parameter Characterization

Figure 2 shows the seven configurations of the node balls, struts and B-Nut assemblies that were tested. All except Configuration 4 were used to provide data to meet the first objective described above. Each configuration was suspended by soft shock cords and string so that the rigid body modes would be well separated in frequency from the first elastic mode. In each configuration a small impact hammer with a force transducer was used to impact one of the end balls longitudinally to excite the first axial mode. Each configuration was also impacted laterally at the middle ball (or the middle of the strut if there was no middle ball) to excite the first bending mode. Frequencies, damping and mode shapes were extracted for the first elastic mode in each impact direction from frequency response functions (FRF's) of the accelerometers to the input hammer force. Five averages were taken to form each FRF estimate. Table 1 lists the results of these tests which were subsequently used in the parameter identification schemes. Further information on the component-level tests can be found in [17].

Analytical Parameter Identification

Here the task was to identify the structural elements at the subsystem level from the results of the modal test series. This identification results in both an appropriate model form as well as estimates for the accompanying nominal parameter values.

Parameter estimation was accomplished for all subsystem configurations and parameters (i.e., those affecting both axial and bending response) using a DSA approach. As a validation step, the parameters affecting the lateral response characteristics were also estimated using a Bayesian estimation algorithm.

Model form issues were addressed by simultaneously considering multiple subsystem configurations in `CORDS`, and by seeking consistent results for all individual configurations in `SSID`. The premise of this approach is that parameterizations cannot support accuracy across a variety of configurations if the model form of the structural subsystem does not capture the correct qualitative structural behavior. The final model form was comprised of point masses for the node balls with rigid elements from these points to their geometrical radii and three beams: one each for the B-Nut assembly, end cap, and strut. Each beam element accounted for mass via nonstructural mass specifications which decoupled it from the physical parameters for each beam: cross sectional areas and moments of inertia.

The reconciliation procedure was separated into two phases with the axial and bending characteristics considered independently.

Axial Characteristics

For this parameter set correlation was performed using the DSA approach with data from each of Configurations 1 through 7 (with the exception of Configuration 4) stacked in a single response vector. The re-

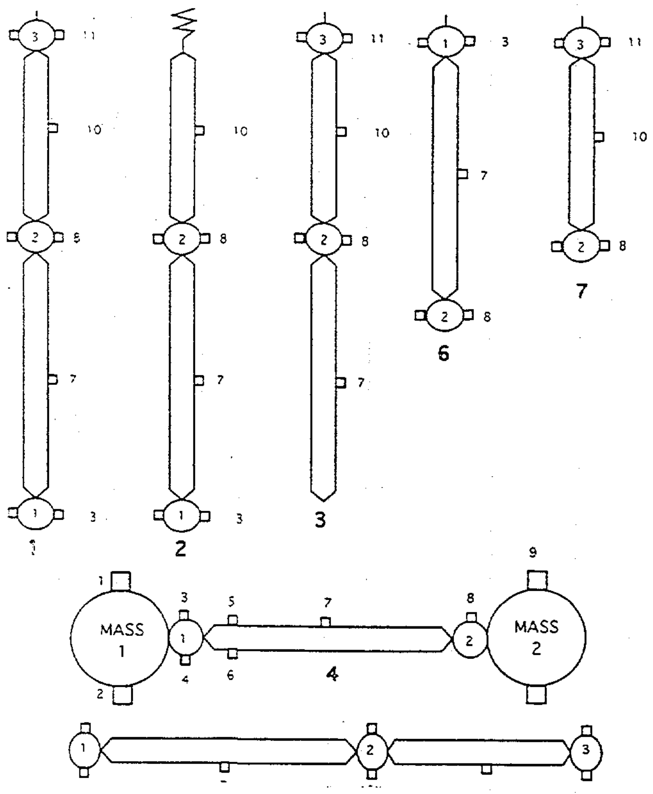

Figure 2: Seven Tested Subsystem Configurations

Configuration	Bending Properties		Axial Properties	
	Freq (Hz)	Damping (%)	Freq (Hz)	Damping (%)
1	12.26	1.0	826.3	0.1
2	15.91	0.5	942.2	0.1
3	13.95	0.4	1013.2	0.1
5	12.09	0.5	825.5	0.2
6	133.56	0.6	1202.3	0.3
7	165.5	0.4	1518.5	0.1

Table 1: Nominal Modal Results for the Component Tests

Config/ Item	Axial Results			Bending Results		
	Initial	Final	Test Freq (Hz)	Initial	Final	Test Freq (Hz)
1	815.2	825.7	826.3	13.20	12.25	12.26
2	928.7	941.7	942.2	17.04	15.83	15.91
3	1003	1015	1013	14.99	13.92	13.95
6	1162	1181	1202	148.9	133.4	133.5
7	1470	1490	1519	198.6	167.2	165.5
A_{strut}	0.3003	0.3123	—	—	—	—
A_{bnut}	0.0700	0.0672	—	—	—	—
I_{bnut}	—	—	—	$4.0(10^{-4})$	$4.01(10^{-4})$	—
I_{endcap}	—	—	—	0.0477	0.00856	—

Table 2: Component-Level Reconciliation Results

Freq No/ Item	Initial FEM	Final FEM	Test (Hz)
1	6.07	6.23	6.21
2	8.76	9.02	9.04
3	112.1	114.9	115.2
$I_{longbnut}$	$4.0(10^{-4})$	$3.77(10^{-4})$	—

Table 3: Config 4 (long B-Nut) Reconciliation Results

sults are summarized in Table 2. A consistent update was achieved with good test-analysis model agreement across the configuration set.

Bending Characteristics

The DSA approach was also taken for estimating the bending parameters. In addition, the Bayesian approach described above was implemented for which formal consideration was given to both modal frequency and shape data. A particularly striking result was that both methods produced parameter estimates which were quite consistent. These results are also shown in Table 2, where one can observe the good correlation for each member of the configuration set.

Configuration 4

Configuration 4 from the original test series was not considered in the reconciliation process due to the effects of the connections between the large masses and the node balls. However, this test was repeated with longer versions of the B-Nut assembly for the purpose of gaining insight into the effects of B-Nut length on the response characteristics. An attempt was made to reconcile the test and analysis models for one particular B-Nut length (3.1in). Both methods yielded good agreement for the axial properties, but the bending characteristics proved problematic. Estimation was performed using the first three bending modes without achieving consistent results. A close examination of the third bending mode shape revealed that a qualitative response property, namely rotational motion between the large end mass and the node ball, had not been captured by the initial model form. Resolving this issue and re-estimating yielded consistent results which are shown in Table 3.

Some Observations

It is worth noting that without an appropriate selection of "correlation" data, that effectively serve as weighting data for the Bayes estimation procedure, the estimated parameter sets varied between the classes of substructure configurations (those in configurations 1–3 and 6–7). It is this behavior that prompted a closer look at the procedure itself (cf. Appendix A.).

One assumption that is made in Bayesian estimation is that the log likelihood function is sharply peaked about a unique global minimum [13]. In practice this is rarely the case. Beck and Katafygiotis [18] generalize this notion by defining those models for which either a global minimum exists, or a finite number of global minima exist as *system identifiable*. Models other than this type are deemed to be *system unidentifiable*.

For our case, the mere existence of multiple extrema makes the selection of the weighting data much more important. These data indicate to the estimator which of these minima get emphasized. Our results imply that by employing a multiple configuration methodology, where the "rank" [19] of the combined problem is at least as large as the number of independent parameters, this essential problem has been mitigated.

System Level Identification

Modal Testing

In contrast to the component testing, which was designed to focus on localized behavior in simple structural elements, the system level modal test was intended to exercise the entire MPI structure with all of the structural elements interacting. The primary objectives of the system level test were to obtain laboratory measurements of the dynamic properties of the structure and to provide the data necessary for building an accurate analytical model.

The structure was supported by soft springs in the laboratory to simulate a free-free environment which would best mimic the operational environment of the MPI. Modal data were extracted in the range 0–60Hz.

Supporting the structure so that free boundary conditions were well approximated was a very important aspect of the pre-test planning. For this test the MPI was suspended from three points with assemblies consisting of steel coil springs and light weight steel cables which produced rigid body modes in a range below 1Hz.

Utilizing a pre-test analysis model to generate mode shapes, FRF's, and mode indicator functions, two shaker locations were chosen at the ends of the two booms. The directions of the input forces was diagonal to the end-faces of the booms and oriented to produce torsional response. Two portable fifty-pound shakers were used for excitation. Each of the eighty node balls of the truss structure was instrumented with a tri-axial accelerometer. Additional accelerometers were also placed at a variety of strategic locations, such as mid-strut locations for longer members and suspension system attachment points, to achieve the detailed mode shape information necessitated by the uncertain data requirements of the test-analysis model reconciliation task. Figure 3 depicts the MPI in this initial tested configuration. The results of the modal test and subse-

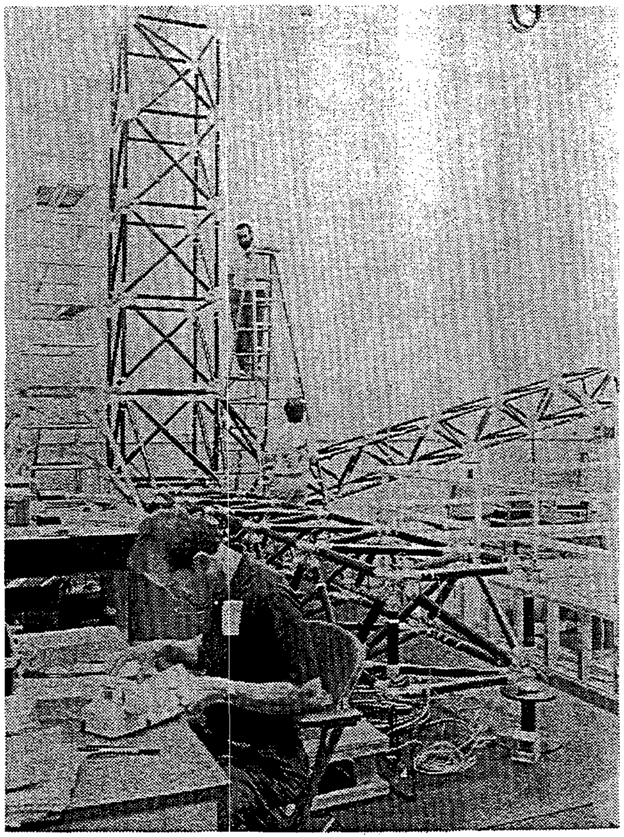

Figure 3: Photo of Tested MPI

quent data reduction sets appear in subsequent tables where comparisons are made with analysis predictions. For more complete details regarding the modal tests the interested reader should consult [17, 9].

This initial test was followed up by a series of modal tests, individually smaller in scope than the first survey, to provide sufficient data for investigating the predictive nature of the resulting FEM model. This test series is discussed in detail in [17].

In this section we first discuss the test-analysis reconciliation, along with a variety of issues concerning the process, for the bare MPI. In addition, we compare the results of analysis predictions to those arrived at via testing for one case of a modified MPI.

Analysis

As a result of successful component level identification, the full system analytical model agreed well with the initial test-derived model—especially for the first eight system modes. Thus, initial focus was on resolving various discrepancies that existed at higher frequencies through re-examination of the test-derived model. Studies then concentrated on a final, refined estimate of parameters in the full system. Our study underscores the need to consider both models, test and analysis, as equals in the reconciliation process. An important, though often understated, fact is that changes in test models inferred from the reconciliation process do not necessarily imply that a full retest is required. They may indicate a need to perform a revised data reduction on the existing test data, for which there is some subjectivity on the part of the experimentalist.

For the structure under consideration, the process was as follows: a first pretest analysis model was developed that contained only axial rod elements connected with pin joints. This model was then modified to conform with results of the component identification. The structure was tested and an initial test model was extracted from the resulting measurement data and compared with the latest analytical model, which was being modified in a parallel effort. This initial reconciliation process motivated refinements in the test model. Discrepancies that remain require further refinements to the analytical model.

Test-Analysis Mode Correspondence

The model reconciliation process for structural dynamics applications generally utilizes test model data in the form of either modal (natural frequencies and/or mode shapes) or FRF data. For cases such as ours, where modal frequency data are used, the first task is to determine which test-analysis mode pairs should be selected for comparison. Only then can their closeness be assessed. Several steps must be taken to (1) identify correspondence among modes, (2) isolate and understand differences (errors) between two paired mode shapes, (3) relate mode shapes and mode shape errors to surrounding modes and (4) explain unmatched modes.

The traditional metric for mode agreement is the modal assurance criterion (MAC) also referred to as the mode shape correlation coefficient [20]. This metric is convenient for three reasons: first, it does not depend on normalization of the modes (a particularly vexing problem introduced by the lack of a test derived modal mass), second, it considers only those degrees of freedom that exist in both the test and analysis models, and finally, it quantifies mode pair agreement with a single scalar value. There is some ambiguity in the definition of the MAC. This paper uses the following

$$\mathrm{MAC} \equiv \mathrm{MAC}_{ns} \equiv \frac{\phi_a^T \phi_e}{|\phi_a|\;|\phi_e|} \tag{1}$$

where ϕ_a and ϕ_e are single analytical and experimental mode shape vectors, respectively, T denotes the transposition operator and $|\cdot|$ is the Euclidean norm. The MAC does have its deficiencies. For instance, it is not possible to establish a clear numerical range over which MAC's guarantee correspondence, or lack thereof. It would appear that such criteria are dependent on a number of issues, such as the class of structure under consideration, or the degrees of freedom to be incorporated in the computation.

Other Correspondence Metrics

Other advanced metrics are being explored which provide additional insight into mode correspondence, quantify similarity to surrounding modes and characterize errors in mode shape pairs.

When attempting to use entries in mode shape vectors an unexpected issue appears: how does one scale the shape vectors so that the subsequent comparison is unbiased. This is always defined for the analysis modes which are normalized with respect to their mass matrix. However, test results often do not include a reliable test derived modal mass with which to perform this normalization. One approach is to minimize the mean square error between corresponding pairs of mode shapes [21].

The following approach, referred to as Minimum Error Mode Superposition (MEMS), is an extension of the above idea to multiple dimensions. Consider comparing a group of modes from one set (either the test or analysis) to a single reference mode from the other. MEMS is concerned with choosing the *set* of scale factors which minimizes the mean square error between the superposition of the selected group of comparison modes and the reference mode. Specifically, define the mean square error, e^2, as follows

$$e^2 = \frac{\left(\phi_a - \sum_{i=1}^{N} \alpha_i \phi_{e_i}\right)^T \left(\phi_a - \sum_{i=1}^{N} \alpha_i \phi_{e_i}\right)}{\phi_a^T \phi_a} \tag{2}$$

where the α_i are the least squares estimates for representing the reference mode in terms of the comparison mode set. The relative values of the α_i can be useful in identifying mode correspondence and in assessing any mixing that may occur in adjacent modes. One problem with this approach involves the arbitrary scaling of the comparison set. If these are FEM modes, the mass orthonormalization will scale the set consistently. However, if the comparison set is comprised of test modes, the scaling can vary widely and a procedure for consistently scaling the comparison set must be devised. One possibility is to use a test derived modal mass, when available. Other alternatives include the use of a reduced order analysis mass matrix, or normalizing each mode shape to unity magnitude. Note that the α_i can be substituted into Eq. 2 to calculate the mean square error, and that a MAC value can be calculated between the reference mode and the sum of comparison modes

A second correspondence tool is the concept of an *error mode*. Here, we seek to establish the nature of mode mixing by examining the shape of the error vector, $\hat{e}$, that remains after best fitting it to a given set of correspondence modes as described above. The definition for $\hat{e}$ is,

$$\hat{e} = \phi_a - \sum_{i=1}^{N} \alpha_i \phi_{e_i} \tag{3}$$

The point of this exercise is to look for systematic tendencies in the error shape as an indication of whether or not the reference mode is being well represented by the correspondence.

Examples of these metrics are displayed in Figure 4.

Both of the above topics are currently under investigation and in this study were used for qualitative information only.

Some recent work which also shows promise involves a process for selectively choosing which degrees of freedom to include in the various correspondence measures. This process accounts for the individual contributions of each of the degrees of freedom to the correspondence measure under consideration [22, 23].

Results

With the tools cited above the process of finding experimental modes from what will be referred to as *Test Set 1* which corresponded to analysis modes was undertaken. The analysis modes were from the FEM model developed as a result of the subsystem level test series. The first eight modes, six of which are shown in Figure 5, were system modes with a high degree of correlation. Table 4 quantifies many of the results. The first and second columns sequentially list the FEM and test modes by increasing frequency and are aligned with their best counterparts—accepted mode pairs are indicated with a (*) in the far right-hand column. A dashed line with an embedded mode number in either of these columns indicates that two comparison modes had their highest MAC values for that mode number with the higher of the two taking precedence. The dashes in the remaining columns are also an indication that this has occurred. Examination of the table shows that three analysis modes, 10, 13, and 14 had no apparent counterparts in the test-derived modal model; nor did test modes 9, 11, and 13. Plots of displacement shapes for FEM modes 13 and 14 indicated that they were an orthogonal pair corresponding to test mode 11, a local strut mode. MAC calculations had failed to give this result due to the omission of mid strut nodes in the test displacement set. In fact, the MAC value of 0.9441 for FEM mode 14 and test mode 14 is explicit evidence of the need for extreme caution when establishing modal correspondence based on this criterion alone. As a result of this investigation, our goal became to find a test-derived model with a mode which corresponded to FEM mode 10.

Test Set 2 was then extracted from the measurement data. The results associated with this set are shown in Table 5 where the first eight mode pairs have been omitted for brevity (they are identical to those of Table 4). In the test mode column, three new modes are shown in bold. In this new set, FEM mode 10 now has a counterpart in test mode 11.

This resolved the issue of correlating test modes to those present in the FEM model, there are still a number of modes that are present in the test set that have

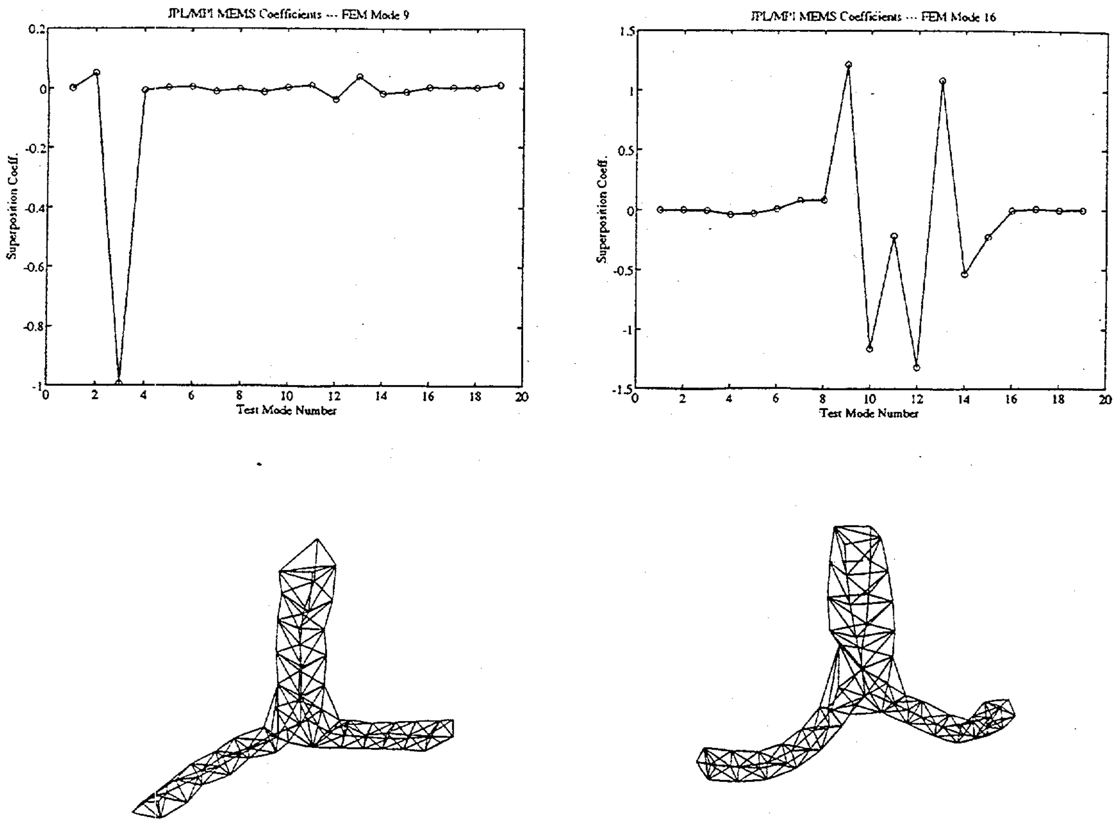

Figure 4: Example MEMS and Error Shapes

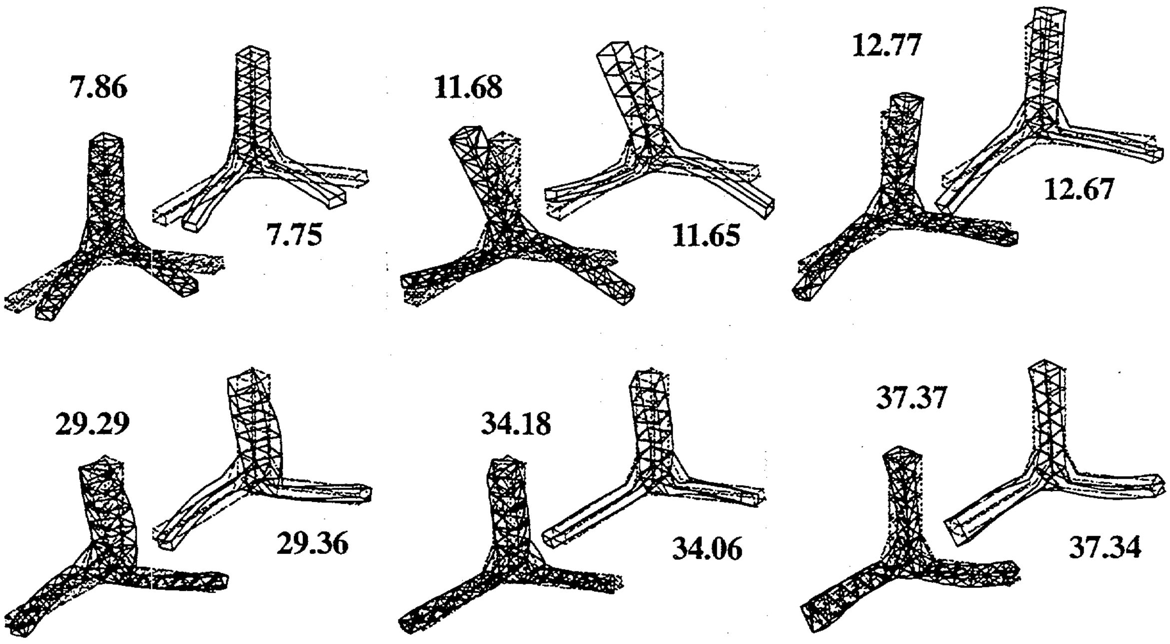

Figure 5: First Six Pairs of Test and Analysis Modes

FEM Frequency/#	Test Set 1 Frequency/#	Maximum FEM MAC	Maximum Test MAC	Frequency Error(%)
7.86/1	7.75/1	0.9984	0.9984	**1.42**(*)
11.68/2	11.65/2	0.9966	0.9966	**0.26**(*)
12.77/3	12.67/3	0.9971	0.9971	**0.79**(*)
29.29/4	29.36/4	0.9978	0.9978	**-0.24**(*)
34.18/5	34.06/5	0.9985	0.9985	**0.35**(*)
37.37/6	37.34/6	0.9950	0.9950	**0.08**(*)
42.43/7	42.25/7	0.9960	0.9960	**0.43**(*)
46.08/8	46.04/8	0.9955	0.9955	**0.09**(*)
-9-	48.06/9	—	0.7474	—
49.37/9	49.50/10	0.9890	0.9890	**-0.26**(*)
51.11/10	51.69/11	0.7696	0.7696	-1.12
53.80/11	53.00/12	0.9677	0.9677	**1.51**(*)
-11-	56.87/13	—	0.7714	—
56.72/12	58.01/14	0.9628	0.9628	**-2.22**(*)
58.58/13	-15-	0.6824	—	—
59.14/14	-14-	0.9441	—	—
60.26/15	60.04/15	0.9836	0.9836	**0.37**(*)

Table 4: MPI FEM/Test Set 1 Comparison

FEM Frequency/#	Test Set 2 Frequency/#	Maximum FEM MAC	Maximum Test MAC	Frequency Error(%)
-9-	48.06/9	—	0.7605	—
49.37/9	49.50/10	0.9890	0.9890	**-0.26**(*)
51.11/10	**50.63/11**	0.9364	0.9364	**0.95**(*)
-10-	51.69/12	—	0.7696	—
53.80/11	53.00/13	0.9677	0.9677	**1.51**(*)
-11-	**53.96/14**	—	0.9116	—
-11-	56.82/15	—	0.7658	—
-12-	**57.26/16**	—	0.7150	—
56.72/12	58.01/17	0.9628	0.9628	**-2.22**(*)
58.58/13	-18-	0.6824	—	—
59.14/14	-17-	0.9441	—	—
60.26/15	60.04/18	0.9836	0.9836	**0.37**(*)

Table 5: MPI FEM/Test Set 2 Comparison

yet to be resolved. These modes have been the object of some concern and an indirect result of the additional test procedures that have been performed indicate that they are associated with axial surge modes of the helical springs in the suspension system. This subject remains under investigation.

Final FEM Model

The final parametric version of the FEM was arrived at by reconciliation with a third, and final, test-derived model (*Test Set 3*). This was done by considering displacement degrees of freedom at the mid strut of each of two longest members, both of which had been observed to experience local strut modes in the frequency range of interest. Additionally, an analysis model reparameterization was performed to account for three long Bnut in assemblies these struts. These anomalous structural elements were used to tune the analysis local strut modes to those frequencies observed in each of the modal tests. These changes were incorporated in a frequency only parameter estimation session once again employing the code SSID. Final results are presented in Table 6.

As can be observed in the Table, the final FEM model reproduces the test modal frequencies, exclusive of the suspension system modes, quite well. FEM modes 11 and 12 correspond to the local strut modes. MAC values were not computed for these modes due to reference coordinate frame discrepancies.

The computational aspects of this problem should also be addressed. The final analysis model exists in the form of an `MSC/NASTRAN` bulk data deck. The a-set model size, output from `NASSID`, was 7896 degrees of freedom. Typical `SSID` runs required 4 Megawords of Cray Y/MP memory and took on the order of 70 seconds of cpu per estimation cycle. Approximately 25 cpu seconds of each estimation cycle was expended in the eigensolver, where 35 modes were computed.

To examine the progression from the initial pretest to the final FEM models graphically, acceleration FRF's from one of the test driving points to a displacement degree of freedom at the top of the tower (depicted graphically in Figure 6) are shown vs the measured FRF's for both models. Figure 6 contains this FRF information for the pre-test FEM, and Figure 7 for the final FEM. A modal frequency comparison is shown in Figure 8.

Second Configuration Results

Lastly, a second configuration was considered. This simple modification consisted of the MPI truss with 6kg of mass added at each of the four ball joints at the end of the metrology boom for a total of 24kg. A typical FRF, consistent with that of Figure 7, is presented in Figure 9. Agreement in those modes involving the system itself is shown to be quite good.

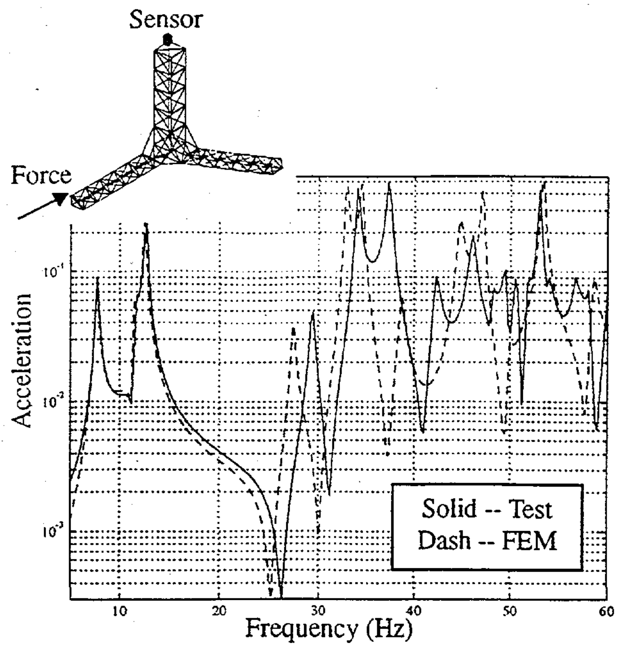

Figure 6: MPI Pre-Test FEM/Test FRF Comparison

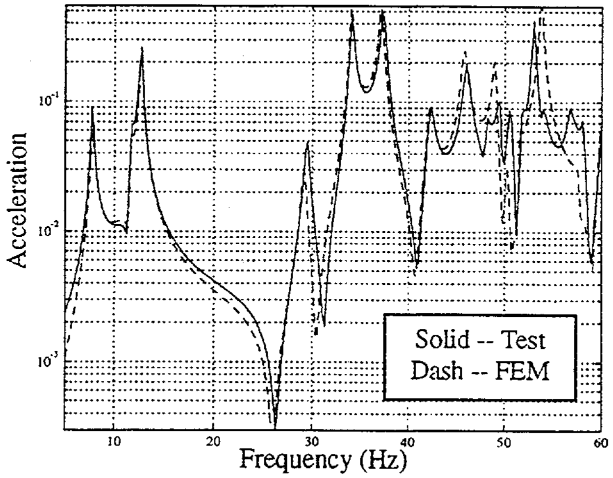

Figure 7: MPI Final FEM/Test FRF Comparison

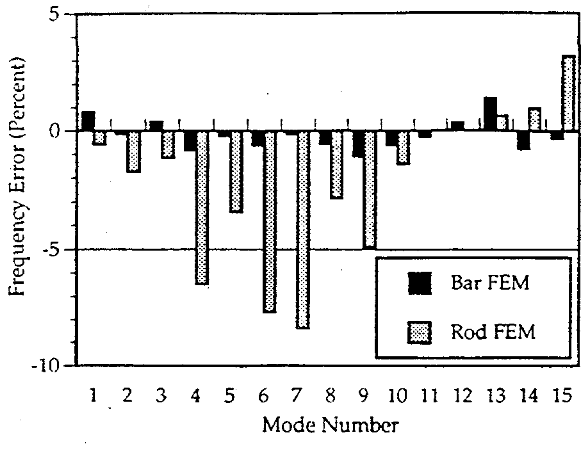

Figure 8: Pretest and Final Frequencies

FEM Frequency/#	Test Set 2 Frequency/#	Maximum FEM MAC	Maximum Test MAC	Frequency Error(%)
7.81/1	7.75/1	0.9984	0.9984	0.77(*)
11.64/2	11.65/2	0.9966	0.9966	0.09(*)
12.71/3	12.67/3	0.9973	0.9973	0.31(*)
29.12/4	29.36/4	0.9977	0.9977	-0.82(*)
33.98/5	34.06/5	0.9985	0.9985	-0.24(*)
37.11/6	37.34/6	0.9950	0.9950	-0.62(*)
42.20/7	42.25/7	0.9960	0.9960	-0.12(*)
45.78/8	46.04/8	0.9960	0.9960	-0.57(*)
-9-	48.09/9	—	0.7545	—
48.97/9	49.50/10	0.9902	0.9902	-1.14(*)
50.32/10	50.63/11	0.9328	0.9328	-.62(*)
51.56/11	51.69/12	—	—	-.25(*)
52.14/12	51.97/13	—	—	0.33(*)
53.74/13	53.00/14	0.9592	0.9592	1.38(*)
-13-	53.96/15	—	0.9515	—
-13-	56.82/16	—	0.7441	—
-14-	57.26/17	—	0.7813	—
57.57/14	58.01/18	0.9841	0.9841	-.76(*)
59.85/15	60.04/19	0.9886	0.9886	0.32(*)

Table 6: MPI FEM/Test Set 3 Comparison

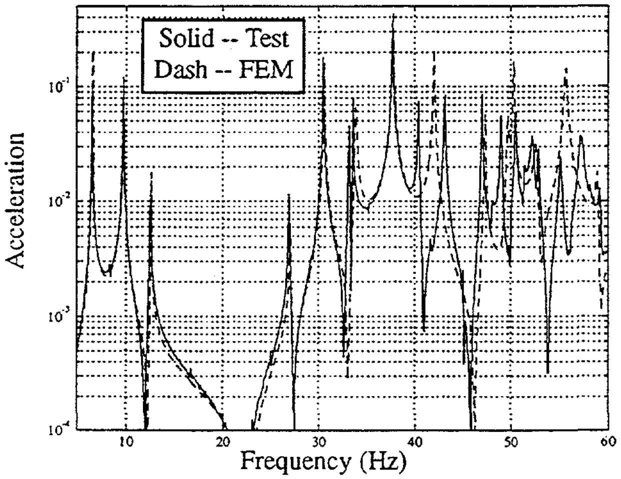

Figure 9: Second Configuration FRF Comparison

Concluding Remarks

The JPL MPI Testbed is an example of a repeatable, linear, high precision structure. As such, it affords an opportunity to refine analytical modeling and structural system identification procedures.

To facilitate an accurate structural characterization, the testing and the test-analysis reconciliation processes were separated into two stages; one each for the component and system levels. The first stage involved a component level test-analysis series which focused on two primary objectives: (1) the identification of an appropriate model form for the Node Ball/B-Nut/End Cap/Strut subsystem and (2) the estimation of a suitable set of "nominal" physical parameter values for this model. Modal test results were presented for the various configurations that were considered.

The test-analysis model reconciliation approach was based on estimating physical parameters in finite element models of each configuration. Such an approach provides an advantage over other methods by allowing results to be extrapolated to different configurations. For the current task, parameter estimation on the component level was performed via two techniques: a design sensitivity based approach using modal frequency information and a Bayesian approach which also incorporated mode shape data. A multiple configuration reconciliation approach resulted in an update of the model form and initial nominal physical parameter values for the structural subsystems which were to be incorporated into the system model.

The second stage concerned the identification of the full system model. Results of the system level modal test were presented. Structural system identification techniques were instrumental in refining the initial experimental modal model development. These developments underscore not only the essential need for communication between the analyst and the experimentalist, but also the equal footing on which both test and analysis rest in the system identification process. The full system model was produced by replicating the model form and parameter estimation results from the component level results. The initial system showed good agreement with modal test results for the system modes in the frequency range of interest. Further refinements to this initial model were achieved via Bayesian estimation on the full system model. Global and local modal behavior were reconciled.

The model was further evaluated by comparing the predictions for a simple structural modification to corresponding test results for the modified structure.

Finally, it is imperative that the analysis model capture the qualitative properties exhibited by the test article and that instrumentation planning be done accordingly to ensure these phenomena are measured in the test. For the current study, testing was done with the structure suspended via "soft" springs—an approximation to an analytical free-free condition. However, initial indications were that the structural dynamics of the suspension suspension system greatly affected the acquired test data. Future work at the system level will examine such issues in greater detail.

Further plans also include: (1) addressing the issue of when the system identification procedure should be considered complete. For example, our focus has been on reconciling modal models, but other characterizations of the response such as those described by FRF's and state-space models might be more suitable, (2) consideration of physical uncertainty in the prediction of system response, (3) local mode characterization and possible mitigation procedures, (4) additional structural modification verification, and (5) establishing metrics for selecting optimal excitation, measurement and suspension system locations.

Appendix A. On Bayesian Estimation

Our experiences with Bayesian estimation have prompted a closer look at the development of the procedure.

Bayesian estimation is a maximum likelihood, *a priori*, estimation technique. Consider the following relationship,

$$y = H(x) + \nu \tag{A.1}$$

where x is the "state" vector, in our case the set of parameters to be estimated; y is the "measurement" vector; and ν represents the assumption that this relation is corrupted with additive noise. We seek an probabilistically-based estimator for x that relies on an initial estimate, x_0. To do this, we will maximize the conditional probability density function $p(x \mid y)$. Applying Bayes' Rule yields

$$p(x \mid y) = \frac{p(y \mid x)p(x)}{p(y)} \tag{A.2}$$

But the denominator in Eq. A.2 is independent of x. Therefore, it can be restated as

$$p(x \mid y) = c_0 p(y \mid x)p(x) \tag{A.3}$$

Now consider the terms on the right hand side of Eq. A.3 which can be written as

$$p(y \mid x) = p(\nu \mid x) = p_\nu\Big(y - H(x)\Big) \tag{A.4}$$

Here we have exploited Eq. A.1 and the fact that the Jacobian of the transformation from y to ν is the identity matrix.

To make the procedure concrete, assumptions must be made on the probabilistic character of ν and x. Bayes estimation assumes that both of these quantities are Gaussian distributed. Specifically,

$$\begin{array}{rcl} \nu & \sim & \mathrm{N}(0, Q) \\ x & \sim & \mathrm{N}(x_0, P) \end{array} \tag{A.5}$$

where Q and P are the correlation matrices for the respective random vectors, and x_0 is the initial, *a priori*, estimate for the parameter vector. Thus, by Eq. A.5 and the additional assumption of statistical independence between the two random vectors,

$$\begin{aligned} p(x \mid y) = C \exp \Big\{ -\tfrac{1}{2} \Big[\Big(y - H(x)\Big)^T Q^{-1} \Big(y - H(x)\Big) \\ + \Big(x - x_0\Big)^T P^{-1} \Big(x - x_0\Big) \Big] \Big\} \end{aligned} \tag{A.6}$$

Finding the maximum of this last quantity is equivalent to finding the minimum of

$$\begin{aligned} q(x) = \Big(y - H(x)\Big)^T Q^{-1} \Big(y - H(x)\Big) \\ + \Big(x - x_0\Big)^T P^{-1} \Big(x - x_0\Big) \end{aligned} \tag{A.7}$$

Thus, the Bayesian estimate, $\hat{x}$, is that x which minimizes $q(x)$, often referred to as the *log likelihood function*, in Eq. A.7.

The scheme that we employ is iterative Bayes estimation. This approach is necessitated by the lack of a complete analytical description of the mapping between the measurement and state vectors (test eigendata and analysis physical parameters, respectively were employed in our study) and not by any linearity restriction imposed by the algorithm itself. Thus, sensitivity information is required only to approximate this mapping and does not imply that the procedure is gradient based in the classical sense of hill-climbing optimization approaches.

A recapitulation of the assumptions underlying the development of a Bayesian estimator: (1) a state-measurement relation that is corrupted with zero mean, Gaussian noise, (2) a state, x, that is Gaussian distributed about a mean that corresponds to the initial guess, x_0, and (3) the log likelihood function (Eq. A.7) that is unimodal and concentrated near this mode [13].

Acknowledgments

Thanks are extended to the remaining members of the JPL MPI team, Greg Neat, Lee Sword and Rob Calvet; and to members of the Sandia Modal Testing Department, Tom Carne, Randy Mayes and Larry Dorrell; whose work contributed this article. Also, a portion of this work was performed at Sandia National Laboratories under the support of the U.S. Department of Energy contract number DE-AC04-76DP00789. This support is greatly appreciated.

References

[1] M. Imregun and W. J. Visser. A Review of Model Updating Techniques. *Shock and Vibration Digest* **23**, 9–20 (1991).

[2] M. Baruch and I. Y. B. Itzhack. Optimal Weighted Orthogonalization of Measured Modes. *AIAA Journal* **16**, 346–351 (1978).

[3] A. Berman and F. S. Wei. Automated Dynamic Analytical Model Improvement. Technical Report CR-3452, NASA, 1981.

[4] G. C. Hart and D. R. Martinez. Improving Analytical Dynamic Models Using Frequency Response Data - Application. In *Proceedings of the 1982 Structures, Structural Dynamics and Materials Conference*, number Paper 82-0637, 1982.

[5] J. Isenberg. Progressing from Least Squares to Bayesian Estimation. Number Paper 79-A in DSC-16. ASME Winter Annual Meeting, 1979.

[6] B. R. Hanks. Dynamic Challenges for the 21st-Century Spacecraft. In *Proc. 61st Shock and Vibration Symposium*, volume 4, pages 3–18, 1990.

[7] R. A. Laskin and M. S. Martin. Control/Structure System Design of a Spaceborne Optical Interferometer. In *Proceedings of the AAS/AIAA Astrodynamics Specialist Conference*, 1989.

[8] J. A. Garba, B. K. Wada, and J. L. Fanson. Adaptive Structures for Precision Controlled Large Space Systems. *J. of Intell. Mater. Syst. and Struct.* **3**, 348–366 (1992).

[9] J. R. Red-Horse et al. System Identification of the JPL Micro-Precision Interferometer Truss: an Overview. In *Proc. of the 3rd Int'l Conf. on Adaptive Structures*, San Diego, CA, 1992.

[10] M. B. Levine-West. High Fidelity Predictive Models of Structures on Orbit. Technical Report JPL D-10113, Jet Propulsion Laboratory, California Institute of Technology, Pasadena, CA, 1992.

[11] J. D. Collins, G. C. Hart, T. K. Hasselman, and B. Kennedy. Statistical Identification of Structures. *AIAA Journal* **12** (1974).

[12] W. R. Witkowski and J. J. Allen. Approximation of Parameter Uncertainty in Nonlinear Optimization Schemes – Case Study of a Truss Structure. In *Proc. of Conference on Active Materials and Adaptive Structures*, 1991.

[13] A. H. Jazwinski. *Stochastic Processes and Filtering Theory.* Academic Press, New York, 1970.

[14] T. K. Hasselman and J. D. Chrostowski. SSID—A Computer Code For Structural System Identification. Technical Report TR-91-1134-1, Engineering Mechanics Associates, Inc., 3820 Del Amo Blvd, Suite 318, Torrance, CA, 1991.

[15] C. Flanigan. Users Guide for CORDS2. Technical report, Structural Dynamics Research Corporation, San Diego, California, 1988.

[16] G. W. Antal and L. Collins. Users Guide for NASSID 1.0: NASTRAN/SSID Software Interface. Technical report, Structural Dynamics Research Corporation, San Diego, California, 1992.

[17] T. G. Carne, R. L. Mayes, and M. B. Levine-West. A Modal Test Of a Space Truss for Structural Parameter Identification. In *Proceedings of the 11th Int Modal Analysis Conf*, 1993.

[18] J. L. Beck and L. S. Katafygiotis. Probabilistic System Identification and Health Monitoring of Structures. In *Proceedings of the 6th Specialty Conference on Probabilistic Mechanics and Structural and Geotechnical Reliability.* ASCE, 1992.

[19] N. G. Nalitolela, J. E. T. Penny, and M. I. Friswell. A Mass or Stiffness Addition Technique for Structural Parameter Updating. *Int J of Analytical and Experimental Modal Analysis* **7**, 157–168 (1992).

[20] D. J. Ewins. *Modal Testing: Theory and Practice.* John Wiley and Sons, 1984.

[21] D. O. Smallwood and D. L. Gregory. A Rectangular Plate is Proposed as an IES Modal Test Structure. In *Proceedings of the 4th IMAC*, 1986.

[22] F. Pechinsky et al. Understanding the Effects of DOF Contribution to Orthogonality Checks. In *Proc of the 11th IMAC*, 1993.

[23] P. Avitabile et al. Effects of DOF Selection on Orthogonality Using Reduced System Matrices. In *Proc of the 11th IMAC*, Kissimee, FL, 1993.

A COMPARATIVE STUDY OF METRICS FOR MODAL PRE-TEST SENSOR AND ACTUATOR SELECTION USING THE JPL/MPI TESTBED TRUSS

C.B. Larson*
Department of Aerospace Engineering,
Mechanics and Engineering Science
University of Florida

D.C. Zimmerman†
Department of Mechanical Engineering
University of Houston

E.L. Marek‡
Sandia National Laboratories
Albuquerque, New Mexico

ABSTRACT

A comparative study of several pre-modal-test planning techniques is presented using the Jet Propulsion Laboratories' Micro-Precision Interferometer testbed. Mode indicator functions calculated using a reduced finite element model of the structure are used in conjunction with a Genetic Algorithm to find location and orientation of two excitation sources in order to optimally excite a chosen range of finite element target modes during a modal test.

Effective independence, kinetic energy, and eigenvector product techniques are used with the structural finite element model to place a combination of sensors on the structure for the purpose of modal identification. The sensors are placed in two ways: independent sensor placement and triaxially constrained placement. A numerical simulation of the response of the structure is used to evaluate the effectiveness of each of the placement techniques to identify the target modal parameters of the structure. The effect of finite element model error on the various placement techniques is evaluated.

1. INTRODUCTION

Structural modal analysis has become an essential tool for the validation of finite element models (FEMs) and for the prediction of structural performance. The intended use of modal test data governs the pre-test planning associated with the modal test. The placement of actuators for excitation purposes and the placement of sensors for response observations, may well depend on whether the data will be used for modal parameter estimation, mode orthogonality for FEM correlation, identification of uncertain parameters in FEMs, or structural health monitoring.

In performing a modal test, constraints such as time, money, and spatial access govern the number, location, and orientation of the actuators and sensors that can be placed on the structure. With these constraints in mind, one wishes to find the optimal number, location, and orientation of sensors and actuators in order to obtain the most information from a modal test.

Researchers have developed several techniques which utilize the information contained within the baseline FEM to optimally place sensors and actuators. A thorough literature review on the topic of sensor placement is given in a paper by Kammer [1]. Because these placement techniques are dependent on the FEM of the structure, it is of some concern how FE modeling error affects the placement strategies.

The sensor and excitation placement techniques, which are evaluated in this paper are discussed in Section 2. In Section 3, the characteristics of the Micro-Precision Interferometer (MPI) structure and its corresponding FEM are given. In Sections 4 and 5 the actuator and sensor placements of the various techniques on the MPI structure are discussed. In Section 6, the effect that FEM error has on the various placement techniques is explored. The computational cost of the placement techniques is discussed in Section 7.

2. ALGORITHM DESCRIPTIONS

2.1 Effective Independence (EI)

Effective independence is a technique developed to place sensors for the purpose of obtaining structural information for FEM verification of large space structures [1]. It follows from the work done by Shah and Udwadia [2] and Udwadia and Garba [3]. The sensor locations are chosen such that the trace and determinant of the Fisher information matrix (corresponding to the target modal partitions) are maximized and the condition number minimized. By maximizing the determinant of the Fisher information matrix, the covariance matrix of the estimate error is minimized, thus giving the best estimate of the structural response. A reduced sensor set is obtained in an iterative fashion from an initial candidate set by removing sensors from those degrees of freedom (DOFs) (i.e. removing rows from the Fisher information matrix) which contribute least to the linear independence of the target modes.

---

*NASA/Florida Space Grant Fellow, student member AIAA.
†Associate Professor, Member AIAA.
‡Member AIAA.

Copyright ©1994 by C.B. Larson, D.C. Zimmerman, E.L. Marek
Published by the American Institute of
Aeronautics and Astronautics with permission.

2.2 Kinetic Energy (KE)

The use of kinetic energy for optimal sensor placement as well as target mode identification has been discussed in several papers [1,4]. The modal kinetic energy is calculated using the FEM mass matrix and target modes. It is assumed that by placing the sensors at points of maximum kinetic energy, the sensors will have the maximum observability of the structural parameters of interest. Degrees of freedom with the maximum kinetic energy for a mode or for modes of interest are chosen as sensor or excitation locations.

The kinetic energy objective function precludes placing any sensors or actuators at nodal points since there is no motion and zero kinetic energy at these points. This could be a limiting factor in pre-test planning. To combat this problem, sensors can also be placed using maximum average kinetic energy (AKE) technique. A sensor is placed at a DOF with a maximum average kinetic energy over a range of modes of interest. In using an average kinetic energy, a DOF is not necessarily excluded if it is a node point of a particular mode.

In addition, it should be noted that the mass weighting inherent to the kinetic energy and average kinetic energy approaches causes the sensor or excitation placement to become dependent on the FE discretization of the structure. There is an inherent bias against the placement of sensors in areas of the structure in which a fine mesh size (and thus typically small mass) is used. Since these techniques are dependent on the mass distribution of the FEM, they may also be affected by FEM reduction.

2.3 Eigenvector Product (EVP)

This technique uses modal products from the reduced FEM eigenvectors (or mode shapes) to identify possible locations for sensors or excitation. By choosing a frequency range of interest and the corresponding FEM eigenvectors in that range, a product for the i^{th} DOF is calculated by multiplying the eigenvector components over the mode range chosen. A maximum absolute value of this product corresponds to a candidate location of sensing or excitation [5]. This technique also precludes the placement of sensors at nodal points which result in zero eigenvector products. If this presents a problem for a given test case, the eigenvector product can be replaced by an absolute value eigenvector sum, over the FE target modes of interest.

2.4 Mode Indicator Function (MIF)

The mode indicator function was first developed to detect the presence of real normal modes in sine dwell modal testing [6,7]. This function also serves as a useful metric for pre-test analysis. While it is somewhat useful for assessing the efficacy of sensor layout, its true utility lies in assessing the effectiveness of a particular input in exciting the system modes. The MIF is nearly 1.0 except near a normal mode, at which point it drops off considerably since the frequency response becomes mostly imaginary at that point. In pre-test planning, an excitation is desired which exhibits this drop in the MIF at each mode of interest, indicating that the mode is well excited.

In this work a Genetic Algorithm (GA) is used as the optimization technique in conjunction with the MIF to optimally select location and orientation of excitation devices on the MPI structure. Genetic Algorithms, as introduced by Holland [8], are a form of directed random search. The form of direction is based on Darwin's "survival of the fittest" theories. In GAs, a finite number of candidate solutions or designs are randomly or heuristically generated to create an initial population of designs. This initial population is then allowed to evolve over generations to produce new and potentially better designs. The basic conjecture behind GAs is that evolution is the best compromise between determinism and chance. However, it should be noted that they are not as efficient as nonlinear optimization techniques over the class of problems which are ideally suited for nonlinear optimization; namely continuous design variables with a continuous, differentiable, unimodal design space. Genetic Algorithms also have the capability to solve continuous, discrete and continuous/discrete optimization problems. For the MPI example used in this paper, the node point locations of excitations being sought are represented by discrete design variables, and the orientations of these excitations are represented by continuous design variables. A thorough overview of the GA used in this work is presented in [9].

3. MPI STRUCTURE

The JPL/MPI, shown pictorially in Fig. 3.1, is a testbed that has been built in order to study structural control systems in the development of space interferometers. Modal tests were performed on the MPI structure by two independent groups (Sandia National Laboratories and the Jet Propulsion Laboratories [10,11,12]).

The FEM used to evaluate the placement techniques in the current work was obtained from Sandia National Laboratories [10]. The model used is a 240 DOF Guyan-reduced FEM which has been updated using the data obtained from the modal test of the structure. The 240 DOFs correspond to three DOFs (x,y,z) at each of the 80 node balls. The frequencies from the Guyan-reduced FEM corresponding to the first 12 non-rigid-body modes which will be targeted in the current study are given in Table 3.1 and are compared to actual frequencies obtained during the modal test.

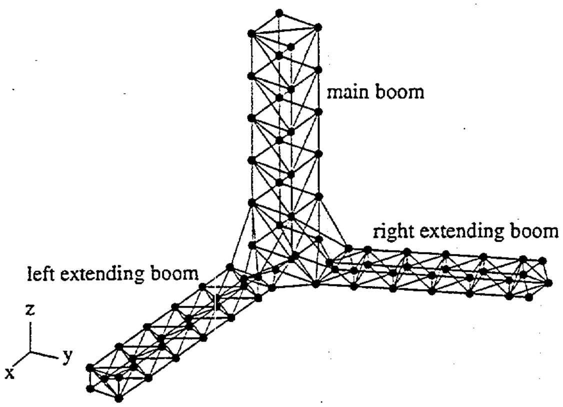

Figure 3.1: JPL/MPI testbed structure

Mode	Frequency(Hz) FEM	Frequency(Hz) modal test
1	7.82	7.75
2	11.66	11.65
3	12.75	12.67
4	29.52	29.36
5	34.45	34.06
6	37.76	37.34
7	42.81	42.25
8	47.30	46.04
9	51.14	50.69
10	52.36	53.00
11	55.41	56.82
12	61.40	60.04

Table 3.1: Reduced MPI FEM frequencies compared with MPI modal test frequencies

4. ACTUATOR PLACEMENT

During the original modal test of the MPI structure two excitation sources were used as pictured in the top portion of Fig. 4.1. The lower portion of this figure is the excitation configuration that was obtained by optimizing the MIFs using a GA. Both the original and the GA/MIF excitation locations have an exciter on the two extending booms although they are oriented differently. The GA/MIF set-up moves the excitation of the right extending boom to an interior point in comparison to the original configuration. Figure 4.2 gives typical frequency responses for the excitations shown in Fig. 4.1. The responses are measured at the sensor location shown in Fig. 4.1 in the y-directions.

The excitation devices placed by the GA were selected to minimize an objective function which was dependent on the MIF of each of the two excitation locations. The MIF will be nearly 1.0 except near normal modes, at which point it drops off considerably. This drop-off indicates that the mode is well excited. Therefore, it is desirable to find two excitation sources (location and orientation) which exhibit a sharp drop at all of the normal frequencies.

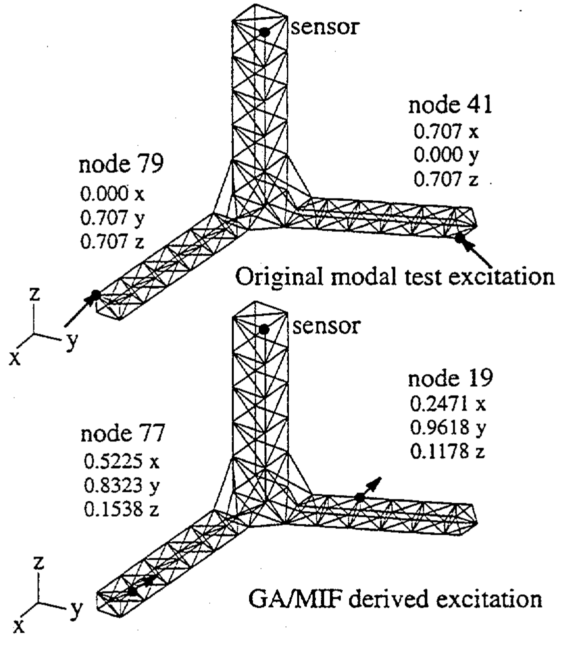

Figure 4.1: Excitation placement on MPI structure

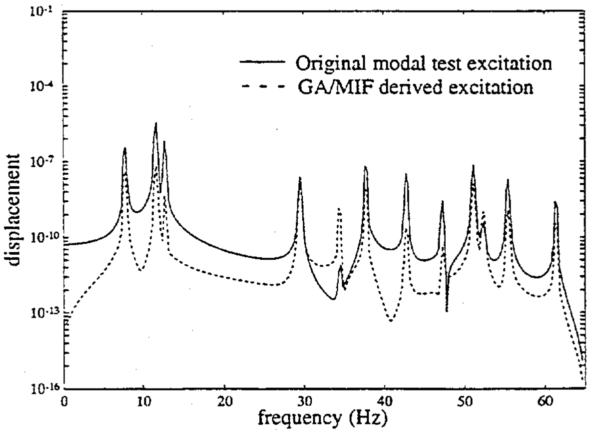

Figure 4.2: Typical frequency response for MPI structure

The GA objective function was derived such that each excitation need not exhibit a sharp drop-off for all modes as long as the the union of the two MIFs exhibited a large drop-off for each frequency. For this example, there were 12 drop-off values for each of the two excitations being evaluated (total of 24), and the maximum drop-off for each frequency was selected for objective function evaluation. Each MIF drop-off value was then scaled according to its location above a target minimum value. For this particular example the target minimum MIF value was set to 0.1. Any drop-off value at or below the target minimum (0.0 to 0.1) contributed nothing to the objective function. Any drop-off value above this target minimum (>0.1 to 1.0) was given an objective function value exponentially proportional to the distance above the target minimum. The final objective function was calculated by summing up the scaled contribution of each drop-off value over the 12 frequencies of interest. The GA was then used to minimize the objective function.

The GA was supplied with a randomly generated initial population of 20 members. Each member in the population was made up of two discrete and six continuous design variables. The 2 discrete design variables were the possible node point locations (ranging from 1 to 80), and the 6 continuous design variable were the direction cosines (ranging from +1 to −1) of the two exciters being sought. The population evolved over 40 generations, and the most fit member of the final population was chosen as the excitation locations. Table 4.1 list each of the excitations' corresponding MIF drop-off values and objective function values. The MIFs for the original excitations used during the modal test and for the GA/MIF located excitations are shown in Fig. 4.3.

	Original		**GA/MIF**	
MODE	**41**	**79**	**19**	**77**
1	0.5978	0.5978	0.5980	**0.5977**
2	0.6714	0.7216	**0.6713**	0.6714
3	0.3572	**0.3569**	0.3572	0.5095
4	0.4414	0.4795	0.4368	**0.4344**
5	0.3280	0.3275	**0.3252**	0.3331
6	0.4863	0.2043	0.7184	**0.2031**
7	**0.2184**	0.2198	0.7366	0.2289
8	**0.1266**	0.3553	0.1325	0.3524
9	0.1826	0.7861	**0.1231**	0.7494
10	0.7256	0.8948	0.8079	**0.1814**
11	0.4184	**0.1331**	0.3169	0.1499
12	0.1012	0.8113	**0.0761**	0.4436
Objective Function	1023.09		500.57	

Table 4.1: Original and GA/MIF excitation locations MIF values

The GA excitations' MIFs exhibit a sharper drop-off than the original excitations' MIFs for 8 of the 12 target modes as can be seen in Fig. 4.3 and Table 4.1. The sharpest drop-off value for each of the modes is highlighted in bold, and the mode numbers whose sharpest drop-off values are those for the GA/MIF derived excitations are also highlighted in the table. An improvement in the drop-off of the GA/MIF excitation over the original excitation can especially be seen for the tenth mode. The last row of Table 4.1 gives the objective function value for the original and GA/MIF derived excitation forces. As previously discussed, the objective function is based on the sharpest MIF drop-off values of the excitation pair being evaluated, hence there is one objective function value for each evaluated excitation set. The large difference in objective function value can be contributed mostly to the exponential penalization associated with the drop-off value at mode ten.

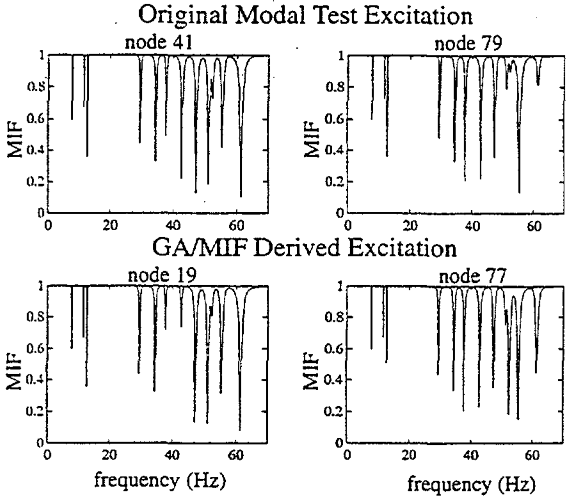

Figure 4.3: Mode Indicator Functions for MPI structure

Numerical simulations of the MPI structural response to simultaneous impulses applied at the two exciter set locations were calculated within the MATLAB environment. Five percent noise was added to the simulated time responses of the structure. These time responses were used along with the Eigensystem Realization Algorithm (ERA) to identify the twelve target mode shapes and frequencies [13]. The evaluation of the success of ERA to identify the frequencies and mode shapes was based on a frequency percent difference comparison between identified and FE frequencies and on a cross-orthogonality check between FE and identified mode shapes using an exactly reduced mass matrix. The reduction is exact in the sense that the frequencies and mode shapes of the reduced system match exactly their counterparts in the unreduced model [14].

It is interesting to note that when ERA was used to identify system mode shapes and frequencies, it missed the fifth and tenth frequencies and mode shapes when the original 41/79 DOF excitation locations were used to numerically simulate structural excitation. To illustrate this, the cross-orthogonality between FEM and ERA identified mode shapes was calculated, and is pictured in Fig. 4.4. For this example, the 240 DOF simulated response was partitioned to the sensor configuration obtained using the EI technique as discussed in the following section. These poor cross-orthogonality results are corroborated by the frequency response function shown in Fig. 4.2 in which poor excitation can be seen for modes 5 and 10. The GA derived excitation resulted in a successful ERA identification of all 12 mode shapes and frequencies of the original FEM.

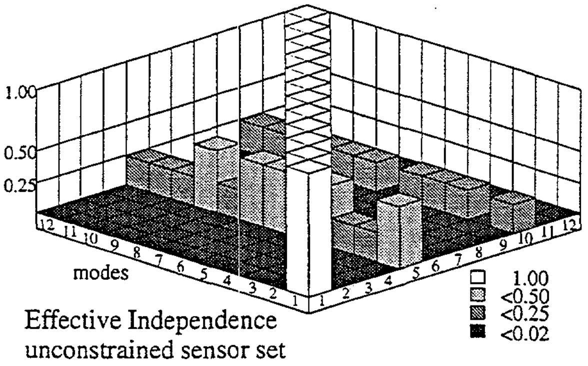

Figure 4.4: Cross-orthogonality between FE modes and identified modes

5. SENSOR PLACEMENT

Four sensor selection techniques, effective independence, kinetic energy, average kinetic energy, and eigenvector product, were used to place sensors on the MPI structure. These techniques were previously evaluated for sensor placement using the NASA eight-bay testbed [15]. In that study, all four techniques performed equally well. This could be due to two reasons: (i) the structure lacked significant dynamic complexity required to distinguish between the methods or (ii) the methods were actually so similar that they led to similar results regardless of structural dynamics. Thus, one purpose of this study is to again evaluate the four techniques on a more complex dynamic system. The second purpose is to investigate the suitability of the techniques when the sensors are constrained to be placed in a triaxial configuration.

Eighteen sensors were placed in two different studies using the four techniques in order to best identify the 12 target FEM mode shapes and frequencies. First, the techniques were used to choose 18 of the 240 DOFs as sensor locations. In the second study, the techniques were constrained to choose 18 triaxially constrained sensors (i.e. 6 triax-sensor sets). The excitations selected using the GA discussed in the previous section were used to excite the MPI structure numerically in order to test the various sensor configurations.

5.1 Unconstrained Sensor Placement

The first placement study evaluated the four techniques' placement of 18 sensors on the MPI structure at any of the 240 DOFs (x,y,z of the 80 node balls). The first 12 flexible modes of vibration were chosen as the target modes for each technique. In the cases of KE, AKE, and EVP techniques, DOFs were chosen for which these values were a maximum over the modes of interest. For the EI technique, those DOFs which contributed least to the linear independence of the target modes were removed in an iterative fashion, starting with 240 DOFs and finishing with 18 DOFs . The locations of the sensors obtained using each of the techniques are pictured in Fig. 5.1.1

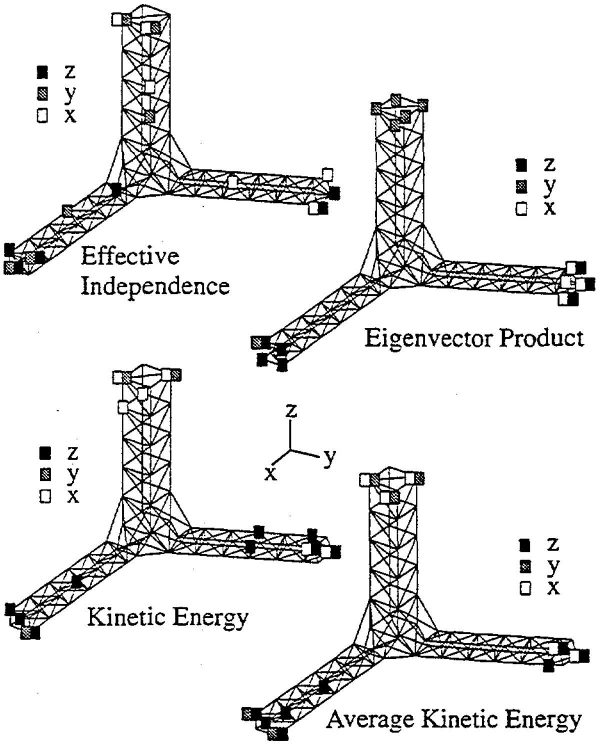

Figure 5.1.1: Unconstrained Sensor Sets

All of the techniques evaluated placed a majority of the 18 sensors at the ends of the three booms. In addition all of the techniques placed sensors in the two DOFs for each boom which exhibited the greatest range of motion (i.e. xy for the primary boom, xz for the extending right boom and yz for the extending left boom). The EVP technique clustered all 18 sensors at the boom tips and the AKE techniques clustered 17 of the 18 sensors at the boom tips, with one sensor being placed near the mid-span of an extending boom. The KE technique placed 15 sensors at the boom tips with 3 sensors near the mid-span of the two extending booms. The EI technique placed 13 sensor at the boom tips and at least one sensor near the mid-span of the main and extending booms.

Of the twelve target modes shapes, modes 2 through 11 exhibit a bending mode similar to that of second-mode-cantilevered-beam bending in at least one of the main or extending booms. The two extending booms exhibit second-mode bending most clearly, but the main boom also exhibits it for some of the twelve modes. The sensor configurations chosen by the EI and KE techniques are particularly suited to capture this second-bending-mode shape due to their placement of some sensors at mid-spans of the three booms.

The FEM of the MPI structure was used with MATLAB to simulate a time response of the structure to an impact applied at the GA/MIF chosen excitation locations for all 240 DOFs. Five percent uncorrelated noise was added to the time response. The noisy response was then partitioned to each of the four sensor sets and was sent to ERA for mode shape and frequency identification.

All the techniques resulted in percent frequency difference between FEM and identified frequencies of much less than 1% (well within industry accepted standards [16]). Cross-orthogonalities between FEM and identified mode shapes were calculated for each of the techniques and are pictured in Figs. 5.1.2-5.1.5. In order to calculate the cross-orthogonalities, the 240 DOF FE mass matrix was reduced to 12 DOFs using exact reduction. For this size model, exact reduction was computationally acceptable, therefore, it was used to get the best cross-orthogonality comparison.

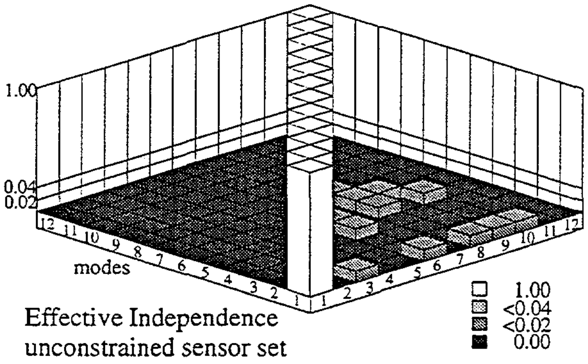

Figure 5.1.2: Cross-orthogonality between FE modes and identified modes

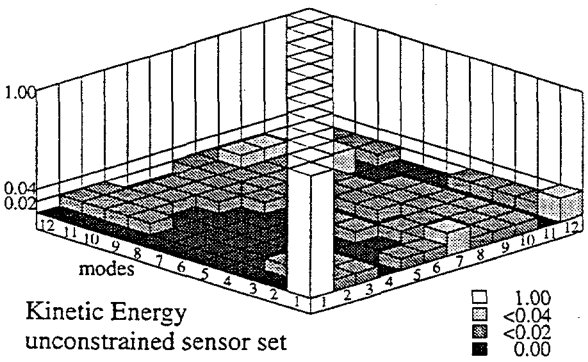

Figure 5.1.3: Cross-orthogonality between FE modes and identified modes

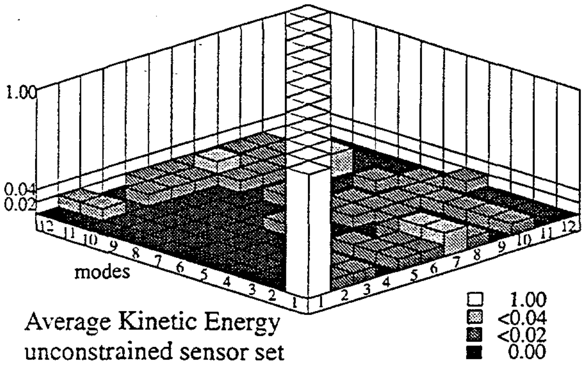

Figure 5.1.4: Cross-orthogonality between FE modes and identified modes

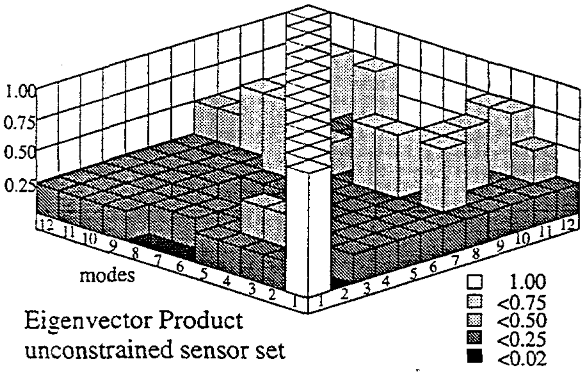

Figure 5.1.5: Cross-orthogonality between FE modes and identified modes

All of the off-diagonal elements of the cross-orthogonality matrix for the EI technique are within the industry accepted standards of <0.02 for primary modes [16]. This can be seen graphically in Fig. 5.1.2. For the KE and AKE techniques, almost all of the off-diagonal elements are <0.02. Some of the entries are greater than 0.02 but less than 0.04. These entries lie within the industry standard for secondary modes (<0.1). The cross-orthogonality for the EVP technique, as seen in Fig. 5.1.5, was poor for all target modes. The cross-orthogonality of the EVP technique was evaluated with no noise, 1%, 2%, and 5% noise added to the time response. Of the four time responses evaluated, only the response with no noise gave acceptable cross-orthogonality values. Based on these calculation, the EVP technique was unsuccessful in finding an acceptable sensor set.

5.2 Triaxially Constrained Sensor Placement

The four sensor placement techniques were modified to place 6 triaxially constrained sensor sets (18 total sensors) at any of the 80 node balls of the MPI structure. For the cases of KE, AKE, and EVP techniques, triax-sensor locations were chosen by taking the sum of the KE, AKE, and EVP values for each DOF at a particular node point of the structure. Those node points with maximum KE, AKE, and EVP sums were chosen as triax locations. The triaxial constraint was used differently with the EI placement technique. As the algorithm iterated through the 240 DOFs, the three DOFs (corresponding to a node point) which contributed least to the linear independence of the target modes were eliminated over each iteration. The EI value for each node was calculated as a sum of the EI of each DOF of that node. If, however, one of the DOFs for a particular node had an EI value of 1.0 (meaning that that DOF was essential to the linear independence of the target modes), that node point was retained, regardless of the ranking of its node point EI sum rating compared to the other node points. The resulting 6 triax-sensor sets placed using the four placement techniques are pictured in Fig. 5.2.1.

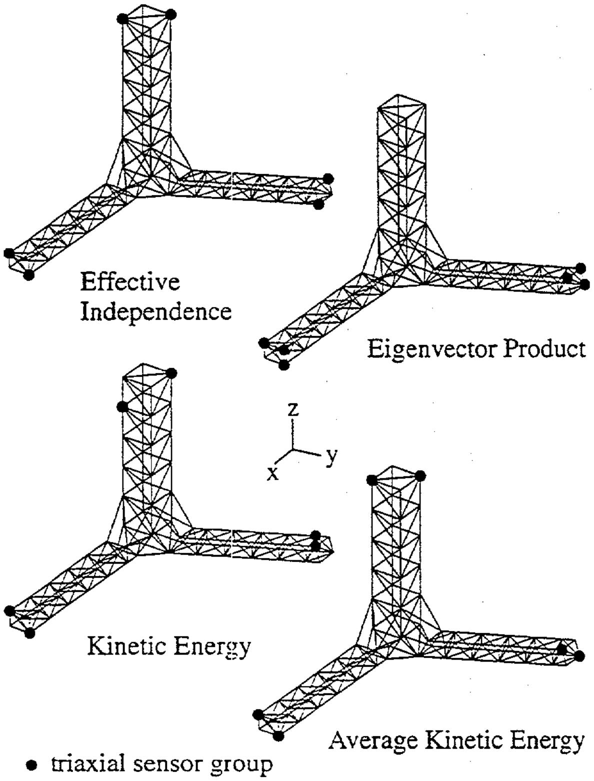

Figure 5.2.1: Triaxially Constrained Sensor Sets

As can be seen in Fig. 5.2.1, the EI, KE, and AKE techniques grouped two sensor sets at or near the end of each boom. However, the EVP technique placed 3 triax-sets at the ends of only two of the booms. It should be noted that if the placement task were extended to placing 7 triax-sets, the seventh set would be placed at the end of the main boom using the EVP technique.

The time response of the MPI structure used in Section 5.1 was partitioned to those DOFs corresponding to the six triax sensor locations chosen by the four placement techniques. The partitioned numerical data with noise added was sent to ERA in order to evaluate the effectiveness of each of the triax-sensor sets in identifying the system mode shapes and frequencies.

All the techniques resulted in percent frequency difference between FEM and identified frequencies of much less than 1% (well within industry accepted standards). The cross-orthogonality calculations between the FEM target modes and the ERA identified modes were performed using an exactly reduced mass matrix as in the previous section, and are shown in Figures 5.2.2 - 5.2.5.

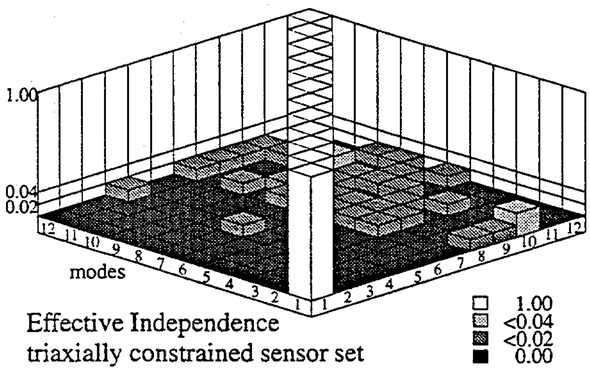

Figure 5.2.2: Cross-orthogonality between FE modes and identified modes

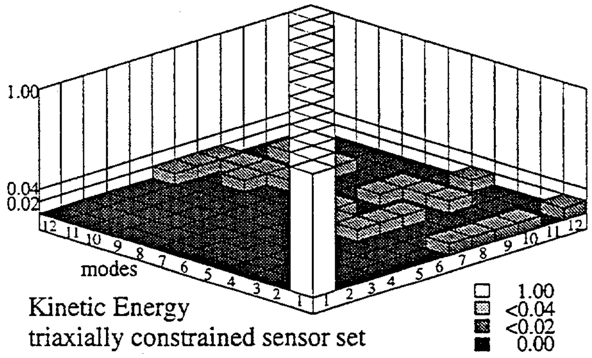

Figure 5.2.3: Cross-orthogonality between FE modes and identified modes

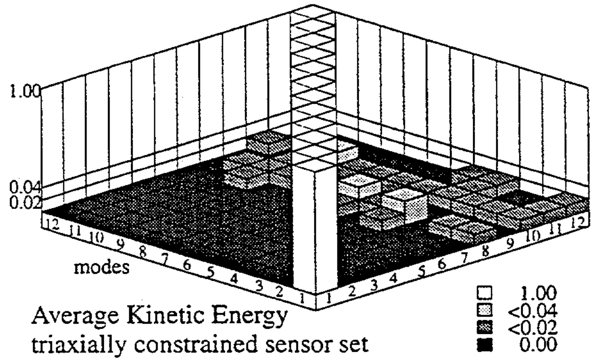

Figure 5.2.4: Cross-orthogonality between FE modes and identified modes

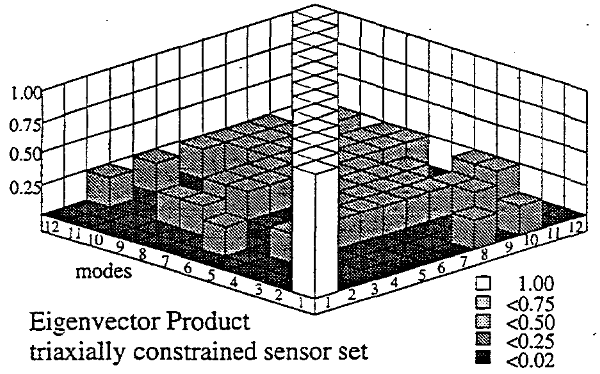

Figure 5.2.5: Cross-orthogonality between FE modes and identified modes

All of the off-diagonal cross-orthogonality values for the KE techniques, shown in Fig. 5.2.3, were within the industry standard of <0.02 for off-diagonal elements for primary modes. The EI and AKE techniques resulted in cross-orthogonalities which were within this standard for most of the modes, but which were slightly above the off-diagonal standard for a few modes as can be seen in Figs. 5.2.2 and 5.2.4. These values were however within the industry standard of <0.1 for secondary modes. The EVP technique resulted in poor off-diagonal cross-orthogonality values for all modes as can be seen in Fig. 5.2.5.

5.3 Unconstrained vs. Triaxially-Constrained Sensor Sets

Based on the cross-orthogonalities and frequency differences between FE and identified mode shapes and frequencies the EI, KE, and AKE techniques located sensor sets for the unconstrained and constrained examples which were reasonably successful in identifying the target mode set. For the unconstrained sensor set, the EI sensor set resulted in identified modes with the best cross-orthogonality with the FE target modes. However, for the triaxially-constrained example, the KE sensor set resulted in identified modes with the best cross-orthogonality with FE target modes. In both constrained and unconstrained cases the EVP technique resulted in identified modes with poor cross-orthogonalities with FE mode shapes.

6. EFFECT OF MODEL ERROR

In order to investigate the effect that model error has on the various placement techniques, error was added to the original Guyan-reduced FEM of the MPI structure. Specifically, 1/3 of the struts' cross-sectional areas were decreased by 20%, 1/3 of the struts' cross-sectional areas were increased by 20%, and the remaining 1/3 of the struts were unchanged.

The resulting differences in pre-corrupted and post-corrupted model frequencies and mode shapes are listed in Table 6.1. The second column represents the percent differences in the frequencies of the two models. The third column represents the root mean squared (RMS) values of the absolute differences in the mode shapes of the two models. The differences between the pre- and post-corrupted model mode shapes are shown pictorially in Fig. 6.1. The true modes are plotted along the x-axis and the corrupted modes are plotted along the y-axis.

MODE	Frequency % difference	Mode Shape RMS values
1	3.15	0.90 e–3
2	3.23	5.20 e–3
3	2.01	5.20 e–3
4	3.27	4.70 e–3
5	1.27	5.60 e–3
6	1.27	10.9 e–3
7	1.76	13.9 e–3
8	0.45	11.8 e–3
9	2.23	9.00 e–3
10	3.47	10.4 e –3
11	0.12	14.7 e–3
12	1.96	14.1 e–3

Table 6.1: Difference between pre and post corrupted model frequencies and mode shapes

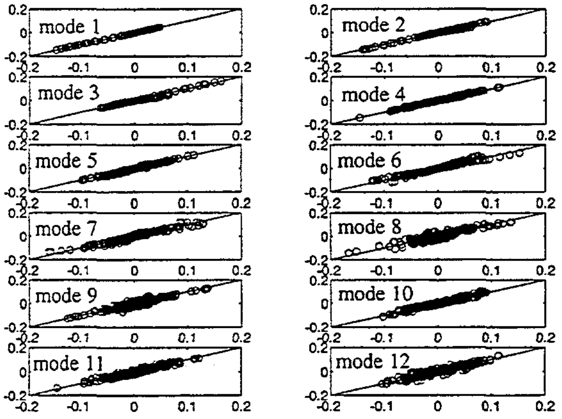

Figure 6.1: True mode shapes vs. corrupted mode shapes

6.1 Excitation Placement

Once error was introduced into the MPI FEM, the excitation placement technique using the MIFs and the GA was run. The twelve error-target modes were used to calculate the MIFs for the objective function evaluation in the GA. The GA setup was the same as that run for the model with no errors added. The GA/MIF derived excitations for the model with error and without error added (as obtained in Section 4) are pictured in Figure 6.1.1. The node points chosen as the excitation locations were very similar for the two cases; only node 77 switched to node 76 when model error was added. The directions for all of the exciters were changed when model error was added.

The resulting frequency response for the corrupted GA/MIF excitation as compared to the uncorrupted GA/MIF excitation is pictured in Fig. 6.1.2. The uncorrupted FEM was used to simulate the response of the MPI structure to impacts applied at the two GA/MIF exciter set locations shown in Fig. 6.1.1; the responses were measured at the sensor shown in Fig. 6.1.1 in the y-direction. As can be seen from Fig. 6.1.2, the excitation locations and orientations obtained using the model with error appeared to be successful in exciting all of the target modes.

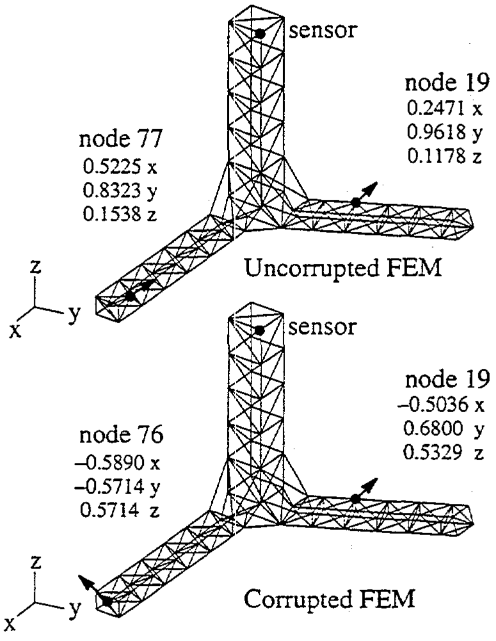

Figure 6.1.1: GA/MIF derived excitation locations

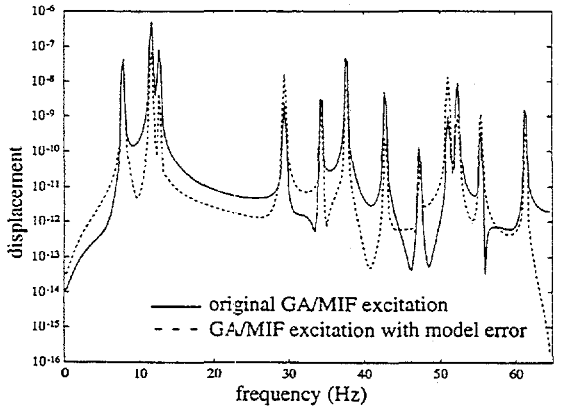

Figure 6.1.2: Frequency response using corrupted and uncorrupted GA/MIF excitations

In order to evaluate the excitation obtained using the corrupted FEM, the time response of the MPI structure to impacts at the excitations obtained with the corrupted FEM was numerically simulated using the original uncorrupted model. This time response was then partitioned to the uncorrupted unconstrained sensor sets (discussed in Section 5.1) and was sent to ERA for identification. As in the case of the uncorrupted model excitations, the EI, KE, and AKE techniques were successful in identifying the target frequencies and mode shapes based on percent difference and cross-orthogonality calculations. Based on these results, the error added to the FEM had little to no effect on the excitation placement configurations' success in exciting the "true" target mode shapes of the structure.

6.2 Sensor Placement

Both the unconstrained and triaxially constrained sensor placement problems were evaluated after error was added to the FEM using the four placement techniques previously discussed. The changes in sensor set configurations for the unconstrained and constrained sets are shown pictorially in Fig. 6.2.1 and Fig. 6.2.2. The original sensors placed using the uncorrupted FEM are represented by the boxes. Any sensors that were removed from the original sensor set after model error was introduced are represented by circles and any sensors that were added to the original set after model error was introduced are represented by triangles.

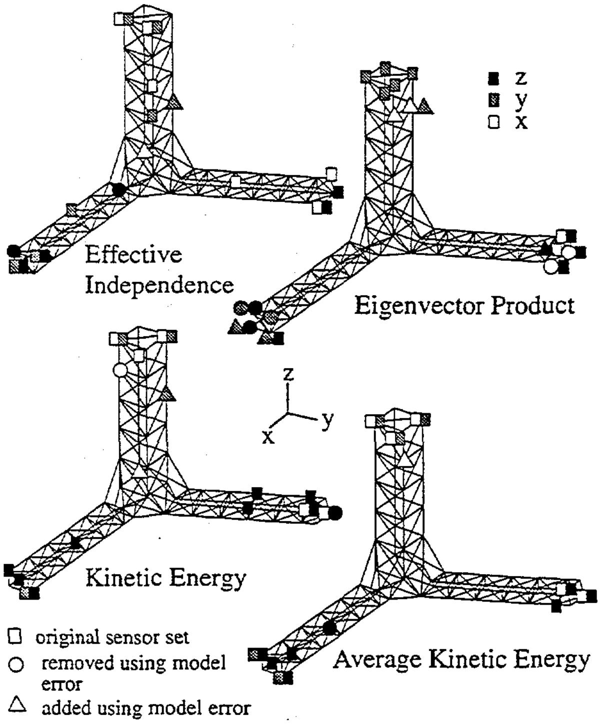

Figure 6.2.1: Model error effect on unconstrained sensor sets

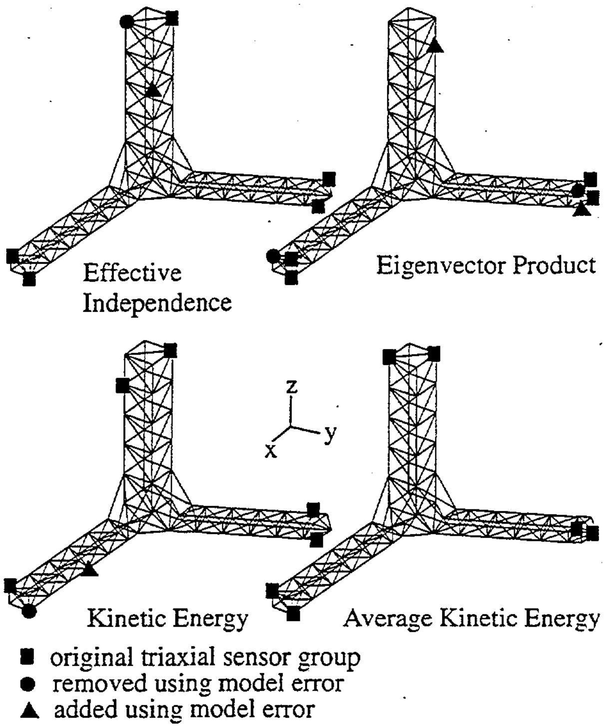

Figure 6.2.2: Model error effect on constrained sensor sets

The total numbers of sensors that changed for the unconstrained sets and the total numbers of triax-sets that changed for the constrained sets after model error was introduced are listed in Table 6.2.1. The AKE technique was affected least by the model error, the EI and KE techniques were affected only slightly by the model error, and the EVP technique was affected the most by model error for both the constrained and unconstrained sensor configurations.

For the unconstrained sensor sets, the general distribution of the sensors was mostly maintained after model error was added. All four techniques resulted in sensor sets which were changed by at least one sensor when model error was added. In each of these cases at least one sensor was added to the main boom of the truss as shown in Fig. 6.2.1.

For the constrained sensor sets, three of the four placement techniques resulted in a changed sensor set after model error was added. The EI technique moved one triax-set from the main boom tip to mid-boom, the KE technique moved one triax-set from the left extending boom tip to mid-extending-boom, and the EVP technique moved a triax-set from the left extending boom to the main boom.

The original uncorrupted FEM response to the GA/MIF derived excitation was used to evaluate the new sensor sets obtained with the corrupted FEM. The time response discussed in Section 5 was partitioned to the new sensor configurations and ERA was used to identify mode shapes and frequencies. Both the unconstrained and constrained sensor sets obtained using the corrupted FEM were successful in identifying the target frequencies within 1%, for all four techniques (EI, KE, AKE, and EVP) evaluated. The resulting cross-orthogonalities between identified (using error sensor sets) and original FEM mode shapes were calculated and are pictured in Fig. 6.2.3 and Fig. 6.2.4.

Sensor Set	EI	KE	AKE	EVP
constrained	2 of 18	2 of 18	1 of 18	6 of 18
unconstrained	1 of 6	1 of 6	0 of 6	2 of 6

Table 6.2.1: Number of sensors or triax sets that change when model error is added

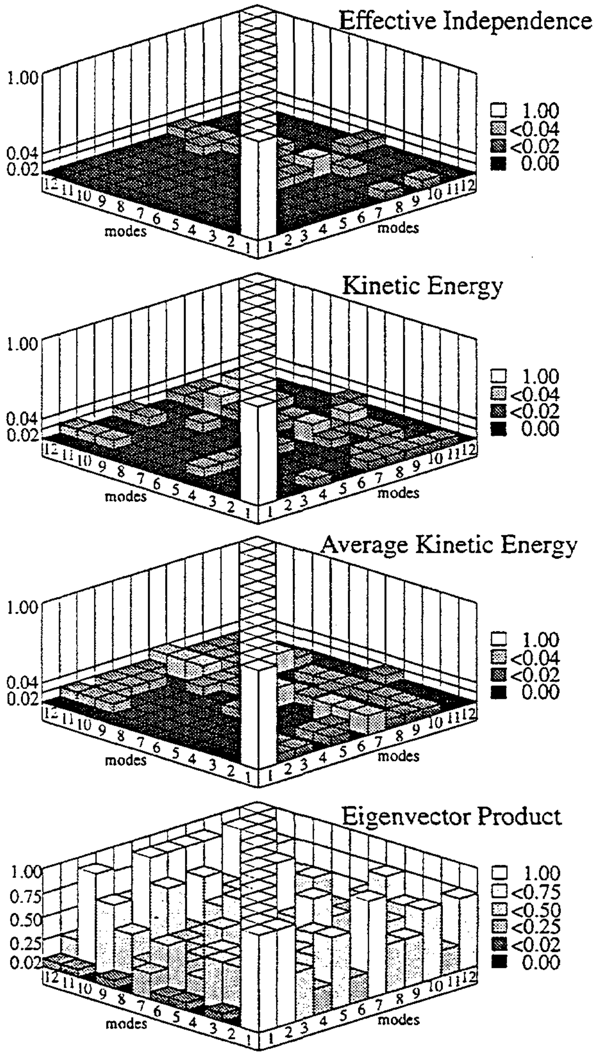

Figure 6.2.3: Cross-orthogonality between identified and FEM modes (unconstrained)

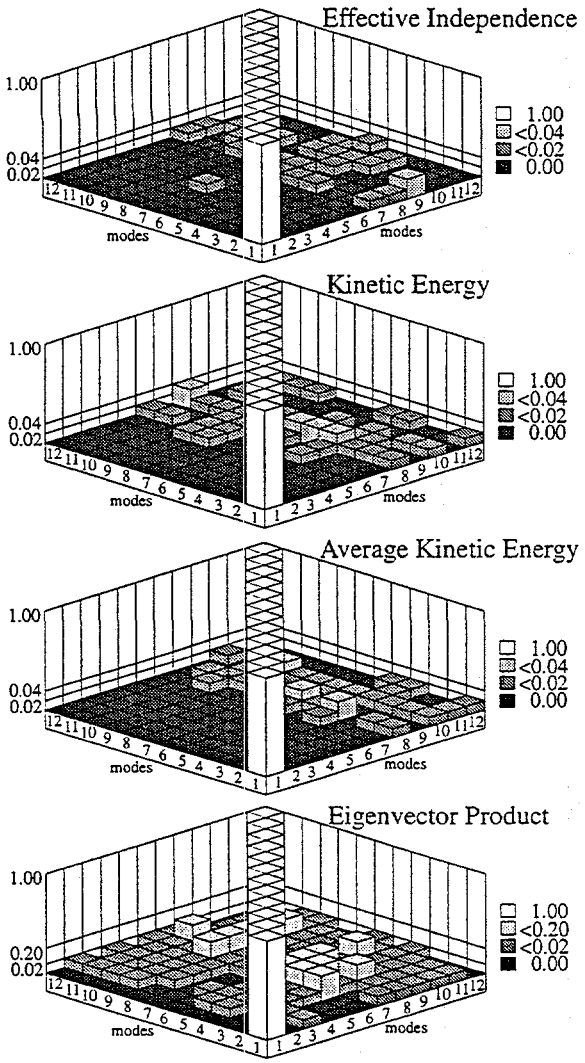

Figure 6.2.4: Cross-orthogonality between identified and FEM modes (constrained)

For the unconstrained sensor sets, the EI, KE, and AKE techniques resulted in generally acceptable cross-orthogonality values for the twelve target modes shown in Fig. 6.2.3. Only a few off-diagonal entries of the cross-orthogonalities resulting from these sensor configuration were above the acceptable limit of <0.02 for primary modes, but were still within the acceptable limit of <0.10 for secondary modes. The error added to the model in this example had little effect on the placement techniques' success in identifying sensor configurations which resulted in successful modal information identification.

For the triaxially constrained sensor configuration, the model error did not greatly affect the uncorrupted cross-orthogonality results for the EI, KE, and AKE techniques, as shown in Fig. 6.2.4. Even though these cross-orthogonalities are not as good as those obtained with no model error, they still lie within acceptable limits (previously discussed). Therefore, the error added to the model in this example had little effect on the constrained placement problem for the EI, KE, and AKE techniques. For the EVP technique, the model error resulted in a new triaxially constrained configuration which out-performed the uncorrupted configuration by chance as can be seen by the cross-orthogonalities pictured in the bottom portion of Fig. 6.2.4. This is probably due to the fact that a triax-set was moved to the previously uninstrumented main boom. Even though an improvement can be seen here, several of the cross-orthogonalities are above the acceptable limits for second mode identification (>0.10).

7. COMPUTATIONAL COST

The size of the FEM used in both the excitation and sensor placement techniques is the basic factor in the computational cost of each technique; the larger the FEM, the greater the computational cost of selecting the excitations and sensors. This computational effort is generally worthwhile, compared to the cost of planning, implementing, and performing a modal test. For the example used in this study, the least costly sensor placement technique (EVP) was not successful in placing sensors to identify modal information.

For the excitation placement, the most expensive part of the calculation is the MIF calculation for each possible design. As the GA searches for candidate excitation locations, the MIF for each possible location must be calculated in order to evaluate the objective function. For the sensor placement techniques, the computational cost for the EVP technique is on the order of 10^3 MATLAB flops, for the KE and AKE techniques is on the order of 10^6 MATLAB flops and for the EI technique is on the order of 10^7 MATLAB flops. For the example used in this work, the mass matrix was (240x240) DOFs and the target mode matrix was (240x12). The 8-bay truss example used in [15] had a mass matrix of (80x80) DOFs and a target mode matrix of (80x5). The computational costs of the EVP, KE and AKE, and EI techniques were on the order of 10^2, 10^4, and 10^5 MATLAB flops. Therefore, an increase in computational cost of approximately order 2 can be seen when the number of DOFs and the number of target modes are approximately tripled.

One way to reduce the computational cost of the techniques evaluated, especially effective independence and GA/MIF techniques, is to reduce the initial set of candidate DOFs to a target set. For the size example used in this work, this reduction is not essential, but a reduction may be needed for larger models.

8. SUMMARY

A comparative study of several pre-modal-test planning techniques was presented using the JPL/MPI testbed. Mode indicator functions calculated using a reduced FEM of the MPI structure were used in conjunction with a GA to find location and orientation of two excitation sources in order to optimally excite a chosen range of FE target modes during a modal test. The original and GA/MIF excitation locations were compared using the MPI's simulated structural response to impulses applied at the exciter locations. The GA/MIF excitation location resulted in a time response to an impulse from which the 12 target modes were successfully identified. The original excitation locations resulted in a time response to an impulse from which there was a problem extracting modes 5 and 10. It should be noted that the original excitation was chosen by an experienced team of experimentalists/analysts, using a careful examination of the modes shapes to define a set of candidate excitations, along with MIFs to select and verify the final set. Despite this, there is still some room for improvement. This indicates the utility of a suite of pre-test planning tools to assist the designer, improving the efficiency and completeness of the process.

Effective independence, kinetic energy, and eigenvector product techniques, were used to place a combination of sensors on the structure for the purpose of modal identification in two ways: independent sensor placement and triaxially constrained placement. For the unconstrained and triaxially constrained sensor configurations the EI, KE, and AKE techniques were successful in indentifying the target modes and frequencies from the noisy time response. The EI technique resulted in the best identification for the unconstrained set and the KE technique resulted in the best identification for the constrained set. The EVP technique was not successful in identifying the target modes for either the unconstrained or triaxially constrained sets.

Error was added to the FEM of the MPI structure in order to evaluate its effect on the placement techniques. Based on the amount of error added in this example, there was little effect seen on either the excitation or sensor placement techniques.

ACKNOWLEDGEMENTS

The authors would like to thank Sandia National Laboratories and the NASA/Florida Space Grant Consortium for their support.

REFERENCES

[1] Kammer, D. C.,"Sensor Placement for On-Orbit Modal Identification and Correlation of Large Space Structures," *Journal of Guidance, Control, and Dynamics,* v15 n2, March-April 1991, pp. 251-259.

[2] Shah, P. C. and Udwadia, F. E., "Methodology for Optimal Sensor Locations for Identification of Dynamic Systems," *Journal of Applied Mechanics,* v 45, March 1978, pp. 188–196.

[3] Udwadia, F. E., and Garba, J. A., "Optimal Sensor Locations for Structural Identification," *JPL Proceedings of the Workshop on Identification and Control of Flexible Space Structures,* April 1985, pp. 247-261.

[4] Salama, M., Rose, T., and Garba, J.,"Optimal Placement of Excitations and Sensors for Verification of Large Dynamical Systems," Proceedings of the 28th AIAA/ASME Structures, Structural Dyanmics, and Materials Conference, pp. 1024-31.

[5] Jarvis, Brian, "Enhancement to Modal Testing Using Finite Elements," *Sound and Vibration,* August 1991, pp. 28-30.

[6] Hunt, D. L., Vold, H., Peterson, E. L., and Williams, R., "Optimal Selection of Excitation Methods for Enhanced Modal Testing," Proceedings of the 25th AIAA/ASME Structures, Structural Dynamics, and Materials Conference, 1984.

[7] Williams, R., Crowley, J., and Vold, H., "The Multivariant Mode Indicator Function in Modal Analysis," Proceedings of the 3rd International Modal Analysis Conference, 1985.

[8] Holland, J. H., *Adaptation in Natural and Artificial Systems,* The University of Michigan press, Ann Arbor, 1975.

[9] Zimmerman, D. C., "A Darwinian Approach to the Actuator Placement Problem With Nonnegligible Actuator Mass," *Mechanical Systems and Signal Processing,* v7 n4, 1993, pp. 363-374.

[10] Red-Horse, J. R., Marek, E. L., Levine-West, M., "System Identification of the JPL Micro-Precision Interferometer Truss: Test-Analysis Reconciliation," Proceedings of the 34th AIAA/ASME Structures, Structural Dynamics, and Materials Conference, LaJolla, CA, 1993, pp. 3353-3365.

[11] Carne, T. G., Mayes, R. L., and Levine-West, M. B., "A Modal TEst of a Space-Truss for Structural Parameter Identification," Proceedings of the 11th International Modal Analysis Conference, Kissimee, FL, 1993, pp. 486-494.

[12] Levine-West, M., Kissil, A., and Milman, M., "Evaluation of Mode Shape Expansion Techniques on the Micro-Precision Interferometer Truss," Proceedings of the 12th International Modal Analysis Conference, Honolulu, HA, 1994, pp. 212–218.

[13] Juang, J., and Pappa, R., "An Eigensystem Realization Algorithm for Modal Parameter Identification

and Model Reduction," *Journal of Guidance and Control,* v8, Sept.-Oct. 1985, pp. 620-627.

[14] O'Callahan, J.C., Avitabile P.A. and Riemer, R. (1989), "System Equivalent Reduction Expansion Process (SEREP)," Proceedings of the 7th International Modal Analysis Conference, Las Vegas, NA, pp. 29-37.

[15] Larson, C. B., Zimmerman, D. C., and Marek, E. L., "A Comparison of Modal Test Planning Techniques: Excitation and Sensor Placement Using the NASA 8-Bay Truss," Proceedings of the 12th International Modal Analysis Conference, Honolulu, HA, 1994, pp. 205-211.

[16] Flanigan, Christopher C., and David L. Hunt, "Integration of Pretest Analysis and Model Correlation Methods for Modal Surveys," Proceedings of the 11th International Modal Analysis Conference, Kissimee, February 1993, pp 444-448.

AIAA-94-1525-CP

ARMAX IDENTIFICATION OF VIBRATING STRUCTURES: MODEL AND MODEL ORDER ESTIMATION

Marc P. Mignolet*
Department of Mechanical and Aerospace Engineering
Arizona State University, Tempe, Arizona 85287-6106.

John R. Red-Horse
Sandia National Laboratories
Albuquerque, New Mexico 87185-5800.

Abstract

The determination of the model characteristics, number and values of natural frequencies, damping ratios, and mode shapes of a vibrating structure from records of its excitation and its response is investigated. First, a multistage eXogeneous Autoregressive Moving Average (ARMAX) procedure, recently employed in a single response measurement format is reviewed and extended to yield not only estimates of the natural frequencies and damping ratios but also of the mode shapes of a structure. The reliability of this technique, even in the presence of strong measurement noise, led to the introduction of a simple and efficient model order determination technique that relies on identification results obtained with different sets of data. Four examples of application are presented that demonstrate the reliability of the proposed model and model order estimation technique for both simulated and experimental data.

Introduction

The determination of the natural frequencies, damping ratios, and mode shapes of a vibrating structure from experimental measurements of its response represents an important classical problem of structural dynamics. Accordingly, a large number of solutions to this identification problem have been suggested that differ from each other not only by the specific numerical algorithm used but also by the data assumed available, i.e. forced or free vibration measurements, response of a single degree-of-freedom or of the entire structure, etc. Some recent results in this area[1,2] indicate that discrete systems concepts, eXogeneous Autoregressive Moving Average (ARMAX) modeling in particular, can lead to reliable estimates of the dynamic characteristics of a structure even in the presence of strong measurement noise. In fact, in Ref. 2 a novel identification algorithm was presented that provided accurate estimates of the natural frequencies and damping ratios of a multi-degree-of-freedom (MDOF) system from the time histories of the excitation and the response of only one of the degrees-of-freedom even for signal-to-noise ratio of 5. Accordingly, the first goal of the present paper is to extend the technique described in Ref. 2 to the estimation of the natural frequencies and damping ratios but also of the mode shapes of a MDOF system from records of both the excitation and the response of some of its degrees-of-freedom.

The numerical algorithm to be presented assumes, as most other identification schemes do, that the order of the system, or equivalently, the number of its observable natural frequencies is known a priori. In many practical applications, however, this hypothesis is not satisfied; the structure is a continuous system whose frequency spectrum is unknown. It is thus impossible to precisely specify the number of natural frequencies that lie in the frequency domain analyzed. Information-theoretic criterion, such as the Akaike Information Criterion[3] (AIC) and the Minimum Description Length[4] (MDL) have sometimes been suggested to resolve this uncertainty. Their reliability in the context of the present identification technique has however been found unsatisfactory[2] so that an alternate approach is required. The second objective of the present paper is thus to introduce a simple model order determination technique that can reliably be used in connection with the proposed identification scheme. For completeness, the connections between vibrating multi-degree-of-freedom systems and ARMAX models will first be briefly reviewed.

ARMAX Models and Vibrating Structures

Consider a multi-degree-of-freedom (MDOF) system described by the equations of motion

$$M \ddot{\underline{X}}(t) + C \dot{\underline{X}}(t) + K \underline{X}(t) = \underline{F}(t) \qquad (1)$$

where $\underline{X}(t)$ denotes the time-dependent vector whose N components uniquely and unambiguously specify the position of all the points of the structure at time t. The symbols M, C and K designate the $N \times N$ mass,

---

[*] Associate Professor

Copyright © by the American Institute of Aeronautics and Astronautics. All Rights Reserved.

damping, and stiffness matrices, respectively. Further, the vector $\underline{F}(t)$ represents the loading on the structure which can be approximated by a series of impulses, that is

$$\underline{F}(t) = \sum_{n=-\infty}^{\infty} \underline{F}_n \, \delta\left[t - (n \, \Delta t)^{-}\right]. \tag{2}$$

Then, under mild conditions, it can be shown (see Ref. 2 and 5 for a proof) that a set of p components of the response vector $\underline{X}(t)$ admits an Autoregressive Moving Average (ARMA) representation of the form

$$\underline{\tilde{X}}_n = - \sum_{k=1}^{s} \tilde{A}_k \, \underline{\tilde{X}}_{n-k} + \sum_{l=1}^{s} \tilde{B}_l \, \underline{F}_{n+1-l} \tag{3}$$

where

$$\underline{\tilde{X}}_n = \underline{\tilde{X}}(n \, \Delta t) \quad n = 1, 2, 3, .. \tag{4}$$

for some matrices $\tilde{A}_k$, $k = 1, 2, ..., s$, and $\tilde{B}_l$, $l = 1, 2, ..., s$, of respective dimensions $p \times p$ and $p \times N$ (see Ref. 2). Further, in Eq. (3), the index s equals $2N/p$ (hereafter assumed to be an integer). Introducing the notation $\tilde{A}_0 = I_p$, it is readily seen that Eq. (3) reduces to the relation

$$\sum_{k=0}^{s} \tilde{A}_k \, \underline{\tilde{X}}_{n-k} = \sum_{l=0}^{s-1} \tilde{B}_l \, \underline{F}_{n-l}. \tag{5}$$

In terms of z transform, the above ARMA representation can conveniently be written in the form

$$\tilde{A}(z) \, \underline{\tilde{X}}(z) = \tilde{B}(z) \, \underline{F}(z) \tag{6}$$

where

$$\tilde{A}(z) = \sum_{k=0}^{s} \tilde{A}_k \, z^{-k} \tag{7}$$

$$\tilde{B}(z) = \sum_{l=0}^{s-1} \tilde{B}_l \, z^{-l} \tag{8}$$

$$\underline{\tilde{X}}(z) = \sum_{n=-\infty}^{\infty} \underline{\tilde{X}}_n \, z^{-n} \tag{9}$$

and

$$\underline{F}(z) = \sum_{n=-\infty}^{\infty} \underline{F}_n \, z^{-n}. \tag{10}$$

To use the above ARMA representation, Eq. (5) and (6), for the purpose of structural identification, it is necessary to dispose of a connection between the matrices $\tilde{A}_k$ and $\tilde{B}_l$ and the modal characteristics of the vibrating structure. In this respect, it has been shown (see Ref. 1 and 2 for example) that the $s \times p = N$ roots, z_l, of the equation

$$\det \tilde{A}(z) = 0 \tag{11}$$

are related to the poles, s_l, of the transfer function of the continuous system defined by Eq. (1) according to

$$z_l = e^{s_l \Delta t}. \tag{12}$$

Introducing the natural frequency, ω_l, and the damping ratio, ζ_l, of the l^{th} mode of vibration by the relations

$$\begin{Bmatrix} s_{2l-1} \\ s_{2l} \end{Bmatrix} = - \zeta_l \, \omega_l \pm j \, \omega_l \sqrt{1 - \zeta_l^2} \quad l = 1, 2, .., N \tag{13}$$

it is readily shown that

$$\omega_l = \frac{1}{\Delta t} \left| \ln z_l \right| = \frac{1}{\Delta t} \left[\left[\ln |z_l| \right]^2 + \alpha_l^2 \right]^{1/2} \tag{14}$$

and

$$\zeta_l = - \frac{1}{\omega_l} \ln |z_l| \tag{15}$$

where

$$\alpha_l = \tan^{-1} \left[\frac{\mathrm{Img}(z_l)}{\mathrm{Re}(z_l)} \right] \quad \alpha_l \in [-\pi, \pi]. \tag{16}$$

The determination of the mode shapes, $\underline{\phi}_l$, of the structure can also be achieved from the ARMA model Eq. (5). Specifically, it can be shown[2] that $\underline{\phi}_l$ is the eigenvector of the matrix $A(z_l)$ corresponding to the zero eigenvalue.

Effect of Measurement Noise and Maximum Likelihood Estimation

In practical situations, it is impossible to obtain a time series of either the excitation $\underline{F}(t)$ or the response $\underline{\tilde{X}}(t)$ that is devoid of measurement noise. Then, the observed samples $\underline{F}_n^{(o)}$ and $\underline{\tilde{X}}_n^{(o)}$ can be written in the form

$$\underline{\tilde{X}}_n^{(o)} = \underline{\tilde{X}}_n + \underline{E}_n^{(1)} \tag{17}$$

and

$$\underline{F}_n^{(o)} = \underline{F}_n + \underline{E}_n^{(2)} \tag{18}$$

where the noise terms $\underline{E}_n^{(1)}$ and $\underline{E}_n^{(2)}$ are often modeled as Gaussian multivariate discrete white noise processes satisfying the conditions

$$E \left[\underline{E}_n^{(k)} \left[\underline{E}_m^{(l)} \right]^T \right] = 0 \;\; \text{for } m \neq n \; . \tag{19}$$

Note in the above equation that the superscript ^{T} denotes the operation of matrix transposition. Under the above assumptions, it is found that the observed response vector $\underline{\tilde{X}}_n^{(o)}$ admits the ARMAX representation

$$\sum_{k=0}^{s} \tilde{A}_k \, \underline{\tilde{X}}_{n-k}^{(o)} = \sum_{l=0}^{s-1} \tilde{B}_l \, \underline{F}_{n-l}^{(o)} + \sum_{k=0}^{s} \tilde{C}_k \, \underline{E}_{n-k} \tag{20}$$

for some $p \times p$ matrices $\tilde{C}_k$ and where the p components of the random vector $\underline{E}_n$ are independent white noises of identical variance σ^2, i.e.

$$E \left[\underline{E}_n \, \underline{E}_m^T \right] = \sigma^2 \, I_p \, \delta_{mn}. \tag{21}$$

Note that the autoregressive and moving average orders are both equal to s while the exogeneous one is $s-1$. If there exists a temporal correlation between the samples of the noise vectors $\underline{E}_n^{(1)}$ and/or $\underline{E}_n^{(2)}$, the ARMAX model, Eq. (20), still describes the response process with a MA order larger than s. Note that the determination of a moving average larger than its autoregressive counterpart could also indicate the presence of unmodeled dynamics, such as a nonlinearity in the system.

The estimation of the elements of the matrices $\tilde{A}_k$, $\tilde{B}_l$ and $\tilde{C}_k$ from time histories of both the response, $\underline{\tilde{X}}_n^{(o)}$, and the excitation, $\underline{F}_n^{(o)}$, can be achieved through the maximization of the likelihood function. Relying on classical results (see Ref. 2 for a more detailed discussion), it can be shown that this criterion is equivalent to the minimization of the error

$$\varepsilon_{ML} = \frac{1}{2\,\omega_b} \int_{-\omega_b}^{\omega_b} \left\{ \tilde{C}^{-1}(\omega) \left[\tilde{A}(\omega)\,\underline{\tilde{X}}^{(o)}(\omega) - \tilde{B}(\omega)\,\underline{F}^{(o)}(\omega) \right] \right\}^H$$

$$\left\{ \tilde{C}^{-1}(\omega) \left[\tilde{A}(\omega)\,\underline{\tilde{X}}^{(o)}(\omega) - \tilde{B}(\omega)\,\underline{F}^{(o)}(\omega) \right] \right\} d\omega \quad (22)$$

under the constraint $\tilde{A}_0 = I_p$. In the above equation, the functions $\underline{\tilde{X}}^{(o)}(\omega)$ and $\underline{F}^{(o)}(\omega)$ denote the observed values of the z transforms $\underline{\tilde{X}}(z)$ and $\underline{F}(z)$, Eq. (9) and (10), evaluated at $z = e^{j\omega\Delta t}$ and the superscript ^{H} represents the combined operation of complex conjugation and matrix transposition. Further, ω_b designates the Nyquist frequency

$$\omega_b = \frac{\pi}{\Delta t} \quad (23)$$

and

$$\tilde{C}(z) = \sum_{k=0}^{s} \tilde{C}_k \, z^{-k}. \quad (24)$$

Model Estimation

Expanding Eq. (22), it can be shown that ε_{ML} is a quadratic function of the elements of the matrices $\tilde{A}_k$ and $\tilde{B}_l$ but involves the MA parameters $\tilde{C}_k$ in a highly nonlinear way. This observation suggests the use of an iterative procedure in which the matrices $\tilde{A}_k$ and $\tilde{B}_l$ are indeed selected to minimize ε_{ML} for a given function $\tilde{C}(\omega)$ through, as will be shown later, the solution of a linear system of equations. Then, an updating procedure is employed to obtain a new set of matrices $\tilde{C}_k$ which, in turn, are used to produce new matrices $\tilde{A}_k$ and $\tilde{B}_l$. Upon convergence of this iterative technique, a minimum of ε_{ML} is achieved. The specific steps, which are described below, can also be visualized in the flow chart presented in Fig. 1.

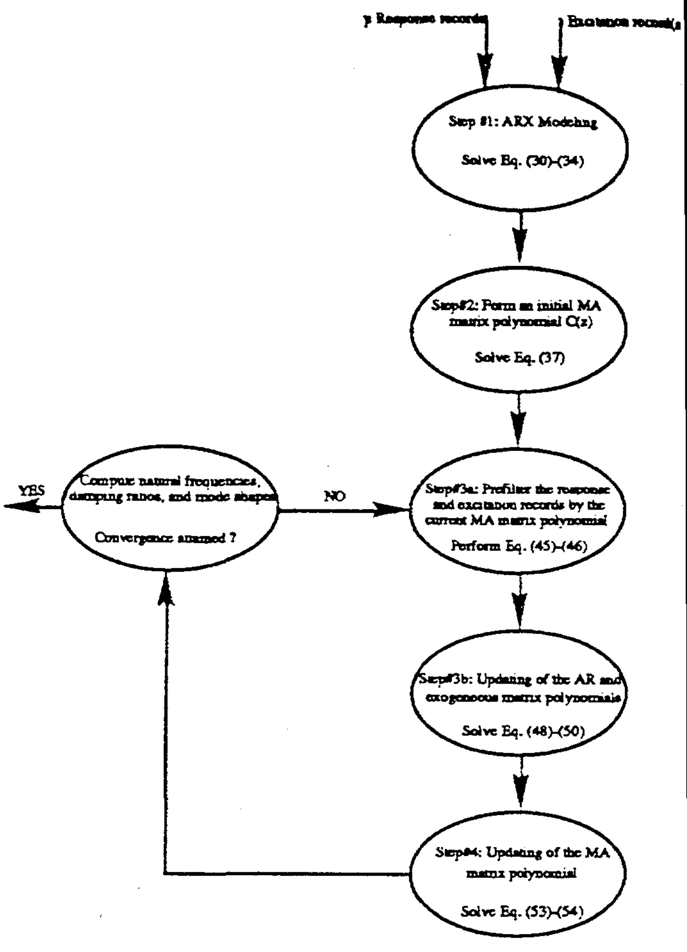

Fig. 1 Flowchart of the iterative ARMAX modeling technique

Step #1: ARX Modeling

Introducing the notations

$$\hat{A}(z) = \tilde{C}_0\,\tilde{C}^{-1}(z)\,\tilde{A}(z) = I_p + \hat{A}_1 z^{-1} + \cdots$$

$$= \sum_{k=0}^{\infty} \hat{A}_k\, z^{-k} \simeq \sum_{k=0}^{m} \hat{A}_k\, z^{-k} \quad m \ large \quad (25)$$

$$\hat{B}(z) = \tilde{C}_0\,\tilde{C}^{-1}(z)\,\tilde{B}(z) = \hat{B}_0 + \hat{B}_1 z^{-1} + \cdots$$

$$= \sum_{k=0}^{\infty} \hat{B}_k\, z^{-k} \simeq \sum_{k=0}^{m} \hat{B}_k\, z^{-k} \quad m \ large \quad (26)$$

and

$$\hat{C}_0 = \tilde{C}_0 \quad (27)$$

it is seen that the ARMAX model, Eq. (5) and (6), admits a long ARX approximation of the form

$$\sum_{k=0}^{m} \hat{A}_k \, \underline{\tilde{X}}_{n-k}^{(o)} = \sum_{l=0}^{m} \hat{B}_l \, \underline{F}_{n-l}^{(o)} + \hat{C}_0 \, \underline{E}_n \tag{28}$$

where $\hat{A}_0 = I_p$. For this model, the minimum of ε_{ML} defined by Eq. (22) or, equivalently, as

$$\varepsilon_{ML} = \frac{1}{2\omega_b} \int_{-\omega_b}^{\omega_b} \left[\hat{A}(\omega) \, \underline{\tilde{X}}^{(o)}(\omega) - \hat{B}(\omega) \, \underline{F}^{(o)}(\omega) \right]^H \hat{C}_0^{-T} \hat{C}_0^{-1} \left[\hat{A}(\omega) \underline{\tilde{X}}^{(o)}(\omega) - \hat{B}(\omega) \underline{F}^{(o)}(\omega) \right] d\omega \tag{29}$$

is achieved by selecting the matrices $\hat{A}_k$, $k = 1, 2, .., m$, and $\hat{B}_l$, $l = 0, 1, 2, .., m$, to satisfy the linear system of equations

$$\left[\sum_{n=m+1}^{r} \underline{Y}_n \, \underline{Y}_n^T \right] \hat{Z}^T = - \sum_{n=m+1}^{r} \underline{Y}_n \left[\underline{\tilde{x}}_n^{(o)} \right]^T \tag{30}$$

where r represents the number of observed samples of the excitation and responses,

$$\underline{Y}_n^T = \left[\left[\underline{\tilde{x}}_{n-1}^{(o)} \right]^T \left[\underline{\tilde{x}}_{n-2}^{(o)} \right]^T \cdots \left[\underline{\tilde{x}}_{n-m}^{(o)} \right]^T \left[-\underline{F}_n^{(o)} \right]^T \left[-\underline{F}_{n-1}^{(o)} \right]^T \cdots \left[-\underline{F}_{n-m}^{(o)} \right]^T \tag{31}$$

and

$$\hat{Z} = \left[\hat{A}_1 \, \hat{A}_2 \cdots \hat{A}_m \, \hat{B}_0 \, \hat{B}_1 \cdots \hat{B}_m \right]. \tag{32}$$

Once the parameters $\hat{A}_k$ and $\hat{B}_l$ have been determined from Eq. (30)-(32), the matrix $\hat{C}_0$ should be specified to complete the ARX model, Eq. (28). This could be achieved by selecting either

$$\hat{C}_0 = I_p \tag{33}$$

or $\hat{C}_0$ to be the matrix such that the noise components $\underline{E}_n$ satisfy Eq. (21). That is,

$$E\left[(\hat{C}_0 \underline{E}_n)(\hat{C}_0 \underline{E}_n)^T \right] = \sigma^2 \hat{C}_0 \hat{C}_0^T = \frac{1}{r-m} \sum_{n=m+1}^{r} \left[\sum_{k=0}^{m} \hat{A}_k \, \underline{\tilde{X}}_{n-k}^{(o)} - \sum_{l=0}^{m} \hat{B}_l \, \underline{F}_{n-l}^{(o)} \right] \times \left[\sum_{k=0}^{m} \hat{A}_k \, \underline{\tilde{X}}_{n-k}^{(o)} - \sum_{l=0}^{m} \hat{B}_l \, \underline{F}_{n-l}^{(o)} \right]^T. \tag{34}$$

For simplicity, the matrix $\hat{C}_0$ satisfying the above equation could be selected to be lower triangular. It is then easily computed from Eq. (34) by using the Cholesky factorization algorithm.

Step #2: Initial AR and exogeneous parameters

Initial AR and exogeneous parameters, $\tilde{A}_k^{(0)}$ and $\tilde{C}_k^{(0}$ can be obtained by requiring that

$$\left[\tilde{C}^{(0)}(z) \right]^{-1} \tilde{A}^{(0)}(z) \approx \hat{C}_0^{-1} \hat{A}(z) \tag{35}$$

or equivalently, by minimizing the error

$$\varepsilon_S = \left| \tilde{C}^{(1)}(\omega) \, \hat{C}_0^{-1} \, \hat{A}(\omega) - \tilde{A}^{(1)}(\omega) \right|^2$$

$$= \frac{1}{2\omega_b} \int_{-\omega_b}^{\omega_b} tr \left\{ \left[\tilde{C}^{(1)}(\omega) \, \hat{C}_0^{-1} \, \hat{A}(\omega) - \tilde{A}^{(1)}(\omega) \right]^H \left[\tilde{C}^{(1)}(\omega) \, \hat{C}_0^{-1} \, \hat{A}(\omega) - \tilde{A}^{(1)}(\omega) \right] d\omega \tag{36}$$

where $tr\,U$ denotes the trace of an arbitrary matrix U, with respect to the elements of the matrices $\tilde{A}_k^{(1)}$ and $\tilde{C}_k^{(1)}$, $k = 1, 2, ..., s$. Note that the condition given by Eq. (27) is still enforced.

The minimization of ε_S, Eq. (36), is accomplished when the parameters $\tilde{C}_k^{(1)}$, $k = 1, 2, .., s$, satisfy the linear system of equations

$$\sum_{l=1}^{s} \left[\sum_{n=max(k,l)}^{min(m+k,m+l)} \hat{A}_{n-k} \, \hat{A}_{n-l}^T \right] \left[\tilde{C}_l^{(1)} \, \hat{C}_0^{-1} \right]^T = - \sum_{n=k}^{m} \hat{A}_{n-k} \, \hat{A}_n^T \tag{37}$$

for $k = 1, 2, .., s$.

Step #3: Updating of AR and exogeneous parameters

This third step can in fact be viewed as composed of two different operations. The first one, referred to as prefiltering, aims at rewriting the error ε_{ML} in a form that is more amenable to the second operation which represents the determination of the matrices $A_k^{(i+1)}$ and $B_l^{(i+1)}$ minimizing ε_{ML} for a given MA polynomial $\tilde{C}(z)$.

Step #3a: Prefiltering

It might appear at first that the minimization of ε_{ML}, Eq. (22), would require the use of a numerical quadrature algorithm for the evaluation of the integrals involving the inverse $\tilde{C}^{-1}(\omega)$ of the MA polynomial $\tilde{C}(z)$. Note however that the samples Q_k corresponding to the z transform $Q(z) = \tilde{C}^{-1}(z) R(z)$ can easily and recursively computed as

$$\tilde{C}(z) \, Q(z) = R(z) \tag{38}$$

or

$$\sum_{k=0}^{s} \tilde{C}_k \, Q_{n-k} = R_n \tag{39}$$

or, finally,

$$Q_n = \tilde{C}_0^{-1} \left[R_n - \sum_{k=1}^{s} \tilde{C}_k \, Q_{n-k} \right]. \tag{40}$$

In trying to apply the above concepts to the expressions $\tilde{C}^{-1}(z) \tilde{A}(z) \underline{\tilde{X}}^{(o)}(z)$ and $\tilde{C}^{-1}(z) \tilde{B}(z) \underline{F}^{(o)}(z)$, see Eq. (22), with $\tilde{C}(z) = \tilde{C}^{(i)}(z)$ known and $\tilde{A}(z) = \tilde{A}^{(i+1)}(z)$, $\tilde{B}(z) = \tilde{B}^{(i+1)}(z)$ unknown, it is directly recognized that the recurrence computation specified by Eq. (40) cannot be achieved since the matrices $\tilde{A}_k^{(i+1)}$ and $\tilde{B}_l^{(i+1)}$ have not yet been determined. This problem can be circumvented by express-ing the AR and exogeneous polynomials $\tilde{A}^{(i+1)}(z)$ and $\tilde{B}^{(i+1)}(z)$ in terms of their components $\tilde{A}^{(i+1)}_{,\alpha\beta}(z)$ and $\tilde{B}^{(i+1)}_{,\gamma\delta}(z)$ as follows

$$\tilde{A}^{(i+1)}(\omega) = \sum_{\alpha,\beta=1}^{p} \tilde{A}^{(i+1)}_{,\alpha\beta}(\omega)\, \underline{u}_{\alpha}\, \underline{u}_{\beta}^{T} \tag{41}$$

and

$$\tilde{B}^{(i+1)}(\omega) = \sum_{\gamma=1}^{p} \sum_{\delta=1}^{N} \tilde{B}^{(i+1)}_{,\gamma\delta}(\omega)\, \underline{u}_{\gamma}\, \underline{v}_{\delta}^{T}. \tag{42}$$

where $\underline{u}_k$ and $\underline{v}_k$ denote the vectors of respective dimensions $p \times 1$ and $N \times 1$ whose components are all zero except the k^{th} one which equals unity. Then, the products $\left[\tilde{C}^{(i)}(\omega)\right]^{-1} \tilde{A}^{(i+1)}(\omega)\, \underline{\tilde{x}}^{(o)}(\omega)$ and $\left[\tilde{C}^{(i)}(\omega)\right]^{-1} \tilde{B}^{(i+1)}(\omega)\, \underline{F}^{(o)}(\omega)$ can be written in the forms

$$\left[\tilde{C}^{(i)}(\omega)\right]^{-1} \tilde{A}^{(i+1)}(\omega)\, \underline{\tilde{x}}^{(o)}(\omega)$$

$$= \sum_{\alpha,\beta=1}^{p} \tilde{A}^{(i+1)}_{,\alpha\beta}(\omega) \left[\left[\tilde{C}^{(i)}(\omega)\right]^{-1} \underline{u}_{\alpha}\, \underline{u}_{\beta}^{T}\, \underline{\tilde{x}}^{(o)}(\omega)\right]$$

$$= \sum_{\alpha,\beta=1}^{p} \tilde{A}^{(i+1)}_{,\alpha\beta}(\omega)\, \underline{U}^{(i)}_{\alpha\beta}(\omega) \tag{43}$$

and

$$\left[\tilde{C}^{(i)}(\omega)\right]^{-1} \tilde{B}^{(i+1)}(\omega)\, \underline{F}^{(o)}(\omega)$$

$$= \sum_{\gamma=1}^{p} \sum_{\delta=1}^{N} \tilde{B}^{(i+1)}_{,\gamma\delta}(\omega) \left[\left[\tilde{C}^{(i)}(\omega)\right]^{-1} \underline{u}_{\gamma}\, \underline{v}_{\delta}^{T}\, \underline{F}^{(o)}(\omega)\right]$$

$$= \sum_{\gamma=1}^{p} \sum_{\delta=1}^{N} \tilde{B}^{(i+1)}_{,\gamma\delta}(\omega)\, \underline{V}^{(i)}_{\gamma\delta}(\omega) \tag{44}$$

where the vectors $\underline{U}^{(i)}_{\alpha\beta}(\omega)$ and $\underline{V}^{(i)}_{\gamma\delta}(\omega)$ represent the bracketed terms in Eq. (43) and (44). These quantities can be computed as in Eq. (40) in the form

$$\tilde{C}_0\, \underline{U}^{(i)}_{\alpha\beta}(n) = - \sum_{k=1}^{s} \tilde{C}_k^{(i)}\, \underline{U}^{(i)}_{\alpha\beta}(n-k) + \underline{u}_{\alpha} \left[\underline{u}_{\beta}^{T}\, \underline{\tilde{x}}_{n}^{(o)}\right]. \tag{45}$$

and

$$\tilde{C}_0\, \underline{V}^{(i)}_{\gamma\delta}(n) = - \sum_{k=1}^{s} \tilde{C}_k^{(i)}\, \underline{V}^{(i)}_{\gamma\delta}(n-k) + \underline{u}_{\gamma} \left[\underline{v}_{\delta}^{T}\, \underline{F}_{n}^{(o)}\right]. \tag{46}$$

Step #3b: Updating of AR and exogeneous parameters

With the notations introduce above, the error $\varepsilon^{(i)}_{ML}$ can be rewritten as

$$\varepsilon^{(i)}_{ML} = \frac{1}{2\omega_b} \int_{-\omega_b}^{\omega_b} \left[\sum_{\alpha,\beta=1}^{p} \tilde{A}^{(i+1)}_{,\alpha\beta}(\omega) \underline{U}^{(i)}_{\alpha\beta}(\omega) - \sum_{\gamma=1}^{p}\sum_{\delta=1}^{N} \tilde{B}^{(i+1)}_{,\gamma\delta}(\omega) \underline{V}^{(i)}_{\gamma\delta}(\omega) \right]^{H}$$
$$\left[\sum_{\alpha,\beta=1}^{p} \tilde{A}^{(i+1)}_{,\alpha\beta}(\omega) \underline{U}^{(i)}_{\alpha\beta}(\omega) - \sum_{\gamma=1}^{p}\sum_{\delta=1}^{N} \tilde{B}^{(i+1)}_{,\gamma\delta}(\omega) \underline{V}^{(i)}_{\gamma\delta}(\omega) \right] d\omega. \tag{47}$$

Then, it can be shown that its minimization with respect to the elements $\tilde{A}^{(i+1)}_{k,\alpha\beta}$, $k=1,2,..,s$, and $\alpha,\beta=1,2,..,p$, and $\tilde{B}^{(i+1)}_{l,\gamma\delta}$, $l=0,1,..,s-1$, $\gamma=1,2,..,p$ and $\delta=1,2,..,N$, leads finally to the linear system of equations

$$\left[\sum_{n=s+1}^{r} \underline{\Psi}_n\, \underline{\Psi}_n^{T}\right] \underline{\tilde{Z}} = - \sum_{n=s+1}^{r} \underline{\Psi}_n \left[\sum_{k=1}^{p} \underline{U}_{kk}(i)(n)\right] \tag{48}$$

where

$$\underline{\Psi}_n^{T} = [\, \underline{U}^{(i)}_{11}(n-1)\ \underline{U}^{(i)}_{21}(n-1) \,..\, \underline{U}^{(i)}_{p1}(n-1) \,..\, \underline{U}_{pp}(i)(n-1)$$
$$\underline{U}^{(i)}_{11}(n-2) \,..\, \underline{U}^{(i)}_{pp}(n-s)\ \underline{-V}^{(i)}_{11}(n)\ \underline{-V}^{(i)}_{21}(n) \,..$$
$$\underline{-V}^{(i)}_{p1}(n) \,..\, \underline{-V}_{pN}(i)(n)\ \underline{-V}^{(i)}_{11}(n-1) \,..\, \underline{-V}^{(i)}_{pN}(n-s+1)\,] \tag{49}$$

and

$$\underline{\tilde{Z}}^{T} = [\tilde{A}^{(i+1)}_{1,11} \tilde{A}^{(i+1)}_{1,21} .. \tilde{A}^{(i+1)}_{1,p1} \tilde{A}^{(i+1)}_{1,12} .. \tilde{A}^{(i+1)}_{1,pp} \tilde{A}^{(i+1)}_{2,11} .. \tilde{A}^{(i+1)}_{s,pp}$$
$$\tilde{B}^{(i+1)}_{0,11} \tilde{B}^{(i+1)}_{0,21} .. \tilde{B}^{(i+1)}_{0,p1} \tilde{B}^{(i+1)}_{0,12} .. \tilde{B}^{(i+1)}_{0,pN} \tilde{B}^{(i+1)}_{1,11} .. \tilde{B}^{(i+1)}_{s-1,pN}]. \tag{50}$$

Step #4: Updating of the MA parameters

The second and final step of the updating procedure represents the selection of a matrix polynomial $\tilde{C}(z) = \tilde{C}^{(i+1)}(z)$ that satisfies "at best" Eq. (25). Specifically, select the MA parameters $\tilde{C}_k^{(i+1)}$, $k=0,1,..,s$, to minimize the error

$$\varepsilon_C = \left| \tilde{C}^{(i+1)}(\omega)\, \hat{C}_0^{-1}\, \hat{A}(\omega) \left[\tilde{A}^{(i+1)}(\omega)\right]^{-1} - I_p \right|^{2}$$
$$= \frac{1}{2\omega_b} \int_{-\omega_b}^{\omega_b} tr \left\{ \left[\tilde{C}^{(i+1)}(\omega)\, \hat{C}_0^{-1}\, \hat{A}(\omega) \left[\tilde{A}^{(i+1)}(\omega)\right]^{-1} - I_p \right]^{H} \right.$$
$$\left. \left[\tilde{C}^{(i+1)}(\omega)\, \hat{C}_0^{-1}\, \hat{A}(\omega) \left[\tilde{A}^{(i+1)}(\omega)\right]^{-1} - I_p \right] d\omega. \right. \tag{51}$$

Since the above error involves, as ε_{ML}, Eq. (22), the inverse of a matrix polynomial, a prefiltering operation similar to the one described in step 3a, Eq. (40), is helpful. Specifically, introduce first the matrices $W^{(i+1)}(\omega)$ as

$$W^{(i+1)}(\omega) = \hat{A}(\omega) \left[\tilde{A}^{(i+1)}(\omega)\right]^{-1}. \tag{52}$$

Then, proceeding as in Eq. (40), it can be shown that the corresponding matrices $W_n^{(i+1)}$ satisfying the recurrence relation

$$W_n^{(i+1)} = - \sum_{k=1}^{s} W_{n-k}^{(i+1)}\, \tilde{A}_k^{(i+1)} + \hat{A}_n. \tag{53}$$

Finally, the minimization of ε_C yields the linear system of equations

$$\sum_{k=0}^{s} \left[\sum_{n=max(k,l)}^{min(q+l,q+k)} W_{n-l}^{(i+1)}\, W_{n-k}^{(i+1)} \right] \left[\tilde{C}_k^{(i+1)}\, \hat{C}_0^{-1} \right]^{T} = I_p\, \delta_{l0} \tag{54}$$

for $l=0,1,..,s$. In the above equation, q denotes the largest sample index for which $W_q^{(i+1)}$ can be considered non negligible (in theory, $q=\infty$).

The corresponding new estimates of the matrix $\tilde{C}(\omega)$, i.e. $\tilde{C}^{(i+1)}(\omega)$, can then be used to generate the updated values $\tilde{A}_k^{(i+2)}$ and $\tilde{B}_l^{(i+2)}$ of the remaining ARMAX parameters and the process continues until convergence is obtained.

Model Order Estimation

The procedure described above assumes an a priori knowledge of the model order of the system, i.e. N. In practical cases, however, the exact value of this parameter i unknown since the frequency spectrum of the structure analyzed is as yet unavailable. Various concepts, such as information theoretic measures[3,4] (AIC, MDL, ..), eigenvalues of certain matrices[6], etc., have been suggested to produce an estimate of the true system order. The approach proposed in the present investigation is to determine the value of this parameter by counting the number of system frequencies identified by application of the above ARMAX modeling technique to two or more distinct sets of measurements. Assume for example that the response records of p degrees-of-freedom are available for identification purpose. Then, the application of the above ARMAX identification procedure to this data, with an order s which is large enough to exceed the expected true system order, yields a first set of $p\ s$ natural frequencies and damping ratios. Repeating this analysis with only p/d, $d=2,3,..,or\ p$ response records and a corresponding model order $d\ s$ provides a second ensemble of $p/d \times d\ s = p\ s$ modal characteristics. It is then suggested that the natural frequencies and their corresponding damping ratios and mode shapes that are common to both identification results are characteristic of the system while the remaining ones are associated with the measurement noise. Clearly, for an accurate determination of the system model characteristics, the p/d degrees-of-freedom whose response is used in the second analysis should not all correspond to nodes of any of the mode shapes identified in the first analysis. Once the true system order has been accurately determined, the ARMAX identification scheme can be applied one last time with the correct system order to produce, if desired, an input-output model of the measured data in the form of an ARMA representation, Eq. (3).

Numerical Results

An intensive testing of the model and model order estimation technique described above has been accomplished with four distinct sets of data three of which were obtained by numerical simulation while the last measurements were obtained experimentally and corresponded to the composite shell tested by Red-Horse et al.[7] In all cases, the response records of two points were used both separately ($p=1$) and together ($p=2$) to obtain estimates of the modal characteristics of the structures. Finally, the condition given by Eq. (33) was enforced and the parameter q, Eq. (54), was selected to be 800.

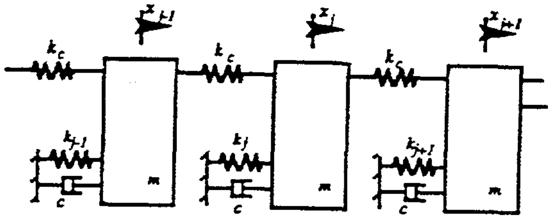

m=0.0114 kg; c=1.443 Ns/m; k=430 000 N/m

Fig. 2 M.D.O.F. System for simulated data

Simulated Data

Three distinct systems consisting of N lumped masses connected to each other and to the ground by springs of stiffnesses k_C and k_j, $j=1,2,3,..,N$, were first considered (see Fig. 2). Damping was introduced by placing dash pots of common coefficients c between the masses and the ground. For simplicity, the masses associated with the N degrees-of-freedom were assumed to be identical and equal to m. Further, in all cases considered the excitation acted only on the first mass and consisted of a mean zero Gaussian white noise sequence F_n of variance arbitrarily set to 100, i.e.

$$E\left[F_n\ F_t\right] = 100\ \delta_{nt}$$

The determination of the response was computed numerically for 2048 time steps using the integration program DIVPRK[8] that relies on Runge-Kutta-Verner fifth-order and sixth-order methods. Measurement noise modeled as a zero mean Gaussian white noise process was added to the response of the different masses but the time history of the excitation was assumed to be noise free. The noise to signal ratio (N/S) was defined as the ratio of the standard deviation of the measurement noise to the corresponding value for the response considered. In all cases and for all degrees-of-freedom, this coefficient was set to 0.05.

A two-degree-of-freedom system was first investigated in which $k_1=k_2=k=k_C$ and $\Delta t = 1.476649\ 10^{-4}$ sec. The order of the prior ARX model was set to $m=45$ when the response of both masses were analyzed ($p=2$) and to $m=90$ when only one record was considered ($p=1$). Shown in

Tables 1 and 2 are the natural frequencies and damping ratios obtained by the multistage ARMAX identification scheme with $s=6$ when $p=2$ (both responses considered) and $s=12$ when $p=1$ (only one of the two responses used). Note first the large variability of the noise natural frequencies obtained which permits a very simple discrimination of the frequencies and provides the correct value of the true system order ($N=2$). Next, note that the ARMAX identification technique yields reliable estimates of the two system natural frequencies (see Table 1) and damping ratios (see Table 2) but also of the mode shapes (see Table 3)

$p=2; s=6$ d.o.f. 1&2	$p=1; s=12$ d.o.f. 1	$p=1; s=12$ d.o.f. 2	Exact
272.08	326.40	401.41	NOISE
977.45	977.47	977.45	977.47
		1393.72	NOISE
1692.97	1692.95	1693.07	1693.02
2096.07	2377.30		NOISE
2173.57	2484.87		NOISE
2669.42	2709.72	2928.62	NOISE
3700.52		3079.47	NOISE

Table 1. Comparison of natural frequencies (Hz) computed by relying on either 1 or 2 response data, 2 d.o.f. case

$p=2;s=6$ d.o.f. 1&2	$p=1;s=12$ d.o.f. 1	$p=1;s=12$ d.o.f. 2	Exact
1.000	0.368	0.159	NOISE
$1.031\ 10^{-2}$	$1.028\ 10^{-2}$	$1.031\ 10^{-2}$	$1.031\ 10^{-2}$
		$1.027\ 10^{-3}$	
$5.928\ 10^{-3}$	$5.912\ 10^{-3}$	$5.924\ 10^{-3}$	$5.950\ 10^{-3}$
$5.432\ 10^{-4}$	0.174		NOISE
$3.793\ 10^{-2}$	$3.014\ 10^{-4}$		NOISE
0.193	0.125	$8.496\ 10^{-3}$	NOISE
0.403		$1.652\ 10^{-2}$	NOISE

Table 2. Comparison of damping ratios computed by relying on either 1 or 2 response data, 2 d.o.f. case

	ARMAX(6,5,6)	Exact
$(\phi_1)_1$	1.001 + 0.002 i	1.000
$(\phi_2)_1$	-0.998 - 0.005 i	-1.000

Table 3. Mode shapes identified by the ARMAX technique and their exact counterparts, 2 d.o.f. case (modal displacement of the mass 2 is set to unity)

The excellent results presented in Tables 1-3 motivated the analysis of a six-degree-of-freedom system in which $k_1=k_6=k+k_C$, $k_2=k_3=k_4=k_5$ with $k_C=200\,000\,N/m$. The response of the masses 3 and 4 was computed with a time step $\Delta t=1.51224\,10^{-4}$ sec. The prior ARX model order was selected to be $m=65$ when $p=2$ and $m=130$ when $p=1$. Shown in Tables 4 and 5 are the natural frequencies and damping ratios obtained by the multistage ARMAX identification scheme with $s=9$ when $p=2$ (both responses considered) and $s=18$ when $p=1$ (only one of the two responses used). Again the large variability of the noise frequencies and damping ratios allows a simple and reliable discrimination of modal characteristics. In that respect, note that the frequencies 3011.31 Hz and 3016 Hz are quite close but a comparison of their damping ratios, $1.175\,10^{-3}$ and $1.760\,10^{-2}$, clearly indicates that this mode is associated with measurement noise. Note again the high accuracy of the estimates of the system natural frequencies (see Table 4), damping ratios (see Table 5), and mode shapes (see Table 6).

$p=2; s=9$ d.o.f. 3&4	$p=1; s=18$ d.o.f. 3	$p=1; s=18$ d.o.f. 4	Exact
74.29	56.43	50.62	NOISE
423.88			NOISE
1021.48	1021.50	1021.48	1021.50
1135.70	1135.58	1135.72	1135.82
1283.14	1283.18	1283.12	1283.14
1428.99	1428.97	1428.98	1428.98
1548.60	1548.68	1548.53	1548.67
1626.29	1626.38	1626.27	1626.34
	2652.43	2859.51	NOISE
3011.31		3016.43	NOISE
3082.46	3111.02		NOISE
	3312.30		NOISE

Table 4. Natural frequencies (Hz) computed by relying on either 1 or 2 response data, aperiodic 6 d.o.f. case

$p=2;s=9$ d.o.f. 3&4	$p=1;s=18$ d.o.f. 3	$p=1;s=18$ d.o.f. 4	Exact
1.000	1.000	0.189	NOISE
1.000			NOISE
$9.899\,10^{-3}$	$9.970\,10^{-3}$	$9.882\,10^{-3}$	$9.861\,10^{-3}$
$8.897\,10^{-3}$	$8.930\,10^{-3}$	$8.932\,10^{-3}$	$8.868\,10^{-3}$
$7.869\,10^{-3}$	$7.921\,10^{-3}$	$7.842\,10^{-3}$	$7.850\,10^{-3}$
$7.062\,10^{-3}$	$7.089\,10^{-3}$	$7.069\,10^{-3}$	$7.049\,10^{-3}$
$6.552\,10^{-3}$	$6.460\,10^{-3}$	$6.532\,10^{-3}$	$6.504\,10^{-3}$
$6.248\,10^{-3}$	$6.298\,10^{-3}$	$6.211\,10^{-3}$	$6.194\,10^{-3}$
	$2.726\,10^{-2}$	$7.438\,10^{-3}$	NOISE
$1.175\,10^{-3}$		$1.760\,10^{-2}$	NOISE
$5.494\,10^{-2}$	$2.476\,10^{-4}$		NOISE
	$5.991\,10^{-2}$		NOISE

Table 5. Damping ratios computed by relying on either 1 or 2 response data, aperiodic 6 d.o.f. case

	ARMAX(9,8,9)	Exact
$(\phi_1)_1$	0.992 - 0.001 i	1.000
$(\phi_2)_1$	-1.000 - 0.001 i	-1.000
$(\phi_3)_1$	0.999 - 0.001 i	1.000
$(\phi_4)_1$	-1.004 - 0.001 i	-1.000
$(\phi_5)_1$	1.001 - 0.010 i	1.000
$(\phi_6)_1$	-0.993 - 0.010 i	-1.000

Table 6. Mode shapes identified by the ARMAX technique and their exact counterparts, aperiodic 6 d.o.f. case (modal displacement of the mass 4 is set to unity)

To provide a final check of the adequacy of the ARMAX identification technique and of the associated model order determination method, a periodic six-degree-of-freedom system was considered in which the masses 1 and 6 were also connected by a spring of stiffness $k_C = 200\,000\,N/m$. Further, the mass to ground stiffnesses were all selected to be equal to k. With these system parameters, the second and third natural frequencies are both repeated so that the true noise free input-output model is an ARMA(8,7,8) when $p=2$. The response of the third and fourth masses was again assumed to be recorded with a time step $\Delta t = 1.51224\,10^{-4}$ sec. Further, the prior ARX model order was selected to be $m=65$ when $p=2$ and $m=130$ when $p=1$. The results shown in Tables 7-9 and corresponding to the selection $s=6$ when $p=2$ and $s=12$ when $p=1$ demonstrate again the reliability of the proposed model and model order estimation techniques.

$p=2;s=6$ d.o.f. 3&4	$p=1;s=12$ d.o.f. 3	$p=1;s=12$ d.o.f. 4	Exact
951.61		11.45	NOISE
977.46	977.46	977.47	977.47
1183.10	1183.13	1183.11	1183.15
1512.82	1512.89	1512.82	1512.82
1653.26	1653.08	1653.33	1653.18
1683.56	1850.69		NOISE
	3110.80	2918.90	NOISE
	3319.77	3312.09	NOISE

Table 7. Natural frequencies (Hz) computed by relying on either 1 or 2 response data, periodic 6 d.o.f. case

$p=2;s=6$ d.o.f. 3&4	$p=1;s=12$ d.o.f. 3	$p=1;s=12$ d.o.f. 4	Exact
$1.502\,10^{-2}$		1.000	NOISE
$1.024\,10^{-2}$	$1.030\,10^{-2}$	$1.023\,10^{-2}$	$1.03\,10^{-2}$
$8.459\,10^{-3}$	$8.457\,10^{-3}$	$8.451\,10^{-3}$	$8.51\,10^{-3}$
$6.643\,10^{-3}$	$6.681\,10^{-3}$	$6.654\,10^{-3}$	$6.66\,10^{-3}$
$6.051\,10^{-3}$	$6.007\,10^{-3}$	$6.042\,10^{-3}$	$6.09\,10^{-3}$
0.126	1.000		NOISE
	$3.737\,10^{-4}$	$8.702\,10^{-3}$	NOISE
	$8.983\,10^{-2}$	$5.883\,10^{-2}$	NOISE

Table 8. Damping ratios computed by relying on either 1 or 2 response data, periodic 6 d.o.f. case

	ARMAX(6,5,6)	Exact
$(\phi_1)_1$	0.998 + 0.002 i	1.000
$(\phi_2)_1$	0.500 - 0.0001 i	0.500
$(\phi_3)_1$	-0.498 + 0.002 i	-0.500
$(\phi_4)_1$	-0.988 - 0.011 i	-1.000

Table 9. Mode shapes identified by the ARMAX technique and their exact counterparts, periodic 6 d.o.f. case (modal displacement of the mass 4 is set to unity)

Experimental data

To confirm the excellent result obtained in connection with the simulated data, it was decided to test the proposed identification method on experimental data. The response of the composite shell investigated by Red-Horse et al.[13] was chosen in particular because of the availability of estimates of the natural frequencies and damping ratios determined by both the ERA/DC[6] and the polyreference technique[9]. The length of the ARX model was selected to be $m=65$ when $p=2$ and $m=130$ when $p=1$. The ARMAX model was selected to be $s=28$ when $p=2$ and $s=56$ when $p=1$. The discremination of the system vs. noise natural frequencies was consistent with the simulated data. Shown in Table 10 are the estimates of the system natural frequencies and damping ratios obtained. Note in particular that the ARMAX procedure was able to detect the presence of repeated frequencies both with two and one responses observed. Overall, it is seen that the ARMAX results match well with their ERA/DC and polyreference counterparts. In this regard, it should be noted that the ERA/DC and polyreference results have been derived from 7 different records while the ARMAX natural frequencies and damping ratios have been extracted from only one of these 7 time histories. Further, the indicated ERA/DC and polyreference values for mode 7-10 have not been computed from the same 7 records but rather from another set of 7 time histories for which the sampling time was 4 times lower[7].

ARMAX 1 rec;p=2	ARMAX 1 rec;p=1	ERA/DC 7 records	polyreference 7 records
8.346 8.339	8.341	8.340	8.335
11.967 12.010	11.966	11.958	11.952
23.748	23.748	23.744	23.741
29.808 29.670	29.819	29.820	29.770
45.635 45.926	45.663 45.462	45.649	45.673
52.463 52.943	52.504 52.828	52.459	52.502
74.206 74.275	74.261	74.255*	74.285*
81.008 81.420	81.067 81.654	80.888*	80.928*
109.176 109.460	109.132	109.235*	109.266*
115.318 115.631	115.098 114.776	115.279*	115.307*
6.43 28.37	6.45	6.89	7.50
11.72 21.30	13.52	13.44	13.56
5.68	5.75	5.35	5.64
10.67 25.12	10.68	11.63	11.06
4.56 5.73	5.61 12.48	4.85	4.95
7.81 9.30	7.82 22.04	7.74	7.57
3.70 3.88	4.26	4.01*	4.34*
7.77 7.84	9.54 8.87	9.20*	9.36*
4.00 5.17	3.12	3.92*	3.96*
5.65 6.75	5.84 42.61	6.19*	6.78*

* Results estimated from different records

Table 10. Comparison of natural frequencies and damping ratios - Experimental data

Conclusions

In this paper, the determination of the modal characteristics, number and values of the natural frequencies, damping rations, and mode shapes, of a vibrating structure has been addressed. Specifically, the connections between the noisy response of p degrees-of-freedom of a structure and the output of an exogeneous autoregressive moving average (ARMAX) discrete system has been utilized to perform the required identification.

The estimation of the ARMAX model that "best" represents the measured data has been accomplished in four steps, as shown in Fig. 1. First, an ARX model is obtained from the measured responses and excitation records by solving the linear system of equations, Eq. (30)-(34). This prior ARX model can then be used to initialize the exogeneous matrix polynomial $\tilde{C}(z)$ through Eq. (37). Then, an iterative scheme is employed to determine the ARMAX model that provides, at the same time, the "best" fit of both the existing data and the prior ARX model. Upon convergence of this process, the estimates of the natural frequencies, damping ratios, and mode shapes can be obtined from the autoregressive part of the ARMAX model, see Eq. (11)-(16).

The determination of the true model order, i.e. of the number of system natural frequencies that can be observed in the given records, has been addressed by relying on identification results that correspond to distinct sets of data. In fact, the numerical results presented here have shown that the estimates of the true modal characteristics vary very little from identification results obtained with one data set to those obtained with different response records. On the contrary, the frequencies associated with the measurement noise have been shown to change substantially, if not drastically, from one set of results to another. This property allows for a very simple and efficient discremination scheme of the true modal characteristics that in turn yields an accuate estimate of the true order of the system.

Finally, an intensive testing of the proposed multistage ARMAX identification scheme with both simulation and experimental data has demonstrated its high reliability in providing accurate estimates of not only the natural frequencies but also of the damping ratios and mode shapes of a structure from records of its response.

Acknowledgements

The support of this work by the contract number 96-0277 from Sandia National Laboratories is gratefully acknowledged.

References

1. Lee, J.E., and Fassois, S.D., "A Stochastic Suboptimum Maximum Likelihood Approach to Structural Dynamics Identification," *Proceedings of the 8th International Model Analysis Conference*, Kissimmee, FL, Jan. 29 - Feb. 1, 1990, Vol. 2, pp. 1424-1433.
2. Mignolet, M.P., Red-Horse, J.R., and Lin, C.C., "A Multistage ARMAX Identification of Structures," *Proceedings of the 34th Structures, Structural Dynamics, and Materials Conference*, Apr. 19-21, 1993, La Jolla, California, pp. 3366-3374.
3. Akaike, H., "A New Look at the Statistical Model Identification," *IEEE Transactions on Automatic Control*, Vol. AC-19, Dec. 1974, pp. 716-723.
4. Rissanen, J., "Modeling by Shortest Data Description," *Automatica*, Vol. 14, 1978, pp. 465-471.
5. Gersch, W., and Yonemoto, J., "Synthesis of Multivariate Random Vibration Systems: Two-Stage Least Squares AR-MA Model Approach," *Journal of Sound and Vibration*, Vol. 52, No. 4, 1977, pp. 553-565.
6. Juang, J.-N., Cooper, J.E.., and Wright, J.R., "An Eigensystem Realization Algorithm Using Data Correlations (ERA/DC) for Modal Parameter Identification," *Control Theory and Advance Technology*, Vol. 4, No. 1, Mar. 1988, pp. 5-14.
7. Red-Horse, J.R., Carne, T.G., James, G.H., and Witkowski, W.R., "Structural System Identification of a Composite Shell," *Proceedings of the 33rd Structures, Structural Dynamics, and Materials Conference*, April 13-15, 1992, Dallas, Texas, pp. 1732-1740.
8. IMSL, *User's Manual*, Version 1.1, Dec. 1989.
9. Vold, H., and Recklin, G.F., "The Numerical Implementation of a Multi-Input Modal Estimation Method for Mini-Computers," *Proceedings of the International Modal Analysis Conference*, Nov. 1982.

Appendix B
LDRD Summary

LDRD Summary:

Number of patent disclosures resulting from this project:	0
Number of patent applications resulting from this project:	0
Number of patents:	0
Number of copyrights resulting from this project:	2
Number of students supported by this project:	3
Number of technical staff hired as a result of this project:	2
Number of awards received by the staff as a result of this project:	1 Best Paper Award 1994 AIAA SDM Conference

Distribution List:

MS0321 W. J. Camp
MS0439 D. R. Martinez
MS0439 J. R. Red-Horse (20)
MS0188 C. E. Meyers
MS9018 Central Technical Files, 8940-2
MS0899 Technical Library, 4414 (5)
MS0619 Review & Approval Desk, 12690
for DOE/OSTI (2)